Nanomechanical Systems from 2D Materials

by

Xinghui Liu

B.S., Shaanxi University of Science and Technology, 2005

M.S., Shaanxi University of Science and Technology, 2008

A thesis submitted to the

Faculty of the Graduate School of the

University of Colorado in partial fulfillment

of the requirement for the degree of

Doctor of Philosophy

Department of Mechanical Engineering

2014

This thesis entitled:

Nanomechanical Systems from 2D Materials

written by Xinghui Liu

has been approved for the Department of Mechanical Engineering

_____

J. Scott Bunch

Committee Chairman, Department of Mechanical Engineering

_____

Xiaobo Yin

Department of Mechanical Engineering

Date_____

The final copy of this thesis has been examined by the signatories, and we

Find that both the content and the form meet acceptable presentation standards

Of scholarly work in the above mentioned discipline.

Liu, Xinghui (Ph.D., Department of Mechanical Engineering)

Nanomechanical Systems from 2D Materials

Thesis directed by Professor J. Scott Bunch

ABSTRACT

The isolation of graphene, a single atomic layer of carbon atoms, leads to the exploration of a group of new materials - 2 dimensional (2D) crystals, which have unique properties in mechanical, electrical and optical fields. This thesis demonstrates our work on the development of nanomechanical systems from 2D materials (graphene and MoS_2) and using them for the study of material properties.

At first, we developed large arrays of 3-terminal graphene NEMS switches with a novel design, which help the devices to achieve low actuation voltages (down to ~3V), improved reliability and mechanical integrity. These switches may find applications in mechanical computing, data storage, and RF communication, and the design can be used for other 2D materials based NEMS switches. We also studied the electromechanical properties of the devices. A study of the threshold switching voltages is carried out, and the switching voltage is simulated with a finite element model which includes nonlinear mechanics. From this we deduce a scaling relation between the switching voltage and device dimensions.

Next, we present a unique nanomechanical configuration that allows us to determine the interfacial forces between graphene and Au/SiO$_2$. The nature of the interfacial forces at ~ 10 - 20 nm separations is consistent with an inverse fourth power distance dependence, implying that the interfacial forces are dominated by van der Waals interactions. Furthermore, the strength of the interactions is found to increase linearly with the number of graphene layers. The experimental approach can be used to measure the strength of the interfacial forces for other atomically thin two-dimensional materials, and help guide the development of nanomechanical devices such as switches, resonators, and sensors.

Finally, we show the modulation of electronic band structure in monolayer suspended MoS$_2$ membranes with local biaxial strain at the center of a spherical blister. We observed a linear direct band gap (A peak) decrease rate of ~100 meV/% strain in monolayer MoS$_2$. Future work includes biaxial strain engineering on bilayer and trilayer MoS$_2$.

Acknowledgement

Working on my Ph.D. thesis during the last 6 years in Boulder is an unforgettable life journey for me. I think Boulder is a perfect place for living, but what I enjoy most was the research during this period of time. So at first I want to thank my advisor, Professor Scott Bunch, for bringing me into an exciting area of scientific study and leading me to the successful completion of this thesis. After trying to make nano size metal powders for about 2 years in China, I realized that there is a lot of room and fun as well after scaling the size of materials into the nano scale. When I was looking for the smallest material I can work on in the department after arriving at CU, Dr. Bunch introduced me to graphene, which is amazingly one atom thick. With this unique structural property, there are tons of potentials to explore and the primary one of them is to make transistors from graphene. Other than traditional field effect transistors (FETs), he led me to explore some unusual transistors from graphene, and the work in the Ch. 5 is one of them that finally interested us most. Within all those years of making transistors, his passion and wisdom always inspired me. Furthermore, Dr. Bunch taught me how to keep patient when facing failures and how to tackle difficult problems with creativity. All this training significantly accelerated my speed to complete the work in Ch. 6 and Ch. 7.

It turns out that I am the first and last group member in Dr. Bunch's lab in CU, and I want to say it was lots of fun to work with all the group members during this period of time. Steven Koenig and Phi Pham were the first batch of students in the lab and contributed a lot for building the lab. Luda Wang came one year later and was always happy to help with different projects. Lauren Cantley started working with me in 2010 summer REU program followed by Miguel Rodriguez and Mariah Szpunar in 2011. Here I want to thank them all for their significant

Contents

Table

List of Figure

Chapter 1

Introduction

1.1   Introduction

Everyone has an unforgettable memory with colorful balloons during childhood. For me, the happiness with balloons continues to my Ph.D. period. My work in the last few years is to make and study tiny balloons of a few microns in diameter from a new family of materials, 2 dimensional (2D) materials. To put it in a more scientific way, I make graphene and molybdenum disulfide (MoS_2) membranes based nanomechanical systems, and study intrinsic properties of the materials, or their interactions with surrounding materials by manipulating them with different approaches. In this thesis, it is demonstrated the graphene/MoS_2 balloons are "blown" with electrostatic force, van der Waals force, and pressure differences. The whole thesis details how I build, play, control, and use these tiny balloons for various applications, and probe science behind the colorful and magical balloons.

No one would have imagined that scotch tape can finally lead to scientific studies recognized by a Nobel Prize in 2004. However, the scotch tape to isolate graphene sheets made it. It gave birth to the discovery and study of a family of 2 dimensional (2D) materials, which became one of the hottest topics in science and engineering in the past 10 years. At this point, I would say, for me, the tiny balloons are like the scotch tape for exfoliation of single crystal graphene, helping me have new discoveries and enjoy the scientific studies, which matters a lot to me, even though they are just like a droplet of sea water in the ocean of scientific research.

1.2   Outline

This thesis presents systematic experiments on graphene and MoS_2 based nanomechanical systems including graphene nanoelectromechanical (NEMS) switches, graphene annular bulges to study the interfacial forces in the atomic membranes, MoS_2 spherical caps for bandgap engineering with biaxial strain in MoS_2. Chapters 1-4 review the fundamentals and status of relevant studies. The experimental parts start from Chapter 5, where we demonstrate the first work of large arrays of 3-terminal NEMS switches with a novel nanomechanical design, which can reduce the actuation voltage, improve the mechanical integrity and reliability. A modified form of this chapter is published in *Advanced Material **26**, 1571* (2014). Chapter 6 introduces our observation of pull in instability in graphene membranes under interfacial forces, which plays an important role in nanomechanical systems. We also analyze the pull in phenomenon analytically and numerically, which leads to a quantitative estimation of the interfacial force in graphene membranes. The calculated interfacial force between graphene and SiO_x on silicon wafer is ~1.5% of the dispersion force between two perfectly metallic parallel plates, while that between graphene and gold is ~10%. The experiment is published in *Nano Letters* **13**, 2309 (2013). Chapter 7 describes my work on the other 2D material, MoS_2. We tune the band structure of free standing MoS_2 membrane with biaxial strain by pressurizing the membrane. The overall tuning rate for monolayer MoS_2 is ~0.1 eV/%, twice the modulation rate with uniaxial straining. The work is under preparation for a journal paper submission.

1.3   Nanomechanical Systems

Nanomechanical systems function as nanomechanical structures either deflecting or vibrating. Like macroscopic mechanical structures, nanomechanical structures can take the forms of cantilevers, doubly clamped beams, plates, membranes, and etc. However, after scaling into the nano size regime, nanomechanical systems have various intriguing attributes due to the scaled dimensions.[1–4] Prominent of these attributes is the higher resonance frequency owing to size scaling, which can reach up to 10 GHz.[2] Such high-frequency mechanical devices show capacity for responding to applied forces in less than one nano second. A second advantage is lower power dissipation, largely determined by high Q factor in nanomechanical structures. The Q factors attained for nanomechanical systems in moderate vacuum are in the range of 10^3 to 10^5, while Q values for high-frequency electrical resonators are typically less than one hundred. Therefore, the nanomechanical system is expected to have decreased degree of internal dissipation, thereby leading to low operating power levels. Furthermore, thermal fluctuations in nanomechanical system nanomechanical systems are at about the attowatt (10^{-18}) scale. Therefore, signal-to-noise ratios of up to 10^6 can be attained by driving a nanomechanical system with picowatt (10^{-12}) level.[2]

Meanwhile, the small effective mass from the vibrating part can provide nanomechanical systems with an astoundingly high sensitivity to additional masses considering the low mass of the nanomechanical structures.[5] This can be a valuable attribute for a wide range of sensing applications. Finally, the reduced dimension of nanomaterials used in NEMS, such as nanowires, nanotubes, or membrane with atomic layers, grants us more options to actuate the nanomechanical structures. Take carbon nanotube as an example,[6] we can bend it in any

3
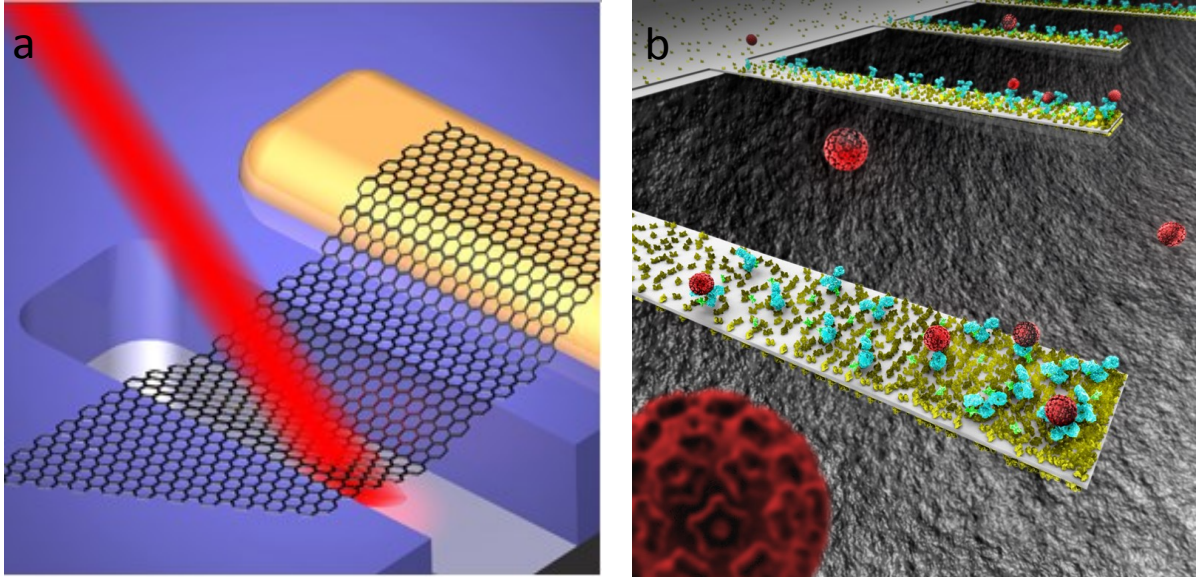
Figure 1.1 Nanomechanical Systems: a) NEMS resonator from exfoliated graphene,[7] b) nanomechanical mass sensor to detect molecules (adapted from *http://the-briefing.com*).

direction, stretch it by applying tension along the tube, and rotate it by applying shear stress along the tangential direction of it periphery. The versatility of actuation modes is favored, because it shall lead to numerous types of sensing or actuating devices. Owing to these encouraging attributes, NEMS could be used across a broad range of applications including highly sensitive mass sensor, high resolution magnetic resonance imaging, radio frequency (RF) signal processing, etc.[2]

1.4 Top-down versus Bottom-up Fabrication

There are two main approaches to build nanomechanical systems: top-down or bottom-up.[8–10] As we can understand from the name, top down fabrication starts from bulk materials, and makes nanomechanical structures by using lithography for patterning from the top followed by several etching-down steps. A releasing process is always required to make suspended nanomechanical elements. Until now, silicon is still the primary material used in this approach due to its excellent mechanical properties and well established patterning and etching technologies derived from semiconductor integrated circuit (IC) industry. Other materials used in top-down include atomic layer deposition (ALD) oxide / metal, silicon carbide, diamond like carbon.[9,11,12] A top-down strategy is suitable for large arrays, design oriented, and leads to well controlled fabrication of nanomechanical systems. However, available materials for top-down are still limited, and the materials are easy to crack due to grain boundaries, material defects, and process induced stress.

The other approach starts with the fabrication of nano/micro size features like trenches or cavities, followed by suspension of nano-scale materials on the top with a transfer process. Traditional nanomaterials used as building blocks in this approach ranges from zero dimension

fullerene or gold particles to one dimensional carbon nanotubes (CNT) or silicon nanowires.[8,13] The exceptional properties of nanomaterials can be integrated and transferred to the nanomechanical systems with this approach. However, we can rarely achieve large array fabrication in this case.

Combining these two approaches, to integrate their advantages and to avoid their drawbacks becomes an interesting issue in wafer scale fabrication of nanomechanical systems, nano-electronics, nano-optoelectronics, etc. The ideal strategy should allow large arrays, design oriented fabrication as well as the integration of nanomaterials with exceptional properties. The development of 2D materials provides a promising approach to the integration of outstanding properties from nanomaterials into large arrays of devices. Take graphene for example. Right now we don't have to wait for good luck to bring us tens of micron size graphene by drawing graphite. Instead, it is possible to make graphene wafers with chemical vapor deposition of carbon atoms on copper foil followed by a transfer process, which can move graphene from the foil to any substrate we want.[14–17] In this way, graphene becomes compatible to traditional microfabrication techniques and even complementary metal-oxide semiconductor (CMOS) process. Graphene itself, can be patterned by oxygen plasma, which will not etch typical substrate materials, like Si, SiO_2, and metals.[18] On the other hand, release etchants for SiO_2 or metals does not severely damage the quality of graphene. The compatibility for integration and the selectivity during fabrication process in graphene and other 2D materials offers the possibility to fabricate large arrays of nanomechanical/nanoelectronics devices while keeping the intrinsic properties in the 2D materials.

1.5   Conclusion

This chapter introduces the outline of this thesis, followed by a brief introduction of 2D materials, mechanics in 2D materials, and review of nanomechanical systems in Chapter 2, 3, 4, respectively. In Chapter 5, we will introduce our novel design of graphene NEMS switches, and demonstrate our study on the large arrays of 3-terminal switches fabricated. In Chapter 6, we will describe the measurement of the interfacial forces between graphene and substrate with a unique set up. Chapter 7 will introduce the electronic bandgap tuning in monolayer MoS_2 with biaxial strain.

Chapter 2

Graphene, MoS$_2$, and Beyond

2.1 2D Materials

Dimensionality is one of the most fundamental material parameters, which not only defines the atomic structure of the material but also determines the properties to a significant degree.[19–23] The same chemical element or compound can exhibit dramatically different properties in different dimensionality. After the discovery of fullerene and single layer carbon nanotube (CNT), which are 0D and 1D carbon nanomaterials respectively, researchers tried to isolate 2D graphitic material or to make 1D nano-ribbons from 2D crystals. The efforts have started to pay off since 2004 with the first isolation and electrical characterization of graphene transistors published by Geim's group.[18] At that time, most people would not expect that more than a dozen kinds of 2D crystals can be isolated and studied in less than 10 years. Right now, the 2D materials family includes not just carbon material but also transition metal dichalcogenides (TMDs), oxides, and layered metals. One of the most promising applications of 2D materials is in electronic devices.[20,21,24] With respect to the electrical properties, we can already have superconductors, metallic materials, semimetals, semiconductors, insulators from the 2D crystals, namely a complete electrical materials family.

Table 2.1 lists all the current members in the 2D layered materials family. However, stability is a critical issue. The blue shaded materials are stable under ambient conditions (room temperature in air) for monolayers. Those probably stable in air are shaded green but those may

be stable only in inert atmosphere are shaded pink. Grey shading means monolayer has been exfoliated and verified by AFM, but no further information has yet been provided.

Table 2.1 2D materials family[24]

Graphene family	Graphene	hBN 'white graphene'		BCN	Fluorographene	Graphene oxide
2D chalcogenides	MoS_2, WS_2, $MoSe_2$, WSe_2		Semiconducting dichalcogenides: $MoTe_2$, WTe_2, ZrS_2, $ZrSe_2$ and so on		Metallic dichalcogenides: $NbSe_2$, NbS_2, TaS_2, TiS_2, $NiSe_2$ and so on	
					Layered semiconductors: GaSe, GaTe, InSe, Bi_2Se_3 and so on	
2D oxides	Micas, BSCCO	MoO_3, WO_3	Perovskite-type: $LaNb_2O_7$, $(Ca,Sr)_2Nb_3O_{10}$, $Bi_4Ti_3O_{12}$, $Ca_2Ta_2TiO_{10}$ and so on		Hydroxides: $Ni(OH)_2$, $Eu(OH)_2$ and so on	
	Layered Cu oxides	TiO_2, MnO_2, V_2O_5, TaO_3, RuO_2 and so on			Others	

The rule of thumb to obtain 2D crystal from its 3D layered parent can be helpful for the search of new 2D family members. First, 3D layered materials with high melting temperature, typically over 1000 °C, have better chances. Second, potential 3D layered parents better have chemical inertness. Third, insulating and semiconducting 2D crystals are more likely to be stable after exfoliation or synthesis. [24]
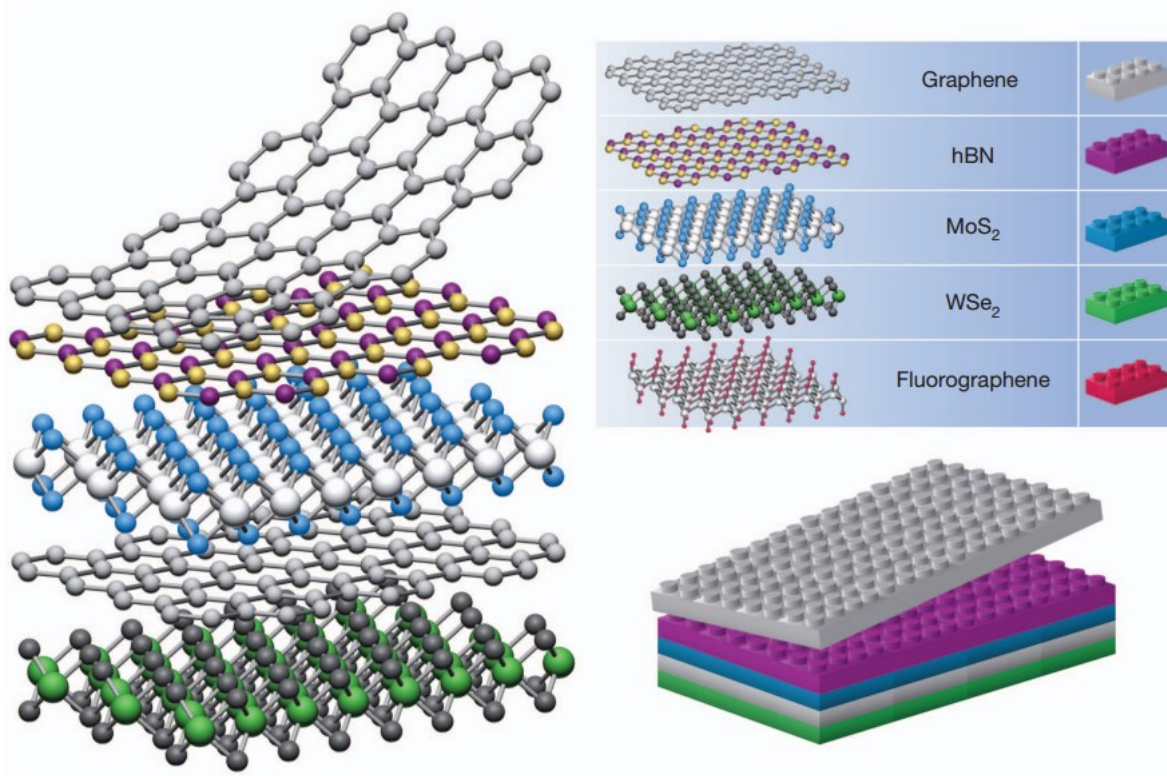
Figure 2.1 Common 2D materials: graphene, MoS_2, hBN, WSe_2, and Fluorographene.[24]

2.2 *Graphene*

Even though graphene is the last one to be isolated in the carbon materials family, it serves as the building block for other family members with different dimensionalities. It can be wrapped up into 0D buckyballs, rolled into 1D nanotubes or stacked into 3D graphite.[22,24,25] Furthermore, graphene exhibits a combination of excellent electronic,[25–27] mechanical,[28,29] optical[30] and thermal properties,[31] which may make it substitute silicon in electronics, photonics, and NEMS as well in this century or next, and this is most researchers' "dream" about graphene or other 2D materials. Considering graphene as a structural material used in NEMS, here I will briefly introduce the electronic and mechanical properties.

Graphene was initially discovered as a remarkable high quality semimetal with a pronounced ambipolar electric field effect.[18] Charge carriers in the material can be tuned continuously between electrons and holes in concentration as high as 10^{13} cm^{-2} and their mobility can exceed 15,000 cm^{2}V^{-1}s^{-1} under room temperature and with a SiO_2 substrate underneath. Besides, as its allotrope-diamond, graphene is considered one of the stiffest and strongest materials if it is in the form of single crystal. Its Young's modulus for stretching is as high as 1 TPa, and breaking stress about 42 N/m with 25% strain, thereby showing the potential of fast response and long life cycle without failure in NEMS.[28,29] What is more, graphene is impermeable to gas molecules, and even helium atoms cannot pass through.[32] This highly conductive, strong and flexible, gas impermeable membrane attracts great interests to make NEMS out of graphene.[32]

11
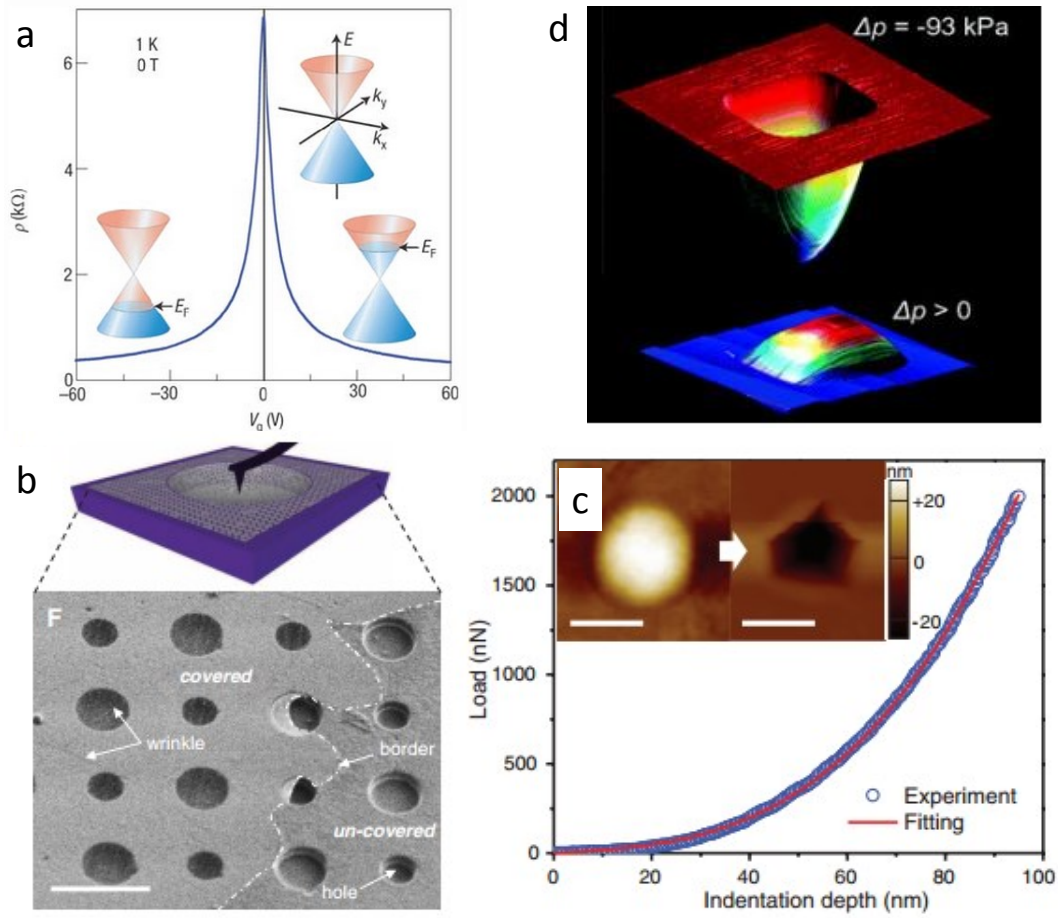
Figure 2.2 Electrical and mechanical properties in graphene a) Ambipolar electric field effect in single-layer graphene.[22] b) (lower) SEM images of the suspended CVD graphene film over holes. (upper) Schematics of the device. c) Force-displacement curve of the single grain graphene film in AFM nanoindentation. Insets are AFM images of graphene film before and after nanoindentation. Scale bar is 3 μm and 1 μm for (b) and (c), respectively.[28] d) AFM images of gas impermeable graphene membranes when bulged down (upper) and bulged up (lower).

To integrate graphene into wafer scale device fabrication, preparation of large area monolayer/few layer graphene with uniform properties is the first step. Right now we don't have to wait for good luck to bring us just tens of micron size graphene by drawing graphite. Instead, it is possible to make graphene wafers with chemical vapor deposition (CVD) of carbon atoms on copper foil.[16] However, CVD graphene are polycrystalline with grains patched together with grain boundaries and voids.[33] How to increase the grain size or reduce voids becomes a critical issue.

Just like the crystal growth of other materials, the CVD of graphene starts with nucleation as well. To increase the size of single crystal, one necessary step is to reduce the density of nucleation sites. Even though this idea looks self-evident, previous efforts to improve the yield and quality of CVD graphene mainly focused on process details like changing C:H ratio,[34] tuning the H_2 and hydrocarbon (CH_4) gas pressures,[35] and smoothing the surface of copper foil.[36,37] Recently, Ruoff's group demonstrated the oxygen passivation of Cu foil surface before the flow of CH_4 significantly suppresses graphene nucleation, fostering growth of ultralarge single-crystal graphene domains.[17] They can repeatedly grow centimeter size graphene single crystals with oxygen passivation during CVD. This size has been close to the size of processor chip. The measured mobility ranges from 15,000 to 30,000 $cm^2V^{-1}s^{-1}$ at room temperature, comparable to that of exfoliated graphene.

To integrate CVD graphene into device fabrication, it is always required to transfer the graphene from copper foil to other substrates, typically silicon wafer.[38–42] Typical transfer processes use PDMS or PMMA as the media to hold CVD graphene during the etching of Cu foil in liquid etchants. After transferring the media together with graphene to a target substrate the polymer is stripped from graphene either by rinsing with Acetone/IPA or baking at high
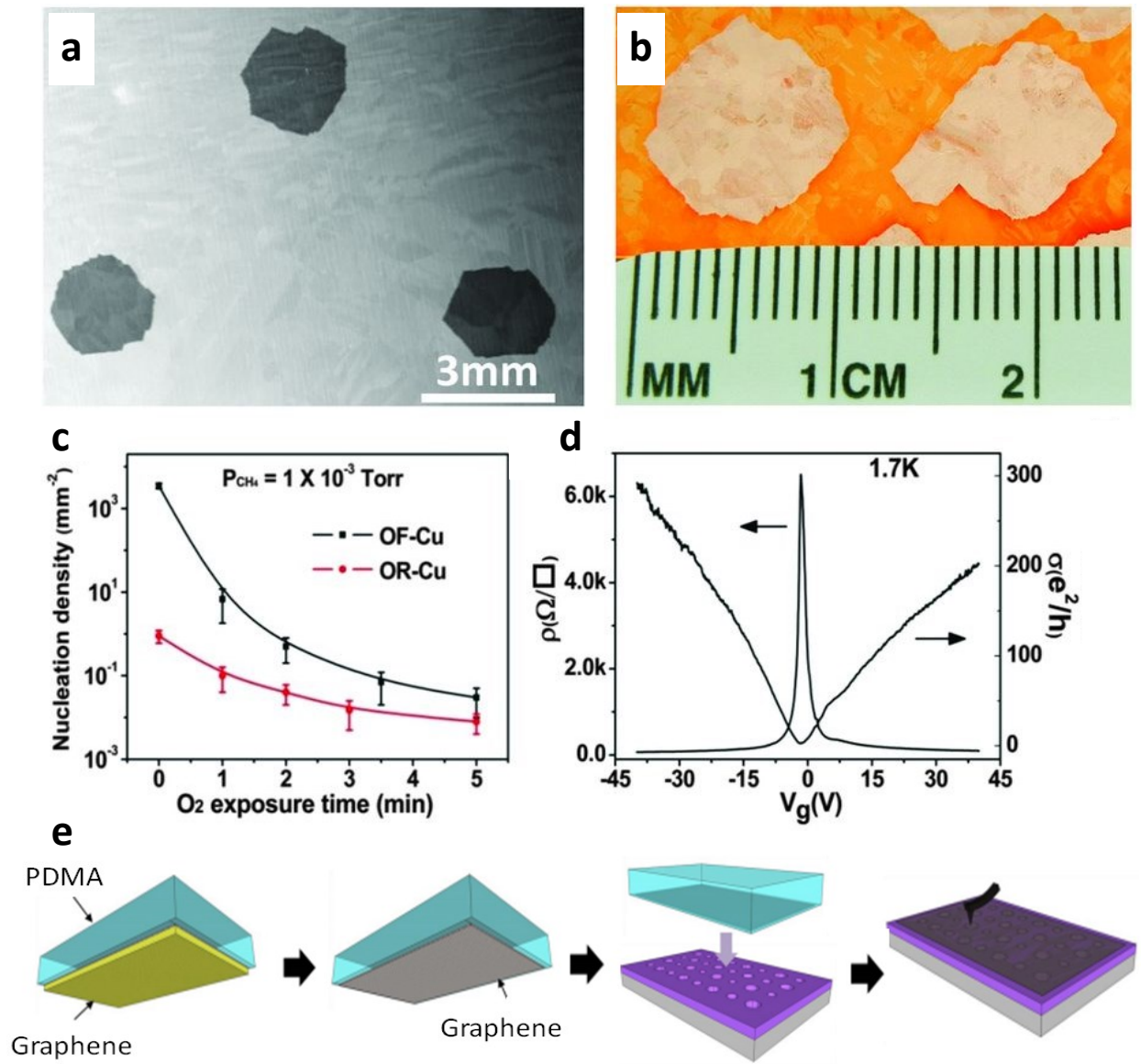
Figure 2.3 CVD growth and transfer of graphene a) SEM image of low-density graphene domains on OR-Cu exposed to O_2.[17] b) Optical image of centimeter-scale graphene domains on OR-Cu exposed to O_2. c) The graphene nucleation density vs O_2 exposure time. d) Plots of resistivity and conductivity as a function of gate voltage at 1.7 K. e) Dry transfer of CVD graphene over microcavities using PDMS.

14

temperature for PMMA, or by directly peeling PDMS. In this way, graphene becomes compatible to CMOS processes. Graphene can be patterned by oxygen plasma, which will not etch typical substrate materials, like Si, SiO_2, and metals. On the other hand, release etchants for SiO_2 or metals can hardly impair the quality of graphene significantly. The compatibility for integration and the selectivity during fabrication process offers great flexibility for the fabrication of graphene based NEMS or other electronic, photonic devices.

2.3   MoS$_2$

The intense interest and rapid progress in graphene researches also led to exploration of other 2D materials.[10,20,23] In particular, single layers of transitional metal dichalcogenides (TMDs) have attracted notable attention because of their diverse properties and natural abundance. Despite the similarity in the chemical formula MX_2, where typically M is a transition metal of groups 4-10 and X is a chalcogen, single layer 2D TMDs exhibit versatile chemistry and properties, ranging from insulators such as HfS_2, semiconductors such as MoS_2, semimetal such as $TiSe_2$, to true metals such as NbS_2, which can even exhibit superconductivity at low temperature.

One important reason for researchers to study TMDs single layers is to find semiconductors with sizable band gaps, therefore we can apply this kind of materials in field effect transistors (FETs) to achieve improved on/off ratio compared with graphene FETs, or use them as light-absorbing materials in alternative thin film solar cells considering their bandgaps in the visible range.[10] Here we will just introduce MoS_2 as a representative of TMDs, since it has been the most studied so far due to its natural abundance and ease of exfoliation from a parent 3D crystal.
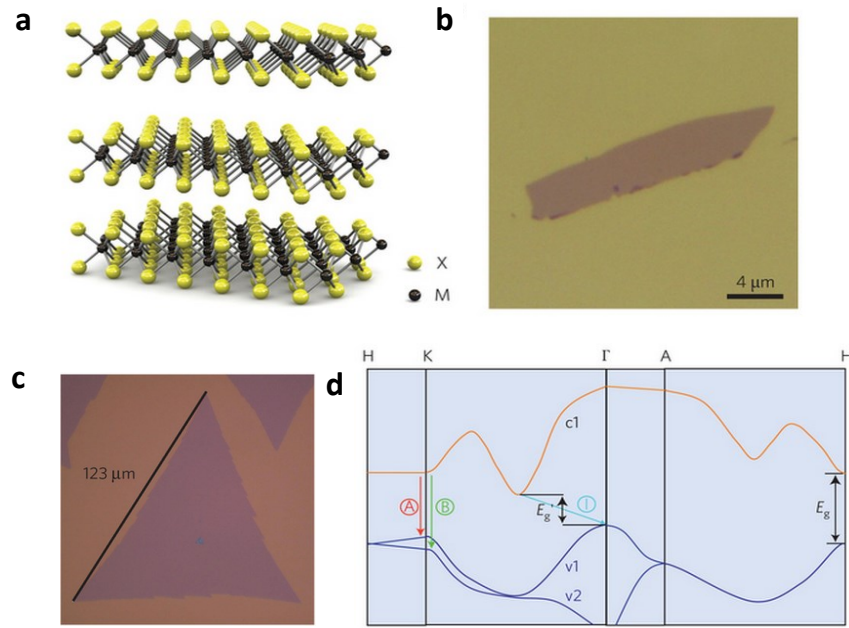
Figure 2.4 a) Atomic structure of monolayer MoS$_2$.[10] b) Optical image of exfoliated monolayer MoS$_2$ flake. c) Optical image of CVD MoS$_2$ flake. d) Simplified band structure of bulk MoS$_2$.[43]
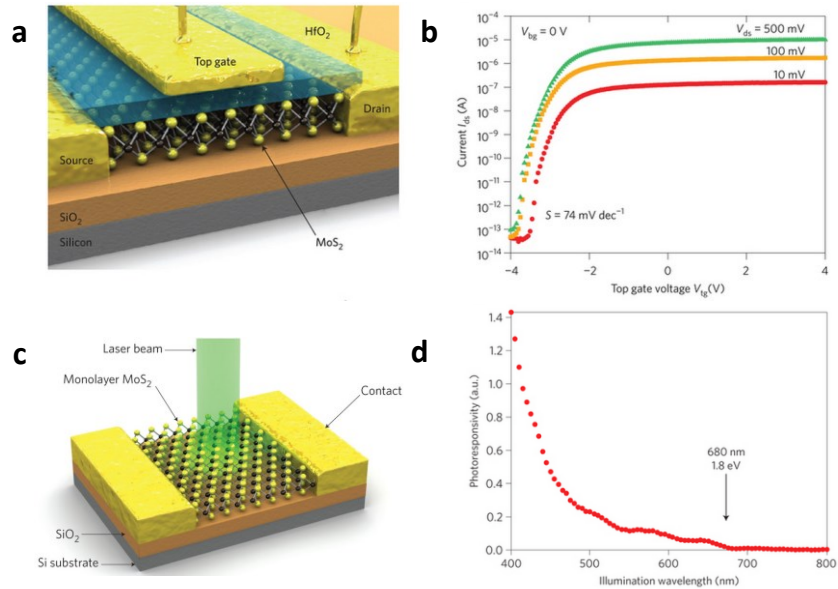
Figure 2.5 a) Schematic of a MoS$_2$ top gate field effect transistor. b) I_{ds} vs V_g.[44] c) Schematic of a MoS$_2$ photodetector. d) Photoresistivity over illumination wavelength.[45]

Monolayer MoS_2 has a direct bandgap of 1.9 eV (A peak), while few layers MoS_2 also has additional peaks corresponding to the indirect bandgap and direct-gap hot luminescence.[43,46] State of the art MoS_2 top-gated FETs developed by Kis' group showed excellent on/off current ratio up to 10^8, room temperature mobility of >200 $cm^2V^{-1}s^{-1}$, and subthreshold swing of 74 mV per decade.[44] The top-gated geometry with high k dielectric used allows a reduction of working voltages, therefore MoS_2 can be considered as a good candidate for low-power electronics. Kis' group also demonstrated ultra-sensitivity of 880 A/W at a wavelength of 561 nm in monolayer MoS_2 photodetectors with the photoresponsivity ranging from 400 nm to 680 nm.[45] The result shows great potential for applications of MoS_2-based integrated in optoelectronic circuits, light sensing, biomedical imaging, video, recording and spectroscopy.

On the other hand, single layer MoS_2 is also a good material for flexible electronics/optoelectronics. Its in-plane stiffness is ~180 N/m, corresponding to an effective Young's modulus of 270 GPa, comparable to that of steel. Breaking occurs at an effective strain between 6 and 11%.[47] Even though one might argue that its mechanical property is not as exceptional as graphene, it is adequate for flexible electronics/optoelectronics applications.

The fabrication of 2D MoS_2 is similar to graphene in several aspects: two main preparation methods are mechanical exfoliation and CVD; it can also be patterned with lithography and oxygen plasma. The monolayer MoS_2 single crystal grown with CVD reaches length scales of up to 100 μm, making it promising for further researches and industrial applications.[48]

2.4   Conclusion

This chapter has a general introduction of 2D materials and introduces the electrical and mechanical properties of graphene and MoS_2 in detail. The next chapter will describe the nanomechanics of 2D materials which will be applied for the analysis of the experimental parts of this thesis.

Chapter 3

Nanomechanics of 2D Materials

3.1 Mechanical Properties of Membranes

The most fundamental mechanical properties of engineering materials lie in the linear response of strain under stress, also known as Hooke's Law, which can be considered a mechanical equivalent to Ohm's law. If we apply a uniaxial compressive or tensile stress to the material, the relation can be expressed as:

$$\sigma = E\varepsilon \tag{3.1}$$

where σ stands for the stress, while ε the strain. Materials usually differ from each other in E, known as the modulus of elasticity of Young's modulus.[19,49]

When applying shear loading to the material instead, we can write a similar equation:

$$\tau = G\gamma \tag{3.2}$$

where τ and γ are the shear stress and strain, respectively; G is called the shearing modulus of elasticity or modulus of rigidity of the material.

Another unique property in different materials is related to the geometry of the material, Poisson's ratio v, which is the constant ratio of the lateral strain to the axial strain. However, G is related to E and v as in an isotropic material:

$$G = \frac{E}{2(1 + v)} \tag{3.3}$$

Accordingly, there are only two independent elastic constants.

19

In practice, materials are usually engineered into different types of structures, like 1D bars or frame structures. Planar or curved structures are a family of structures that have two dimensions much larger than the third one. Three family members are included in the third type: panel, plates and shell. Panels are loaded only to in-plane stress, while plates are subjected to out of plane loads as well. Shells are usually curved planar structures with very small thickness compared with their other dimensions, which can only resist tensile and compressive forces.[50,51]

In this thesis, we focus on the membranes, which are identified as a special kind of shell incapable of conveying shear loads. In other words, bending can be ignored in membranes. To further understand the mechanics in membranes, we can consider a part of a spherical shell of radius R and thickness t, under a uniform pressure of P. The compressive direct stress is

$$\sigma = -\frac{PR}{2t} \tag{3.4}$$

The shell bending moment is

$$M = -\frac{Pt^2}{24} \tag{3.5}$$

So, the bending stress is given by

$$\sigma_b = -\frac{P}{4} \tag{3.6}$$

We can derive the ratio of the direct stress to the bending stress

$$\frac{\sigma}{\sigma_b} = \frac{2R}{t} \tag{3.7}$$

Therefore, we can ignore the bending stress if the in plane stress is much greater than the bending stress as $(t/2r) \ll 1$. In 2D membranes, t is the atomic thickness with a few angstroms and r is usual of micron size, leading to the ratio between 10^3 and 10^4. Hence, we assume the bending stress is negligible in the 2D membranes.

3.2 Bulge Test

During the last 50 years, the bulge test has become a standard technique for measuring mechanical properties in thin film membranes.[52] Beams and his coworkers made an early measurement of mechanical properties in thin films with bulge test and the calculation of stress and strain in the bulged film.[53] Their calculation starts with an assumption of a spherical cap, in which t is the thickness of the thin film, R is the bulge radius of the spherical curvature, P is the applied pressure difference, σ and ε are the stress and strain, respectively. As derived in equation 3.4,

$$\sigma = -\frac{PR}{2t} \tag{3.8}$$

in the spherical cap, the spherical curvature R can be replace by bulge height z, and the film radius a if $z \ll a$,

$$R \approx \frac{a^2}{2z} \tag{3.9}$$

By plugging (3.9) into (3.8), we have

$$\sigma \approx -\frac{Pa^2}{4tz} \tag{3.10}$$

With the same assumption ($z \ll a$), we can derive the strain in the membrane as

$$\varepsilon = \frac{R\vartheta - a}{a} \approx \frac{a^2}{6R^2} = \frac{2z^2}{3a^2} \tag{3.11}$$

In the bulge test, the membrane can be considered to be under uniform biaxial stress, we can get the stress and strain relationship on the isotropic material as

$$\sigma = \frac{E}{1 - \nu}\varepsilon \tag{3.12}$$

For the simplest case of an initially flat, unstressed membrane, we can have the pressure-displacement relationship for an elastic material by combining (3.8), (3.11) and (3.12),

$$P = \frac{8Etz^3}{3a^4(1-v)} \tag{3.13}$$

When there is an initial tension S_o on the membrane, where tension is defined as $S = \sigma t$, becomes

$$P = \frac{8Etz^3}{3a^4(1-v)} + \frac{4S_o z}{a^2} \tag{3.14}$$

Hencky first developed an analytical solution for the bulge test culminating a relationship between pressure difference across the membrane and the maximum deflection of the bulge.[54,55] The analysis starts with the equations in their axisymmetric form for circular membranes are as follows,

$$\sigma_r \frac{dw}{dr} = \frac{pr}{2} \tag{3.15}$$

$$\sigma_t = \frac{d(r\sigma_r)}{dr} \tag{3.16}$$

Here, σ_r and σ_t are radial and tangential components of the membrane stress respectively, r is the radial coordinate, p is the pressure load acting on the membrane, and w is the deflection. The membrane stresses are related to their respective membrane strains ε_r and ε_t through

$$\varepsilon_r = \frac{1}{Et}(\sigma_r - v\sigma_t) = \frac{du}{dr} + \frac{1}{2}\left(\frac{dw}{dr}\right)^2 \tag{3.17}$$

$$\varepsilon_t = \frac{1}{Et}(\sigma_t - v\sigma_r) = \frac{u}{r} \tag{3.18}$$

22

where u is radial displacement, and equations (3.15) through (3.18) can be reduced to one single equation in σ_r given by

$$\sigma_r^2 \frac{d}{dr}\left(r^3 \frac{d\sigma_r}{dr}\right) = -\frac{Etp^2}{8}r^3 \qquad (3.19)$$

Then Hencky gave a series solution to (3.19) for clamped circular membranes. He assumed that the solution to this equation follows the form

$$\sigma_r = \left(\frac{Etp^2 a_0^2}{64}\right)^{\frac{1}{3}} \sum_{n=0}^{\infty} A_{2n}\left(\frac{r}{a_0}\right)^{2n} \qquad (3.20)$$

where, a_o is radius of the circular region of the membrane being pressurized, A_{2n} is nth coefficient. By plugging (3.20) into (3.8) and equating terms on the left hand side with those on the right hand side in the resultant algebraic equation, he got $A_2 = -A_0^{-2}, A_4 = -\frac{2}{3}A_0^{-5}, A_6 = -\frac{13}{18}A_0^{-8}$ etc. The boundary condition of $u = 0$ at $r = a_0$ gives A_0. Once an approximate description of the radial stress is obtained, it is easy to obtain the relation between the maximum deflection and pressure difference across membrane

$$\delta = w(r = 0) = C_1 \left(\frac{pa_0^4}{Et}\right)^{\frac{1}{3}} \qquad (3.21)$$

where C_1 is a constant. Or, we can express the equation as

$$p = C_2 \frac{Et\delta^3}{a^4} \qquad (3.22)$$

Similarly, with an initial tension, *So,* the equation further becomes

$$p = C_2 \frac{Et\delta^3}{a^4} + \frac{4S_o\delta}{a^2} \qquad (3.23)$$

For 2D membranes, since t is very small, the second term dominates when the deflection is small.

3.3 Contact Adhesion

Contact adhesion is an essential mechanical property of 2D materials and an interesting area of study. Due to their atomic thickness and resulting incomparable flexibility, 2D membranes can conform to the contacting surface much better than bulk materials, thereby increasing the contact area and adhesion significantly. The measured contact adhesion energy on graphene is comparable to that of a liquid-solid interface.[56,57] The ultrastrong contact adhesion also plays an important role in the 2D materials and devices from them, especially nanomechanical devices.[58] Take the NEMS switches as an example: the adhesion can help the membrane self-clamp over the trenches or cavities, which helps simplify the fabrication process; on the other hand, a restoring force in the device, determines the required actuation electrical voltage, and needs to overcome the contact adhesion between 2D membranes and the underneath electrodes. This is necessary to guarantee repeatable switching. Therefore, the ultrastrong contact adhesion can result in an undesirably high actuation voltage for the device to repeatedly switch. How to make a reliable NEMS switches with low actuation voltage requires the development of approaches to decrease the contact adhesion force.

3.4 Blister Test

Other than traditional methods to measure the contact adhesion in thin films/membrane, including peel test, pull test, and scratch test, the blister test turns out to be a widely used approach to probe the adhesive property, especially in 2D membranes, due to the ease of

implementation and film preparation.[55,56,59–61] The standard spherical blister test has the same configuration as that used in bulge test, but when the pressure difference across the member is greater than a critical value the membrane starts to delaminate from the substrate. Recently, Steven Koenig et al. used a constant N (# of gas molecules) spherical blister test to achieve stable delamination between graphene and SiO_2 substrate and the adhesion energy is calculated using a thermodynamic model to be 0.45 Jm^{-2}.[56,58] Narasimha Boddeti et al. applied constant N island blister test to get stable and unstable delamination of graphene from SiO_2 substrate, and the adhesion energy measured is comparable, though slightly lower ~ 0.1 Jm^{-2}.[62]

3.5 *Van der Waals Force*

The free energy of van der Waals interaction between a monolayer atomic membrane and a substrate can be derived by integration of pairwise potential energy for the atom-atom interaction based on Hamaker summation method.[63,64] The Lennard-Jones potential for the pair-wise interaction between one atom on the membrane and a substrate atom is

$$W_{LJ}(r) = -\frac{C_1}{r^6} + \frac{C_2}{r^{12}} \tag{3.24}$$

where C_1 and C_2 are the constant for the attractive and repulsive interactions respectively, while r is the distance between the atoms. By summing up the atom-atom potential for all the atoms in the membrane, we have the monolayer-substrate interaction energy, namely

$$W_{LJ} = \int_{A_g} \int_{V_s} W_{LJ} \rho_s \rho_g dV_s dA_g \tag{3.25}$$

Assuming the substrate has a flat surface while the monolayer membrane is flat as well, and they are in parallel, then we can get the analytic form of the interaction potential between the membrane and the substrate,

$$U_{vdW} = \Gamma_0 \left[\frac{3}{2} \left(\frac{h_0}{z} \right)^3 - \frac{1}{2} \left(\frac{h_0}{z} \right)^9 \right] \tag{3.26}$$

where U_{vdW} is the monolayer-substrate interaction energy per unit area, z is the distance between the monolayer and the substrate surface, h_0 is the equilibrium separation, and Γ_0 is the adhesion energy at the equilibrium separation.[65]

Accordingly, the van der Waals interaction can be obtained by taking the derivative of the interaction over z,

$$p_{vdW} = \frac{dU_{vdW}}{dz} = \frac{9\Gamma_0}{2h_0} \left[\left(\frac{h_0}{z} \right)^4 - \left(\frac{h_0}{z} \right)^{10} \right] \tag{3.27}$$

As an approximation, we can consider the attractive van der Waals interaction between a flat monolayer membrane and a flat substrate in unit area as this form

$$p_{vdW} = \frac{a}{z^4} \tag{3.28}$$

3.6 Electromechanical Actuation

Electromechanical actuation with electrostatic force is one of the most common ways to deflect or vibrate micro/nano mechanical structures.[66,67] When applying a voltage V on a capacitor, composed of a micro/nano mechanical structure and a gate electrode for example, the energy stored in the capacitor is

$$U = \frac{1}{2} CV^2 \tag{3.29}$$

where C is the capacitance. The induced electrostatic force is

$$F_e = \frac{dU}{dz} = \frac{1}{2} \frac{dC}{dz} V^2 \tag{3.30}$$

For capacitors with parallel plates, we have the electrostatic pressure as

$$p = \frac{\varepsilon_o \mathrm{K}}{z^2} V^2 \tag{3.31}$$

where ε_o is the dielectric permittivity of vacuum space, K is dielectric constant for the intermediate material.

3.7 Pull in Phenomenon

When we mention "pull in" or "snap through" phenomenon, we always think of the pull in instability in the parallel plate electrostatic actuators, where the actuator gets unstable and collapses at 1/3 of the original distance between the plates. In principle the instability occurs when the rate of change in voltage vs deflection distance is zero during electrostatic actuation. The 1/3 rule can be applied to electrostatic actuators in the form of cantilever, doubly clamped beam, or piston parallel plate.[66,68]

Similarly, the pull in instability in 2D membranes happens when the rate of change of pressure difference across the membrane Δp vs deflection h equals to zero.[69]

$$\frac{d\Delta p}{dh} = 0 \tag{3.32}$$

Here, Δp is not limited to the pressure difference from the input gas across the membrane, but can be combined with the pressures from electrostatic force, interfacial forces, etc.

3.8 Conclusion

This chapter review relevant nanomechanics in 2D materials for the experimental sessions. Next chapter includes a review of nanomechanical systems in terms of NEMS switches, measurement of interfacial forces, and strain engineering with 2D materials.

Chapter 4

Nanomechanical Systems: Review of NEMS Switches, Interfacial Forces and Strain Engineering

4.1   Nanoelectromechanical switches

The development of nanotechnology makes us reexamine one interesting idea - mechanical computing, which was proposed by Charles Babbage about two centuries ago. This idea was completely overwhelmed by the soaring progress in micro/nanoelectronics, which can be represented by Moore's law in last forty years postulated by Gordon Moore in 1965. It predicted that by scaling down the size of transistors, the number of transistors on a chip would roughly double every 18 months.[22] However, when we ultimately reach the scaling limit of semiconductor transistor, it might be time to reinvent the transistor.[70] A NEMS switch is one promising candidate.

As mentioned, the resonance frequency of NEMS can reach up to 10 GHz, thereby making NEMS based electromechanical computers potential viable alternative to work at an even faster speed than state of the art computers in the current market. NEMS switches can also have a low off-state current limited by Brownian motion and tunneling and high on/off ratio, which are great barriers for traditional semiconductor transistors when scaling down to tens of nanometers. Therefore, by means of mechanical computing with NEMS switches we could solve these problems, thus decreasing the power consumption for computing due to leak currents.

Another attractive attribute for NEMS switches is "harsh environment robustness", namely high temperature resistance and radiation hardness. Different from conventional semiconductor transistors, which function based on the electronic properties of semiconductor materials and interfaces, NEMS switches work with mechanical movement. The harsh environments, like high temperature and radiation, can easily affect the interfaces in semiconductor transistors but hardly influence the mechanical movement of nanostructures in NEMS. In sum, NEMS switches are capable of achieving virtually microwave operating frequencies, zero off-state current, high temperature resistance, and radiation hardness. These are attractive advantages over existing complementary metal-oxide semiconductor field-effect transistors.

4.1.1 Graphene Based NEMS Switches

Carbon based nanomaterials including fullerene, graphene and carbon nanotube (CNT) have resulted in two Nobel Prizes and are considered as one of the most attractive elementary materials in the nano world due to their incredible properties in mechanical, electrical, thermal, and even biological fields. Here, I will review the NEMS switches from graphene and CNT, which are the 2D and 1D carbon materials, respectively.

The first graphene NEMS switch was developed by Jing Kong's group in MIT.[71] The device was fabricated by deposition of two layers of graphene separated by a 500 nm gap. The top layer was etched into a 3 μm wide strip suspended over a 20 μm wide trench, and it can deflect and contact the bottom layer by applying ~5 V voltage between them. The schematic and SEM image of the device is shown in Figure 4.1. This first NEMS switch from graphene functioned unreliably, and failed due to tears on CVD graphene after several times of switching.
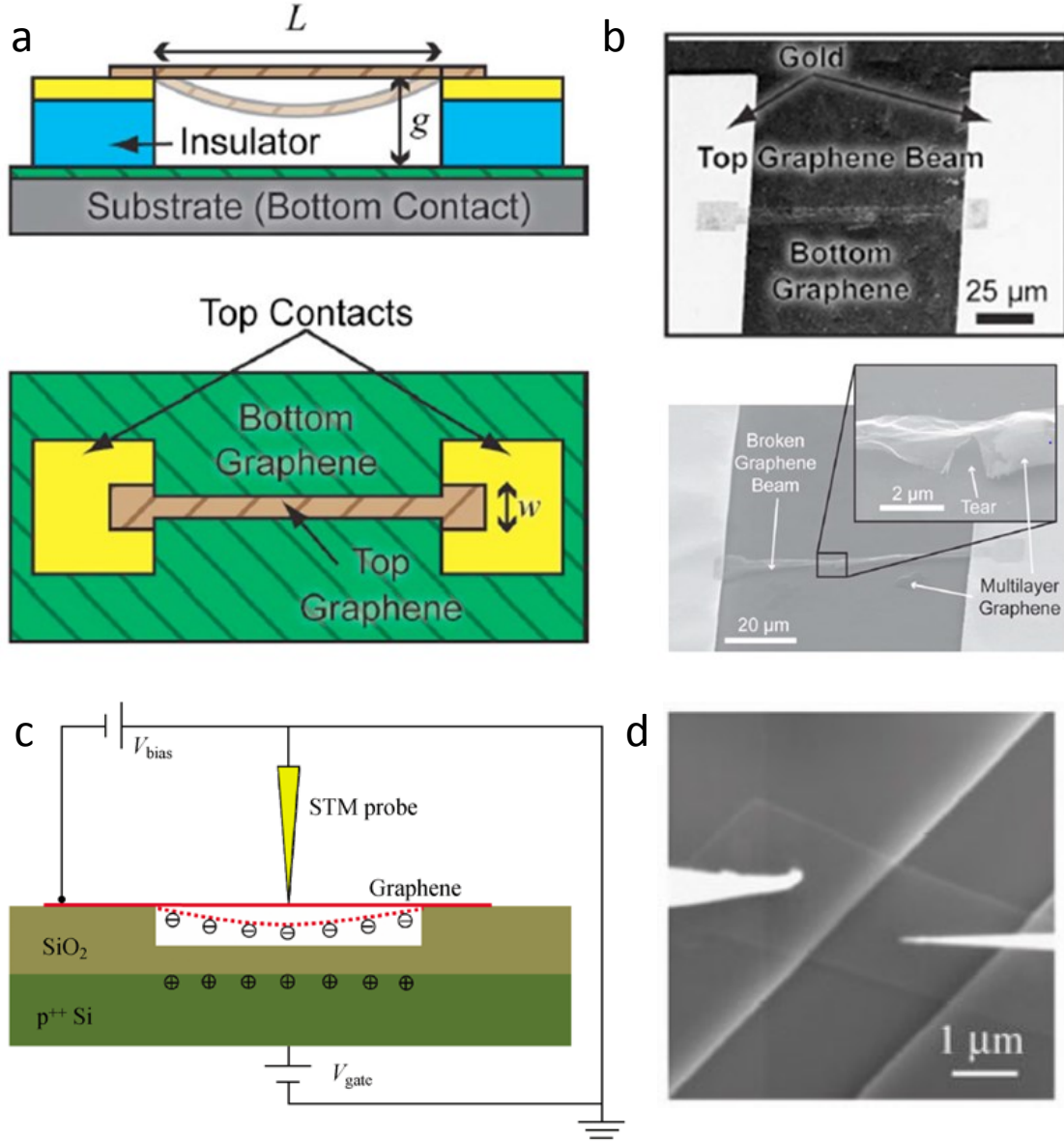
Figure 4.1Graphene NEMS switches a) Schematic diagram of an all CVD graphene switch from a cross sectional view and a top view. b) SEM images of suspended graphene and tear on graphene.[71] c) Schematic of the 3-terminal graphene switches with a STM probe. d) SEM image of the device.[72]

Kang Wang' group improved the fabrication, and suspended a strip of CVD graphene over a smaller trench of 20 μm width and 150 nm depth.[73] This graphene switch can work at actuation voltages of 1.85 V, which is compatible with conventional complimentary metal-oxide-semiconductor (CMOS) circuit requirements. They also reported abrupt on/off characteristic, demonstrating fast response from the device.

G. Zhang's group tried to make a three terminal graphene switch from exfoliated graphene using a similar geometry as previous devices but with a 100 nm wide gold electrode patterned by e-beam lithography in a 2 μm x 0.15 μm trench.[72] However, the switches with this geometry suffered restoring failure due to a strong van der Waals force when graphene touches the electrode even though the electrode is only 100nm wide. They also designed a multilayer graphene NEMS switch with a "point" contact based on their studies on the former graphene NEMS switches. Through quantitative study of the vdW force on graphene and restoring force by sticking and unsticking graphene with an AFM tip, they realized the monolayer graphene device will not recover unless the gold wire width is less than 5nm. They also studied the mechanical robustness of monolayer graphene, and found the monolayer is easy to tear making it not as good as multilayer graphene for NEMS switches. Therefore, "point" contact graphene NEMS switches from multilayer shows potential for greater reliability. Instead of a gold wire as the drain electrode, they used an STM probe with contact area ~150 nm^2, which can lead to ~60 nN probe-graphene vdW force, reflected by the 15 V threshold voltage. The point switch can work over 500 cycles, the most ever reported.

Different from the mechanism of the switches with doubly clamped beam structure, graphene switches developed by Marc Bockrath's group operate based on the formation and breaking of carbon atomic chains that bridge the graphene break junctions.[74] Geometrically, it is
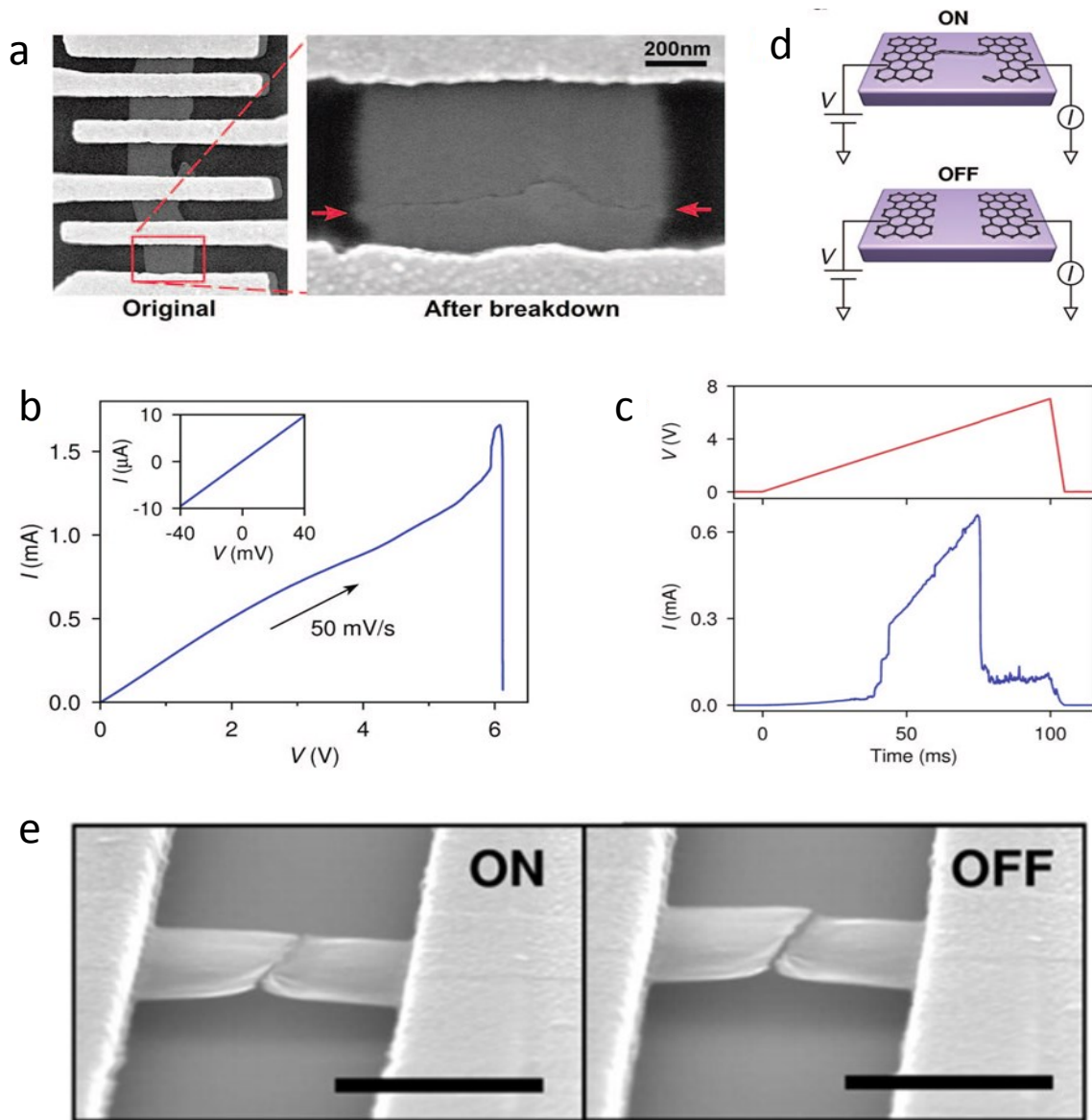
Figure 4.2   a) SEM image showing the breakdown of graphene. b) Electrical measurement showing the breakdown of graphene. c) Electrical measurement of graphene atomic switch. d) Schematic showing the atomic switching of the device.[74] e) The SEM images of ON and OFF state for the atomic switch with suspended graphene. The scale bar is 1 μm.[75]

like a lateral switch. The switches are fabricated by creating nanoscale gaps using electrical breakdown of graphene sheets-a reliable self-limiting process that avoids the need for advanced lithographic technique. Applying appropriate bias voltage pulses switches the gap conductance between high (ON) or low (OFF) conductance states.

Figure 4.2a shows an SEM image of a graphene switch after the formation of a break junction by a voltage pulse of 1.5 V. The breaking down of the graphene sheet is also supported by the IV curve, which is shown in Figure 4.2b. After the voltage increases to 1.5 V, the current decreases suddenly which indicates the breaking of the graphene sheet. After the fabrication of the device with a broken junction, when the voltage is smaller than 2 V, the current is very low; when it reaches ~2.5 - 4 V, the current abruptly increases, reaching a maximum of 0.65 mA at ~5 V. However, with further increase of voltage, the conductance returns to its initial low-conductance state. A typical switching IV curve is shown in Figure 4.2c. They proposed a model for the switch, which claims the devices switch on and off by alternative formation of carbon atomic chains bridging the breaking junction due to the voltage applied (Figure 4.2d). Therefore, by applying voltages of different magnitudes, the graphene devices can be switched into ON and OFF states, thereby functioning as voltage programmable bi-stable switches or memory elements.

To rule out the influence of the substrate, which can also bridge the breaking gap electrically, they also fabricated suspended atomic switches from graphene.[75] Interestingly, the graphene cantilevers after the breaking process can stay suspended considering their low bending rigidity. Furthermore, the graphene break junction switch on/off similar to those staying on silicon oxide substrates.
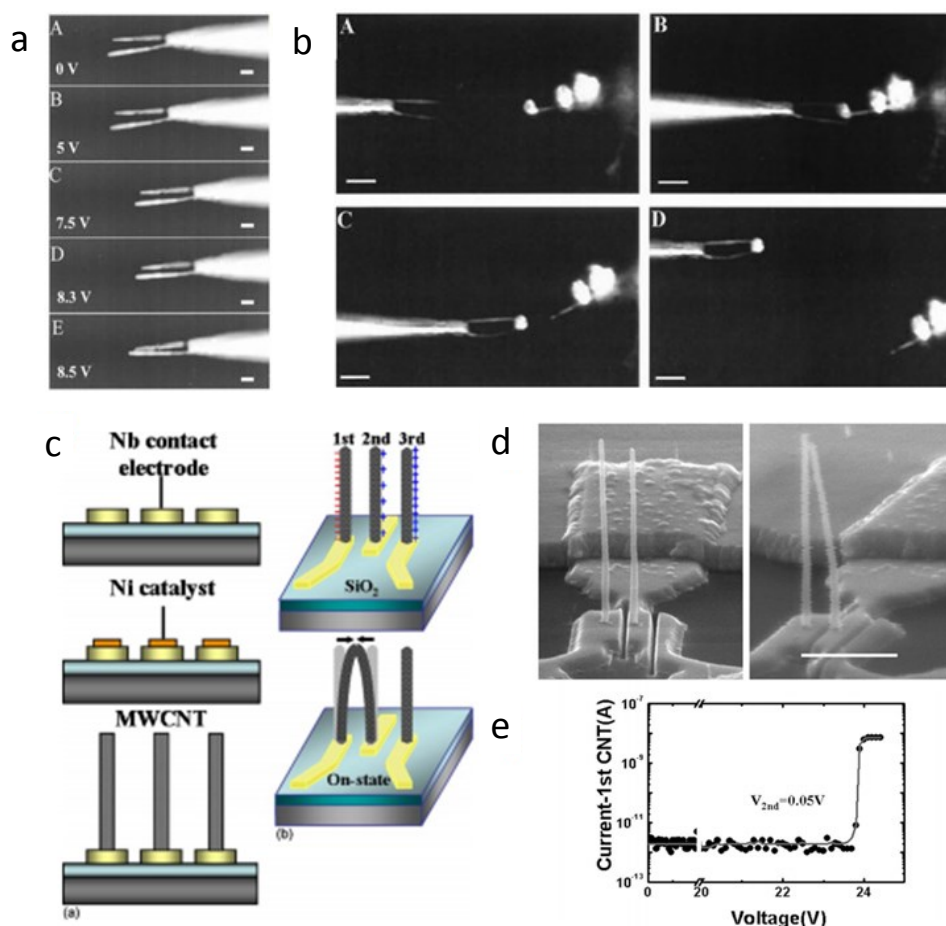
Figure 4.3 a) (A through E) Dark-Field optical micrographs of the nanotube arms at potentials of 0, 5, 7.5, 8.3, and 8.5 V, respectively. Scale bars, 1 mm. b) Dark-field optical micrographs showing the sequential process of nanotweezer manipulation of polystyrene nanoclusters containing fluorescent dye molecules.[76] c) A schematic illustration of the CNT-based electromechanical switch device. d) SEM image of the device: The length and diameter of the MWCNTs are about 2 μm and 70 nm, respectively. e) Current-voltage characteristics of switching action in an ambient environment; the electromechanical movement of MWCNTs provides the on and off states. The scale bar corresponds to 1 μm.[77,78]

4.1.2 Carbon Nanotubes Based NEMS switches

A CNT can be considered a more complicated form of carbon where a strip of graphene is wrapped into a tube shape. However, CNTs were discovered several decades earlier than graphene, and CNTs were applied into NEMS about one decade earlier. As a 1D material, CNT demonstrates different mechanical properties from graphene. Prominent of them is a considerable bending rigidity, which makes cantilevers of CNT be promising structures for NEMS switches as well.

CNT nano-tweezers reported by Philip Kim and Charles Lieber is one example of the earliest CNT based cantilever switches.[76] It is fabricated by attaching two CNT to independent electrodes fabricated on pulled glass micropipettes. Similar to tweezers used in daily life, the CNT nanotweezers can grab and manipulate submicron clusters and nanowires. It works by deflecting the two CNT cantilevers actuated by electrostatic force between them. Different from typical MEMS/NEMS with only one movable part for one device, both CNT cantilevers can deflect. Reported actuation voltage is ~8.5V.

Based on the work on nanotweezers, Jang from Amaratunga's group demonstrated NEMS switching from a similar device.[77] Vertical CNTs cantilevers are grown in situ on Ni catalyst dots via a CVD bottom-up process. In this way, large arrays of device fabrication and integration become feasible. The original device reported in 2005 had a pull-in voltage of ~24 V, but decreased down to ~4.5 V after improvements.[78] This kind of CNTs vertical cantilever NEMS switches show great potential as mechanical transistors, logic devices, and non-volatile memory cells, and RF NEMS applications.

S. W. Lee et al. demonstrated three terminal NEMS switches from multiwall CNTs (MWNTs) in a horizontal geometry instead. The device switches by deflecting the CNT
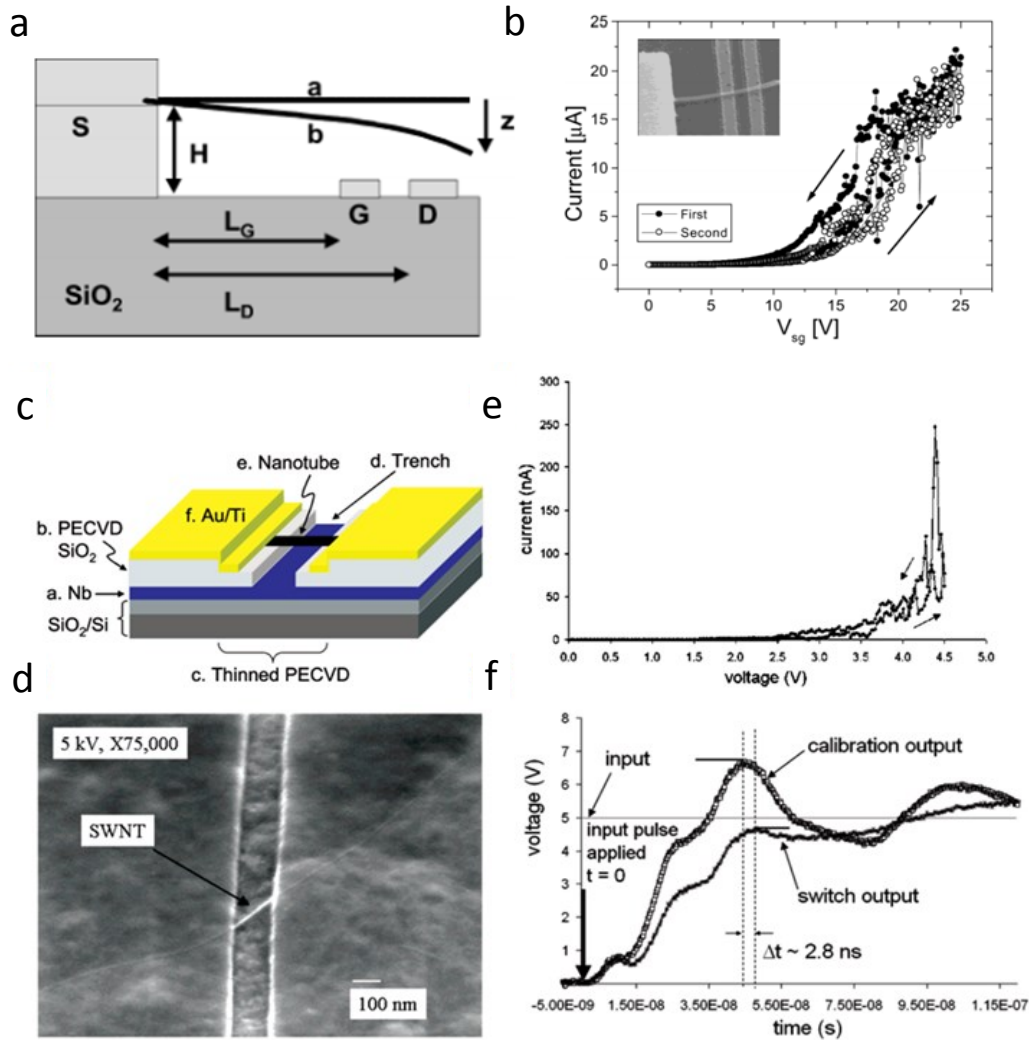
Figure 4.4 a) Schematic diagram of the carbon nanotube relay, b) IV characteristics of a nanotube relay initially suspended approximately 80 nm above the gate and drain electrodes. V_{sd} = 0.5 V.[79] c) Schematic of the device. d) SEM image of the device. e) IV characteristic of the device. f) Response time measurement showing the response time equals 2.8 ns.[80]

cantilever with a gate voltage to contact the drain electrode. I-V_{sg} characteristics of a nanotube relay initially suspended approximately 80nm above the gate and drain electrodes showed a nonlinear increase of current as the gate voltage increased when $V_{sg} < 20$ V, but the linear current increase and strong fluctuations are seen for $V_{sg} > 20$ V. The V_{sd} was 0.5 V. They observed some hysteresis effect on the restoring of CNTs when decreasing the gate voltage, which might be utilized for nonvolatile memory applications.

When clamped on both ends, the CNT can exhibit higher tension after deflection, thereby increasing the restoring force and response rate. A.B. Kaul et al. studied the switching speed of the doubly clamped NEMS switches from single walled nanotubes (SWNTs), and showed that the CNT switches measured to be 3 orders of magnitude faster than MEMS switches, with a switching time of 2.8 ns while requiring pull-in voltages less than 5 V.[79] Some other researchers also used arrays of horizontally aligned CNTs for NEMS switches, which show similar switching properties.[81,82]

4.1.3 Thin film lateral NEMS Switches

The other major way to make NEMS is to etch traditional MEMS material like single crystal or poly silicon into submicron thin film movable structures, and switch them laterally over tens of nanometer gaps by electrostatic force. It is a lot easier to fabricate wafer scale arrays of devices and to integrate into complementary metal oxide semiconductor integrated circuits (CMOS IC) with this method than application of nanomaterials (CNTs or graphene), even though the submicron structures can hardly be scaled down further due to the decay of mechanical robustness by defects.
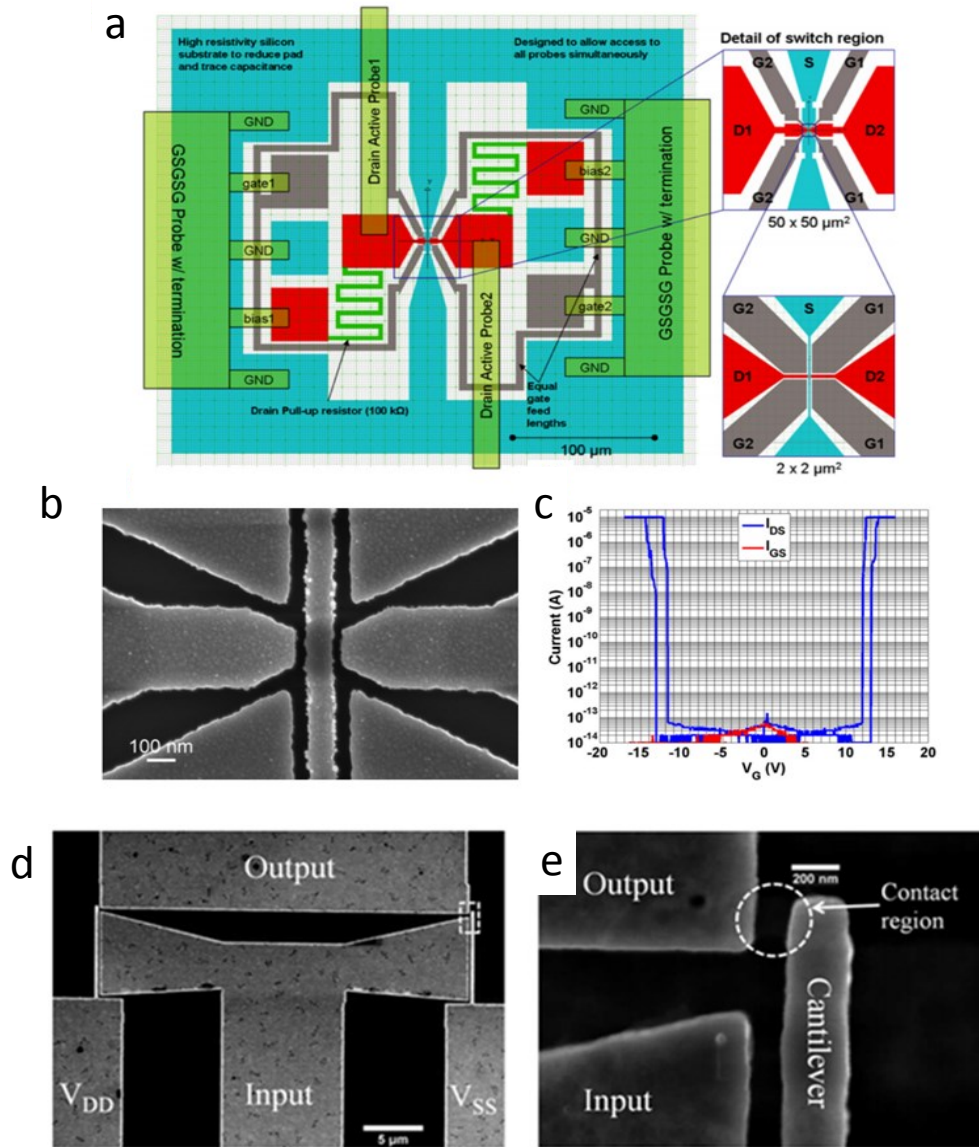
Figure 4.5   a) Layout design of the lateral switch, b) SEM image of the device, c) IV characteristic of the device.[83] d) & e) SEM image of SiC NEMS inverter.[11]

One of the earliest examples is a Ruthenium thin film NEMS switches developed by David. A. Czaplewski et al.[83] A layer of 200 nm thick ruthenium film is deposited by sputtering (210 W DC power, 50 W substrate bias, 4.6 mTorr, 25°C). The Ruthenium thin film is etched by high density plasma RIE (15 mTorr, 10 sccm Cl_2, 90 sccm O_2, 500 W upper power, 200 W lower power) into designed shape with a 50 - 100 nm wide and 3 - 10 μm long beam separated from gate electrode with 30 – 100 nm, and drain electrode 20 - 70 nm masked by a layer of PECVD SiO_2. A typical switch can pull in at ~5 V with a measured switching time of ~400 ns. The maximum lifetime measured is approximately two million cycles tested at a 1 kHz cycle frequency. Furthermore, all processing in the fabrication is CMOS compatible.

T Lee from M. Mehregany's group developed SiC NEMS switches operating at 500°C, at which the mature silicon FET technologies fail due to excessive leakage caused by p-n degradation and thermoionic leakage. Heavily nitrogen-doped ($N_D \sim 1x10^{20}$ cm^{-3}) polycrystalline 3C-SiC films are deposited on the silicon wafer[11]. Assembling two SiC NEMS switches together, they made an inverter, a fundamental element for electromechanical computing. The length, width, and actuation gap of the cantilevers are ~8 μm, ~200 nm, and 150 nm, respectively. Typical switches measured have operated $\geqq$21 billion cycles at 25 °C and $\geqq$2 billion cycles at 500 °C.

Howe's group at Stanford is working on the polysilicon lateral NEMS. About 1.2 μm thick polysilicon with 50 nm sputtered platinum is used as the thin film for movable beam and electrodes. They designed a strategy to separate the mechanical and electrostatic domains, yielding individual control of the pull-in voltage and electrode displacements, enabling the device to be more robust against the shorting of the beam to gate.[84] They realized that an electrically connected beam and drain has several drawbacks, cascading these three terminal

lateral switches, necessary for digital circuits, requires the sustainable voltage across the contact to be greater than or equal to the pull-in voltage. To solve the problem, they add a DC bias electrode that partially actuates the beam towards the drain and isolating the beam to form a conductive channel that connects the source and drain electrodes when the relay is in the ON state.[85]

4.1.4 NEMS memories

The consumer electronics industry is rapidly transitioning to mobile electronics from the dominance of mature home electronics. The uprising of smart phones is the most obvious example of electronic gadgetries that are filling consumers' pockets. Flash memory has enabled the widespread use of these mobile devices by providing storage for the increasing amount of user data that must be carried.[86]

Current memory technologies, such as DRAM, SRAM, and NAND flash, are approaching very difficult issues related to their continued scaling to and beyond the 16nm generation.[87] Fortunately, research over the past ten-fifteen years has led to discovery of several new memory technologies, holding the promise for further continuing scaling. These emerging research memory technologies include the Ferroelectric-gate FET, NEMS RAM, Nanowire phase change memory, electronic effects memory (ie. Charge trapping, mott transition, ferroelectric barrier effects), macromolecular and molecular memory, and nanoionic or redox memory (including the fuse/antifuse memory and related electrochemical metallization, programmable metal cell and the atomic switch).[87] As one recognized promising memory technology, NEMS nonvolatile memory has a host of advantages, such as high response speed due to high resonance frequency, low power consumption due to small size, harsh environment

operation due to the switching mechanism of mechanical movements. The potential density of thin film NEMS reaches up to 10^{12} elements/cm^2.

T. Rueckes et al. proposed a CNT based nonvolatile random access memory for molecular computing.[13,87] In their design, each memory element is based on a suspended, crossed nanotube geometry that leads to bistable, electrostatically switchable ON/OFF states. Bistability can be envisioned as arising from the interplay of the elastic energy, which produces a potential energy minimum at finite separation, and the attractive van der Waals energy, which creates a second energy minimum when the suspended SWNT is deflected into contact with the lower nanotube. An element could be switched between well-defined OFF and ON states by transiently charging the nanotubes to produce attractive and repulsive electrostatic forces. The ON/OFF information at an element thus can be read easily by measuring the resistance of the junction and moreover, can be switched between OFF and ON states by applying voltage pulse at electrodes n and m. This approach suggests a highly integrated, fast and macroscopically addressable nonvolatile random access memory (RAM) structure that could overcome the fundamental limitations of semiconductor RAM in size, speed, and cost. From the calculation, the minimum magnitudes of the voltages required for switching ON and OFF are 4.5V and 20V, respectively.

4.2 Theories and Measurements of van der Waals Forces in Nanomechanical Systems

Van der Waals bonding is considered as a secondary bonding compared to primary ones such as ionic bonding, covalent bonding, and metallic bonding.[49] This secondary bonding force arises from atomic or molecular dipoles, which instantaneously exist whenever there is some

separation of positive and negative portions of an atom or molecule. In essence, the bonding force therefore results from the columbic attraction between the positive end of one dipole and the negative region of an adjacent one.

Van der Waals force is a universal force, acting between all atoms and molecules, even between totally neutral ones such as inert gases, carbon dioxide, and hydrocarbons. Accordingly, it plays a significant role in a host of phenomena like adhesion, surface tension, physical adsorption, the properties of gases, liquids, gels, and thin films, and the structures of condensed macromolecules such as proteins and polymers. Van der Waals force analysis is widely considered in the fields of atomic physics, material science, biomedical engineering, chemistry, and others.[64]

4.2.1 Theories on van der Waals Forces

J.D. Van der Waals first introduced intermolecular forces theoretically to explain the behavior of non-ideal gases in 1873. This kind of force, as we know, was named as van der Waals force later. London (1930, 1937) first published a satisfactory microscopic theory about van der Waals force considering it as dipole-dipole interactions between two neutral atoms based on quantum mechanics considering the perturbation in their zero-point energy, even though the mechanism of vdW force is much complicated considering many different interactions.[88,89] By treating the dipoles as isotropic harmonic oscillators of characteristic frequencies of ω_1 and ω_2 and polarizabilities α_1 and α_2, he showed that the potential energy between two dipoles with a distance d apart as:

$$U = -\frac{3\hbar}{2}\frac{\varpi_1\varpi_2}{\varpi_1+\varpi_2}\frac{\alpha_1\alpha_2}{d^6} \tag{4.1}$$

For the oscillating dipoles, when time taken for the electrostatic field of one instantaneous dipole to reach the neighboring atom and return is comparable to the fluctuating period itself, the power law of force changes because the first atom is no longer in phase with its neighbor atom. This interaction is now known as the retarded van der Waals interaction. Casimir and Polder (1948) showed that for separations greater than $\lambda_i/2\pi$, where λ_i is the characteristic absorption wavelengths, there is a progressively reducing correlation between the polarizations of neighboring atoms as distance increases, and the potential energy for two atoms with polarizabilities α_{10} and α_{20} follows,

$$U = -\frac{23}{4\pi}\hbar_c\frac{\alpha_{10}\alpha_{20}}{d^7} \tag{4.2}$$

This equation means that the non-retarded power law changes from $1/d^6$ to the retarded $1/d^7$ when the distance d increases above $\lambda_i/2\pi$.[90] This power law change effect due to distance was named as the Casimir-Polder effect.

The limit with two former theories is the ignorance of the influence from neighboring atoms on the interaction of the pair of atoms. However, the consideration of this effect can make the problem very complicated, a typical case with quantum mechanics. This problem was solved with the macroscopic theories, which ignored the atomic structures but consider bulk properties such as dielectric constants.

Lifshitz, Dzyaloshinskii, and Pitaevskii first put forward a macroscopic theory to obtain the dispersion force between two flat parallel plates 1 and 2 separated by distance D by a third medium 3 by applying the methods of modern quantum field theory.[91] For non-retarded forces, the force per unit area f follows,

$$f = \frac{\hbar}{8\pi^2 D^3} \int_0^\infty \sum_{n=1}^\infty \frac{1}{n^3} \left[\left(\frac{\varepsilon_1 - \varepsilon_3}{\varepsilon_1 + \varepsilon_3} \right) \left(\frac{\varepsilon_2 - \varepsilon_3}{\varepsilon_2 + \varepsilon_3} \right) \right]^n d\xi = \frac{A_{123}}{6\pi D^3} \qquad (4.3)$$

Where $\varepsilon_j = \varepsilon_j (i\xi)$ is the dielectric constant (or permittivity) of the jth medium as a function of an imaginary frequency $i\xi$, and A is the Hamaker constant for non-retarded forces. In the case of most dielectrics the first term of above equation constitutes about 98% of the total value of f.

For retarded forces, the theory gives

$$f = \frac{\pi^2 \hbar c}{240 D^3} \frac{1}{\varepsilon_{30}^{\frac{1}{2}}} \left(\frac{\varepsilon_{10} - \varepsilon_{30}}{\varepsilon_{10} + \varepsilon_{30}} \right) \left(\frac{\varepsilon_{20} - \varepsilon_{30}}{\varepsilon_{20} + \varepsilon_{30}} \right) \phi(\varepsilon_{10}, \varepsilon_{20}, \varepsilon_{30}) d\xi = \frac{B}{D^4} \qquad (4.4)$$

where $\varepsilon_{10}, \varepsilon_{20}, \varepsilon_{30}$ are the static dielectric constants, and $\Phi (\varepsilon_{10}, \varepsilon_{20}, \varepsilon_{30})$ is a function whose value lies between 1 and $69/2\pi$. B is the Hamaker constant for retarded forces.

4.2.2 Early Measurements of van der Waals Force

Early experimental measurements of van der Waals force were done by Derjaguin and his colleagues in Russia (for example Derjaguin, Lifshitz, and Abrikossova 1956), Sparnaay (1952, 1958), Holland, and Kitchener & Prosser (1957) in Britain.[92–94] The common point their methods shared is to position two bodies close together and to measure the force of attraction as a function of the distance between them. Most measurements carried out at that time were of this type: the bodies were made of glass or other transparent material, the force was determined by measuring the deflection of a balanced arm, and the distance between the highly polished surfaces obtained by optical interference.

The first direct experimental check of the theory of molecular forces of attraction between condensed bodies was done by Derjaguin's work in 1957.[94] Molecular attractions between quartz-quartz, mixed thallium halide-mixed thallium halide, and chromium-quartz in a

range of gap widths from 0.07 to 0.3 microns were measured. The results agreed with the values derived from Lifshitz's theory. The best results on glasses are from the Dutch school in Holland (Black, de Jongh, Overbeek & Sparnaay (1960); Sparnaay & Jochems (1960); Van Silfhout (1966); Rouweler & Overbeek (1971)). In Rouweler & Oberbeek's work (1971), the dispersion force between a fused silica glass lens and a flat in the range 25 to 350 nm were measured.[88,92] They observed retardation effect above 50 nm, while at shorter distances a transition towards non-retarded forces was detected.

There are three main problems with most of those early works:

(1) Electrostatic charges on the surfaces gave rise to spurious results. In some experiments, forces measured are several orders larger than theoretical values.

(2) When surfaces are so close to each other at the order of 5-20 nm, the impurities like small dust particles or silica gel can prevent the measurement at separations smaller than several tens of nanometers.

(3) Vibrations from the surrounding always found their way into the sensitive moving parts of the apparatus and could never be completely suppressed.

To solve these problems, Israelachvili measured the van der Waals force using two crossed cylindrical sheets of muscovite mica, which can be considered molecularly smooth at the surfaces.[88] The distance between surfaces was measured to about ±0.2nm precision by allowing white light to pass through them and observing the interference fringes spectrometrically. The van der Waals forces were measured by two different methods: (1) by the 'jump method', in the range of 1.5 to 20 nm and (2) by the 'resonance method', in the range 10 to 130 nm. The experimental setup is shown in Figure 4.6a.
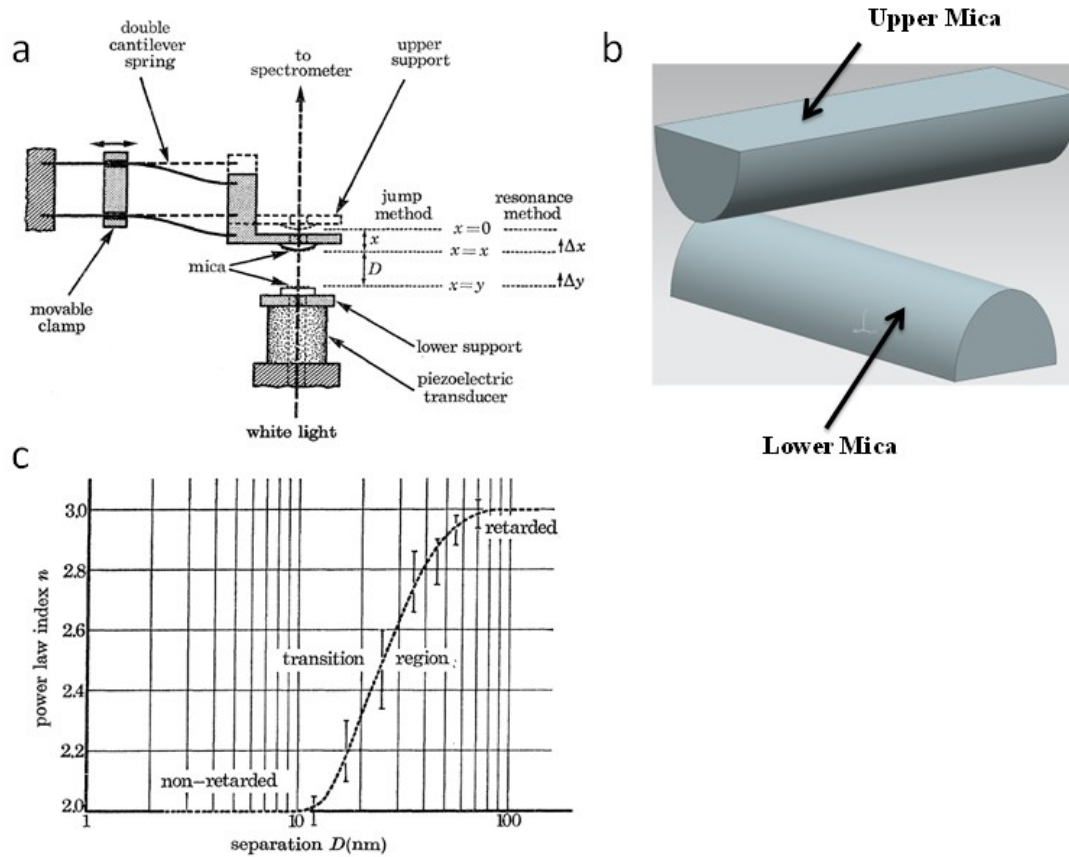
Figure 4.6 a) Schematic drawing on the main parts of the apparatus for van der Waals force measurement. In jump experiments a double cantilever spring was used. In resonance experiments a single cantilever "bimorph" spring was used. b) 3D rendering of the half mica cylinders. c) Variation of the power law of the van der Waals force between crossed mica cylinders with distance D. The curve is based on the combined results of a number of jump and resonance experiments.[88]

The upper glass section is fixed at the end of a double or single cantilever spring. The lower surface can be moved close to the upper one with a piezoelectric transducer. At some distance, the two parts will jump into contact (snap in) depending on the stiffness of the spring. The force can be calculated by the measurement of the jumping distance based on the 'jump' (snap in) condition:

$$dF = -\frac{n\zeta}{D^{n+1}}dD - Kdx = 0 \tag{4.5}$$

Because $dx = -dD$, this gives the jump distance D_o as

$$D_0 = \left(\frac{n\zeta}{K}\right)^{1/(n+1)} \tag{4.6}$$

The principle of the resonance method is to measure the resonant frequency f_D of the upper support as a function of the gap distance D, and from this to deduce the law of force in the range of distances measured. This method allowed relatively accurate measurement of van der Waals force ranging from 10 nm to 130 nm. From this experiment, Isrealachvili et al. observed both non-retarded and retarded van der Waals force, and most importantly, they found that the transition region between them at a distance from ~10 nm to ~100 nm. The result is shown in Figure 4.6c.

4.2.3 Measurements of van der Waals Force in Micro/Nanomechanical Systems

Due to the size scaling into submicron and nano region for applications of nano materials, van der Waals force becomes critically important for the performance and reliability of MEMS/NEMS devices based on these materials. In MEMS, adhesion (stiction) is a universal problem affecting the yield and reliability of devices.[95] The adhesion of the microstructure to

47

adjacent surfaces can occur either during the final steps of the micromachining process (release-related adhesion) due to the capillary force or after packaging of devices, due to electrostatic force from over-range input signals or strong van der Waals force or hydrogen bonding. The versatility of the reasons for adhesion makes it a complicated problem and a huge barrier for the industrialization of MEMS. Accordingly, adhesion problems became a research focus in the field of MEMS.

A common experimental technique to examine the surface-surface interaction involved in silicon microstructures is 'cantilever beam array (CBA) technique'. A scanning electron microscope picture of CBA is shown in Figure 4.7a. To measure the work of adhesion, the beams are brought into contact with the underlying substrate. Once the beams make contact with the underlying substrate, the applied actuation force is removed, and the beams will begin to peel themselves off the surface. For beams shorter than a characteristic length, their stiffness will be sufficient to free them completely from the underlying surface. Beams longer than this characteristic length, however, will remain adhered to the surface. The work of adhesion W, between two surfaces can be calculated as

$$W = \frac{3}{8} \frac{\xi h^2 t^3}{l_d^4} \tag{4.7}$$

where l_d is the characteristic detach length of the beams.

Based on the cantilever beam array technique, Delrio & Dunn studied the role of van der Waals in the adhesion of micromachined surfaces.[96] They experimentally measure adhesion on micro-cantilevers ranging from normal vdW to retarded vdW region as a function of surface roughness, and independently calculated the adhesion using the measured surface topography.
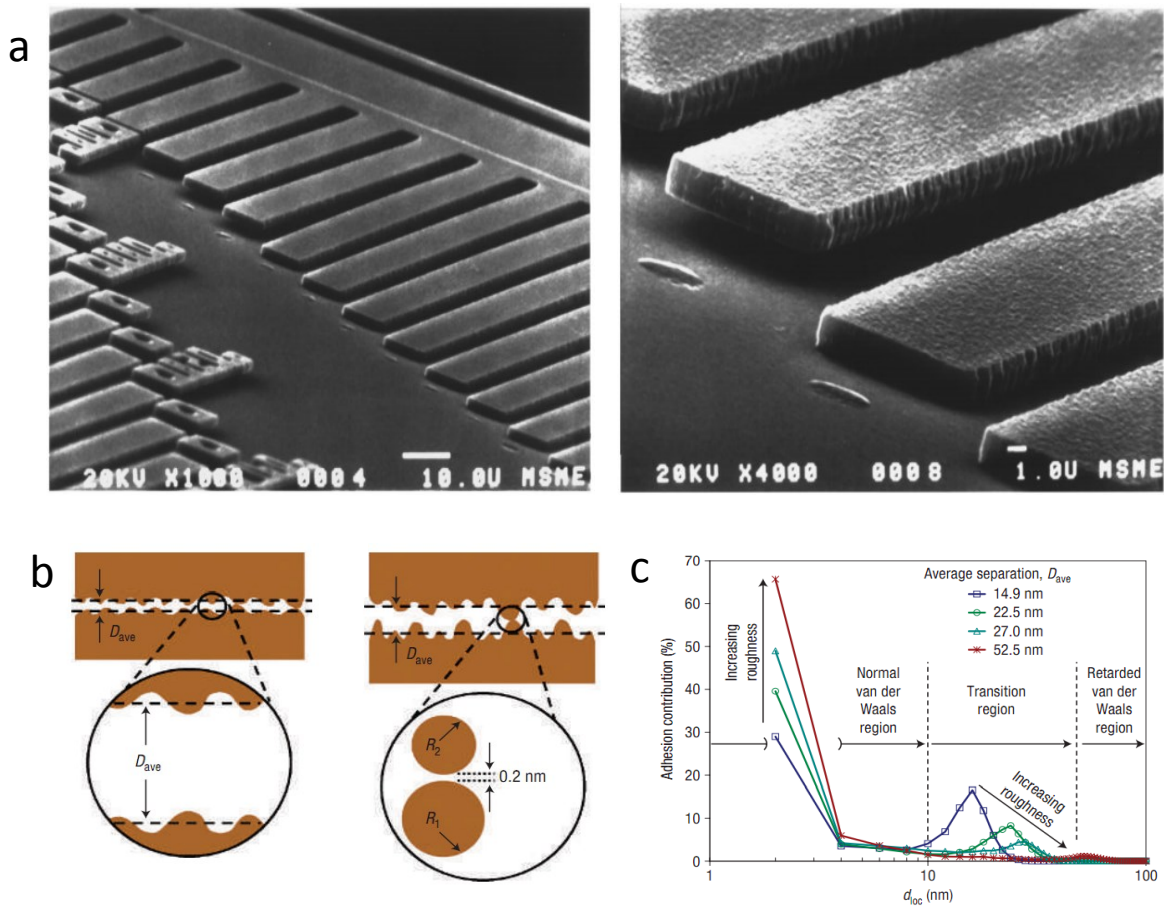
Figure 4.7 a) SEM images of cantilever beam arrays used in CBA technique.[95] b) In the first case (left), the surfaces are relatively smooth and forces across non-contacting portions of the surfaces will dominate the adhesion. In the second case (right), the surfaces are relatively rough, and normal van der Waals forces across asperities that nearly bridge the gap are the dominating contributor to the adhesion. c) The adhesion contribution histogram quantitatively shows the transition from the first case (smooth) to the second case (rough) as the landing-pad roughness is increased from 2.6 to 10.3 nm r.m.s.[96]

They demonstrated that the adhesion of micromachined surfaces with nanoscale roughness is in a regime not considered by standard rough surface adhesion models which were dealing with micro scale roughness. They also showed that the adhesion for surfaces with small roughness values was mainly due to the van der Waals force acting across extensive non-contacting areas and is related to $1/D^2_{avg}$, where D_{avg} is a result of the planar deposition technology, while for surfaces with large roughness values, van der Waals forces at contacting asperities becomes the dominating contributor to the adhesion.

Even before this systematic study of the relationship between van der Waals force and roughness of microstructure, people have intuitively tried to alleviate adhesion by roughening the surfaces of microstructure. While some improvements (a factor of 20) were achieved due to roughening, chemical modification of surfaces showed a better prospect, which can typically decrease the adhesion energy by a factor of 1000. The basic idea of surface chemical modification is to change the surface from hydrophilicity to hydrophobicity. Common methods include hydrogen terminating treatments with Si-H bond for silicon surfaces, self-assembled monolayers (SAM) coating, diamond-like carbon coating, and fluorocarbon film.[95]

Van der Waals forces seem always detrimental in MEMS devices because of their influence on performances and reliabilities, but it is not necessarily true. Chan & Capasso designed and fabricated a new kind of actuator – a MEMS torsional device actuated completely by the Casimir force.[97–99] The results not only demonstrated that this actuation method is feasible, but also provided one of the most sensitive measurements of the Casimir force between metalized surfaces. The measurement setup and results are shown in Figure 4.8.
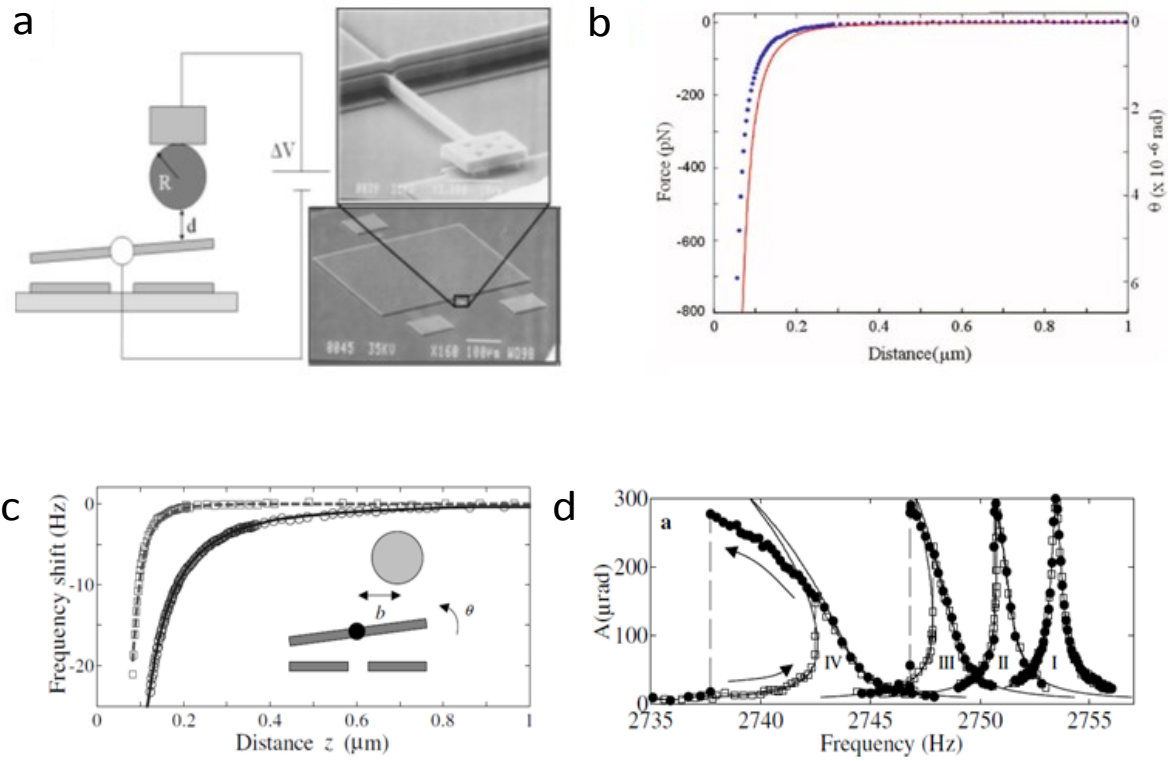
Figure 4.8 a) Schematic and SEM image of experimental setup. b) Van der Waals force measurement results from the experiment.[100] c) Change in resonance frequency of the oscillator in response to the electrostatic force and Casimir force as a function of distance. d)Hysteresis in the frequency response induced by Casimir force on an linear oscillator.[101]

Capasso's group also showed that the Casimir attraction force can influence the dynamical properties of a micromachined device, changing its resonance frequency and giving rise to hysteretic behavior and bi-stability in its frequency response to an AC excitation (Figure 4.8c & d), as expected for a nonlinear oscillator.[101] They also proposed that this device could serve as a nanometric position sensor.

Without surprise, nanomaterials show a unique property on adhesion from van der Waals force, similar as other exceptional properties due to size scaling of the material. Compared to macroscopic and microstructure materials, nano size materials have astonishingly strong adhesion when contacting substrates, the energy of which are several orders of magnitude larger than adhesion energies commonly found in Si micromechanical systems.

Koenig & Bunch demonstrated ultrastrong adhesion between exfoliated graphene membrane and SiO_2 substrates by directly measuring delamination pressures of graphene in blister tests.[56] The adhesion energy for monolayer graphene is 0.45 ± 0.02 J/m^2, and that for multilayer graphene is 0.31 ± 0.03 J/m^2. These values are larger than the adhesion energies measured in typical micro/nano mechanical structures, and are comparable to solid-liquid adhesion energies. They attributed these high adhesion energies to the flexibility of graphene, which allows it to conform to the topography of substrates in a greater degree than traditional microstructure material, thus making its short range van der Waals interaction much stronger. Scharfenberg and Zong measured the graphene adhesion as well by exfoliating a piece of graphene on to substrates with a special topography, namely microsacle - corrugated metallic (Al) substrates and gold nanoparticles on Si substrate.[102] By measuring the conformation of graphene to the features on substrates, they can calculate the adhesion energy between graphene and the substrates. The adhesion energies they measured are about half of the value measured by
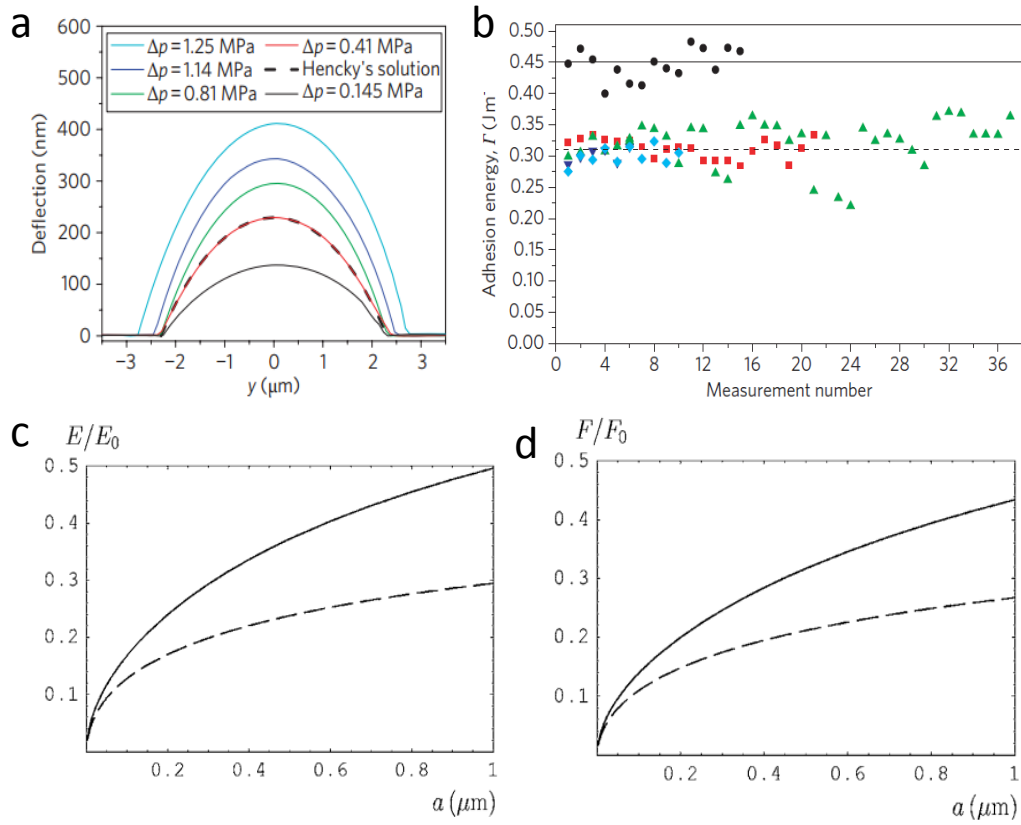
Figure 4.9 a) Deflection versus position for five different values of Δp between 0.145 MPa (black) and 1.25 MPa (cyan). The dashed black line is obtained from Hencky's solution for Δp ~0.41 MPa. The deflection is measured by AFM along a line that passes through the center of the membrane. b) 1-5 layers Graphene/SiO₂ adhesion energies.[56] c) The normalized to the case of ideal metals van der Waals and Casimir energy and force (d) per unit area between a graphene and a semispace versus separation. The solid and dashed lines are related to the semispace made of Au and Si, respectively.[103,104]

Koenig. This difference might come from the use of smaller value of Young's Modulus in their calculation. Gao and Huang studied the effect of surface roughness analytically on adhesion of 1-10 layers of graphene membranes based on Koenig's experiment. For monolayer graphene, the influence of roughness is extremely mild with the corrugation amplitude changing from 0.06 nm to 0.2 nm. However, the adhesion energies can decrease by ~15 % for 2 - 10 layers with the same roughness change.[105]

Like adhesion of graphene at short range, the retarded van der Waals force on graphene is also a hot topic, theoretically. By using the reflection coefficients obtained from the specific boundary conditions for the electromagnetic oscillations on the infinitely thin plasma sheet, Bordag et al. obtained Lifshitz-type formulas calculated the van der Waals and Casimir interaction between a graphene and material plate, between an atom or a molecule and graphene[103,104]. The computational results for the van der Waals and Casimir energy density $E(a)$ normalized to the Casimir energy density in the configuration of the ideal metal plates,

$$E_0(a) = -\frac{\pi^2}{720}\frac{\hbar c}{a^3}$$
(4.8)

are shown in Figure 4.9a as a function of separation. The solid and dashed lines are related to the interaction of graphene with Au and Si, respectively. In Figure 4.9b the analogous results for the van der Waals force per unit area $F(a)$ normalized to the force per unit area,

$$E_0(a) = -\frac{\pi^2}{240}\frac{\hbar c}{a^4}$$
(4.9)

The adhesion energies from other nano-materials were also measured with results of the same order of those of graphene. Yu & Ruoff estimated the adhesion energies between carbon nanotube (CNT) and SiO_2 substrate by calculating the energy balance between the mechanical deformation and surface interactions for a fully collapsed state of multiple-wall carbon nanotubes

(MWCNT).[106] They showed that the work of adhesion should be greater or equal to 0.33 J/m^2 to maintain the collapsed state for the MWCNT. This result is close to the work of adhesion between SiO_2 and graphite calculated by double the square root of the product of surface energies of both materials. Desai and Haque measured the van der Waals force between zinc oxide nanowires and silicon substrate (Si AFM tip) by a snap in measurement in situ inside a scanning electron microscope. Calculated force is 81.05 pN.[107]

4.3 Strain Engineering

Strain engineering was proposed to enhance electronic device performance by modulating the strain in the transport channel in CMOS transistors.[108] The applied strain can improve charge carrier mobility (electron or hole), and thereby conductivity through the channel. This technique has been employed by major processor manufacturers, like Intel, IBM, and AMD.

4.3.1 Strain Engineering in Graphene

Since 2D materials (graphene and MoS_2) are studied and used as field effect transistors (FETs) channels. Researchers started to work on the strain engineering of the 2D materials. Mingyuan Huang from James Hone's group studies Raman scattering of single layer graphene under uniaxial stress, which is applied by 3 point bending of the PDMS substrate where graphene is exfoliated and anchored.[109] The result suggests two types of modification of the low-energy electronic structure of graphene: a deformation of the Dirac cone and its displacement away from the K point. Later, with the transport measurement he also finds that there is no band gap opening with uniaxial strain engineering, which is consistent with results from the first-principles informed molecular dynamics simulation.[110]

4.3.2 Electronic Band Structure in MoS$_2$

Similar strain engineering experiments have been done on single and few layer MoS$_2$. Compared to graphene, MoS$_2$ is a more attractive material for elastic strain engineering because it is a semiconductor.[10,43,46] With measurements of optical absorption, photoluminescence (PL), and photoconductivity, Kin Fai Mak et al. first experimentally studied the band structure of 2D MoS$_2$ (1-6 layers), and measured a 1.9 eV bandgap in monolayer MoS$_2$ after a 0.6 eV upward shift in indirect band gap energy from bulk MoS$_2$ with the decreasing of number of layers.[43] The samples used in this experiment are all free standing over microcavities etched on a Silicon wafer so the doping effect from the supporting substrate can be eliminated. They also found that the luminescence intensity in freestanding monolayer is much higher than supported MoS$_2$ with an increase in luminescence quantum efficiency by a factor of 10^4. Kin Fai Mak et al. studied the band structure of monolayer MoS$_2$ further with a supported and back gated MoS$_2$ monolayer on SiO$_2$/Si substrate. In this way, the doping level of the monolayer MoS$_2$ sample can be controlled by the back gate with a nearly undoped level when applying a -100 V gate voltage. With this experimental setup, they found that in undoped monolayer MoS$_2$ the smallest measured bandgap energy is ~1.92 eV (A peak) with absorption spectra, corresponding to the direct optical transition from highest spin-split valence band and the lowest conduction band.[111] Furthermore, they pointed out that the transition is significantly modified by photogenerated excitons, therefore calling the A peak as the low-energy exciton peak. With the gate voltage on the MoS$_2$ increasing from -100 V to 80 V, the prominent A exciton peak shown in PL diminishes and disappears into the background when $V_g > 0$, while a new A$^-$ peak appears and broadens gradually. The A$^-$ peak is explained with the rise of trions, a kind of quasiparticles composed of two electrons and a hole.

4.3.3 Strain Engineering in MoS$_2$

After the first experimental study of electronic band structure of MoS$_2$, it is proposed in a bunch of theoretical papers,[112–114] that mechanical strains can strongly perturb the band structure in 2D MoS$_2$. This was immediately followed by experimental verifications reported by H. J. Conley et al.[115]. In this work, they exfoliated monolayer and bilayers MoS$_2$ on a layer of cross-linked SU8 photoresist deposited on polycarbonate (PC) beam, and by bending the PC beam with a four points bending apparatus they applied uniaxial strain to the MoS$_2$ flakes. The amounts of uniaxial strain applied are calculated from the bending and verified with Raman spectra. From PL spectra of MoS$_2$ strained to ~2%, they derived a nearly linear band gap redshift rate of ~45 meV/% for A peak in monolayer samples, while in bilayers a A peak redshift rate of ~53 meV/% with a rate of ~120 meV/% for indirect band gap (I peak). Similar experiments are conducted by K. He et al. from Chinese Academy of Science in China and G. Wang et al. from Columbia University by using a cantilever and 3 point bending structure respectively to apply uniaxial strains. They all observed very close A peak tuning rate in monolayer samples as reported by H. J. Conley.[116,117]

In all previous experiments, we can assume the strain over the MoS$_2$ samples is uniform. A. Castellanos-Gomez et al. applied local uniaxial strain up to 2.5 % in 3-4 layers MoS$_2$ by buckling the flake on elastomer.[118] One advantage of this measurement set up is to achieve large amount of data with different strain values at once. The overall tuning rate of direct band gap is close to what others measured, but the fitting and analysis of the data favors a nonlinear tuning rate starting with a large tuning rate at very small strain, which decreases with the increase of strain applied.

Other than uniaxial strains, Y.Y. Hui et al. applied compressive biaxial strain on trilayers MoS$_2$ instead with a piezoelectric substrate.[119] Due to the limit of the piezoelectric substrate, the maximum strain applied is only 0.2 %. They claimed exceptional tunability from the experiment of ~ 300 meV/% redshift rate.

4.4   Conclusion

In this chapter, we review the literatures of the nanomechanical systems in the fields of NEMS switches, measurement of interfacial forces and band gap engineering with elastic strain, which provides a background for the experimental section in the following three chapters.

Chapter 5

Large Arrays and Properties of 3-Terminal Graphene Nanoelectromechanical Switches

5.1 *Introduction*

Nanoelectromechanical (NEMS) switches are promising devices used for mechanical computing, data storage, and RF communication,[8,13,78,80,120–122] due to their attractive attributes such as microwave operating frequencies, low power consumption, high on/off ratio, radiation hardness, and device density comparable to semiconductor integrated circuits.[2,12,71,72,123–125] Graphene, an atomic sheet of graphite, is the thinnest and strongest material in the world.[22,25] Its high Young's modulus (1 TPa), extremely low mass (only 1 layer of atoms), and low resistivity (1 μΩ-cm), makes it an ideal material for a NEMS switch.[7,18,29,58,71–74] Previously reported graphene based NEMS switches are primarily 2-terminal, one-off laboratory scale demonstrations.[71–73,126] These switches operate by deflecting a suspended graphene membrane with a source-drain voltage (V_{sd}) and measuring the current once contact is made. A 3-terminal NEMS switch, on the other hand, using a third electrode to apply an actuation voltage (V_g) independent of the V_{sd}, provides further advantages such as greater operational flexibility, lower power consumption, and higher level of integration and system functionality compared to 2-terminal devices.[127–129] The graphene contact switches reported to date are primarily doubly clamped beams that suffer reliability problems due to tears on open edges and/or irreversible stiction of graphene.[71,72] Here, we fabricate and characterize a large array of circularly clamped

graphene NEMS switches, which can work with either 2-terminal or 3-terminal electromechanical switching. The devices show low actuation voltage and improved mechanical integrity with a novel design, which also reduces the contact area thereby reducing stiction problems.

5.2   Device Design

The design of our graphene NEMS contact switch is different from that of most traditional MEMS/NEMS switches, in which a doubly clamped beam or cantilever makes large area surface contact with an electrode.[13,71,72,80,83,126,127,130] A 3D schematic of the design is shown in Figure 5.1. Our device switches with a "line" contact similar to a recently reported "pipe clip" geometry.[125] A distinct advantage of this geometry is that tear is eliminated and stiction is limited, which addresses two major challenges facing implementation of a reliable graphene NEMS switch. Furthermore, in the design, the graphene membrane with its edge completely clamped provides higher restoring force compared with a doubly clamped beam or cantilever structure of the same dimensions. The mechanical integrity of the graphene nanostructure is also improved without open ends on the graphene membrane for tearing. From more than one hundred devices scanned with non-contact mode AFM before and after switching, no tears in the graphene membrane have been observed. In addition, this design with the graphene membrane making a "line" contact also decreases the contact area, which provides a platform to reduce stiction problems.[56,58,72,125]
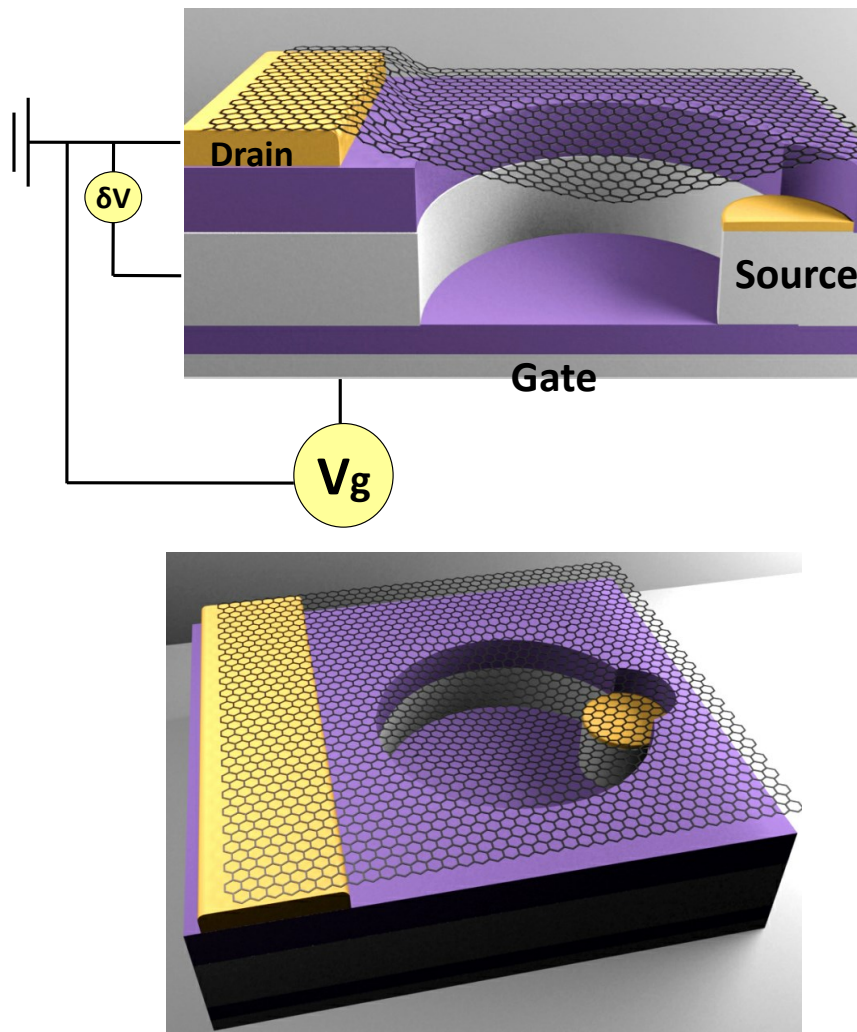
Figure 5.1 Three dimensional schematic of a 3-terminal graphene NEMS switch. (upper) Cross sectional view and top view, (lower).

5.3 Device Fabrication

The graphene NEMS switch array is made by a bottom-up fabrication process.[8] We start with a substrate (typically 2 cm x 1 cm) which includes prefabricated gold electrodes defining source and drain electrodes, a doped silicon layer which acts as a gate electrode, and predefined wells over which suspended graphene is transferred. Each chip which will contain ~1000 devices is separated into individual units (~ 700 µm x 700 µm) by trenches etched through the device silicon layer on which source electrodes are deposited, and each unit is prepared with four drain electrodes that correspond to a single source electrode. Finally, monolayer graphene films are grown by chemical vapor deposition (CVD) on copper, patterned into rectangular strips, and then transferred to the prefabricated substrates using a dry transfer technique.[16,39]

The predefined wells over which graphene is transferred are fabricated by a combination of standard micro-fabrication processes on SOI wafers (device silicon layer 1µm thick, buried oxide layer 100/200 nm thick, handle silicon layer 500µm thick). The fabrication process chart is shown in Figure 5.2. At first, the device layer is etched by reactive ion etching (RIE) with SF_6 down to 270-300 nm, and then the device layer is heavily doped by boron diffusion. Thermal oxidation is used to grow a layer of 150-200 nm thick SiO_x on the device Si layer of an SOI wafer. An array of 220 µm x 220 µm Au electrodes (drain electrodes) are patterned using photolithography followed by thermal evaporation of 5/50 nm of Cr/Au (Figure 5.2b). The wells, over which graphene membranes are suspended, are etched next to the drain electrodes. First, an array of ~ 2 µm circular wells are etched through the top SiO_x layer by reactive ion etching (RIE), and a layer of 5/30 nm Cr/Au is thermally evaporated into the wells to define
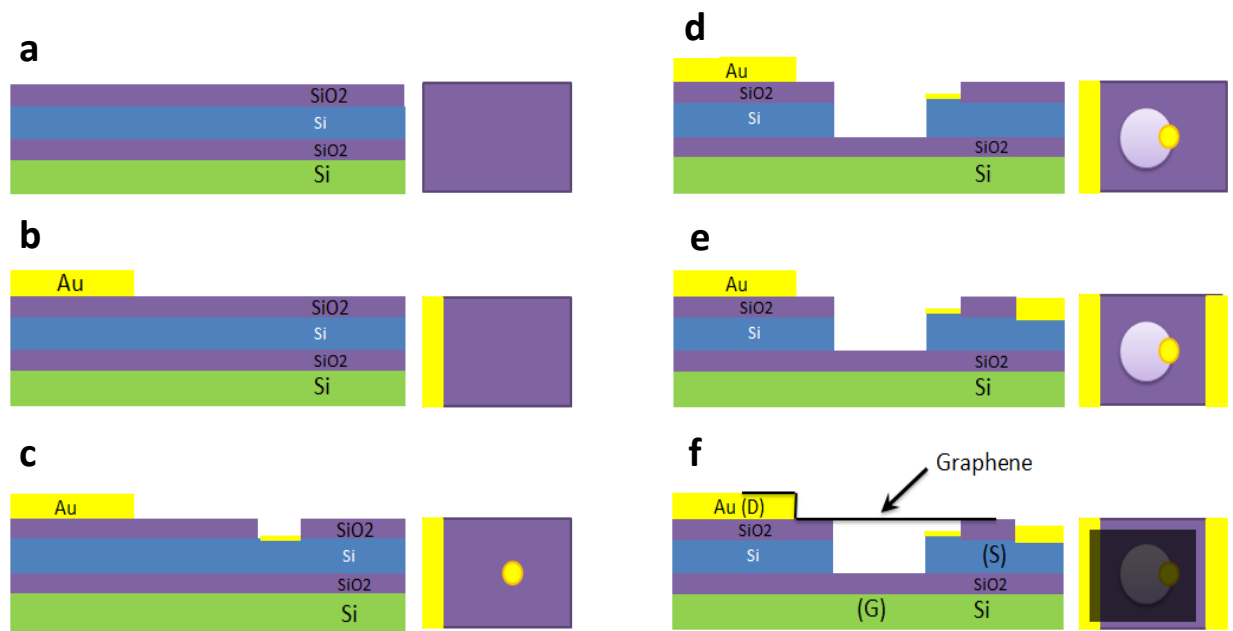
Figure 5.2 Schematic of process flow for fabrication of CVD graphene 3-terminal switches.

the source electrodes (Figure 5.2c). Then, larger circular wells (~5 μm diameter) are etched overlapping each source electrode and through both the SiO_x layer and the Si device layer with a combination of buffered oxide etching (BOE 1:6) and RIE (Figure 5.2d-e). Finally, each chip is separated into arrays of units by trenches (15 μm wide) etched down to the buried oxide layer, and each unit is prepared for four potential devices. In each unit, two windows (200 μm x 80 μm) to the underneath source electrode are fabricated by RIE etching the top oxide layer and depositing a layer of Cr/Au (5/60 nm). Graphene sheets are prepared by chemical vapor deposition (CVD) on copper foil, and then patterned with oxygen plasma into arrays of 50 μm x 12 μm rectangular strips. Graphene sheets were transferred onto the substrates using a dry transfer method.[16,39] (Figure 5.2f)

Figure 5.3a and 5.3b is an optical image of a four unit array of graphene NEMS switches and zoom in of a completed device, respectively. Atomic force microscope (AFM) images of suspended graphene membranes were taken for more than 100 devices with a Veeco Dimension 3100 in non-contact mode (tip: μmasch, mode NSC15, 325 kHz, 46 N/m), and the majority of initial deflections before electrical measurements at room temperature and atmosphere are between 50-100 nm downward. (see Statistical distribution of the initial deflections in Section 5.10). This initial deflection was found to increase after electrical measurements were performed suggesting that further slack is introduced in the graphene, presumably through sliding of the graphene. Figure 5.3b is an example of the AFM image of the switch showing graphene suspended over the etched well and electrically contacting the drain electrode. A side view schematic of the completed device is shown in Figure 5.1. A monolayer graphene film is electrically contacted to a drain electrode and suspended over a gate and source electrode (all of which are electrically isolated from each other.)

64
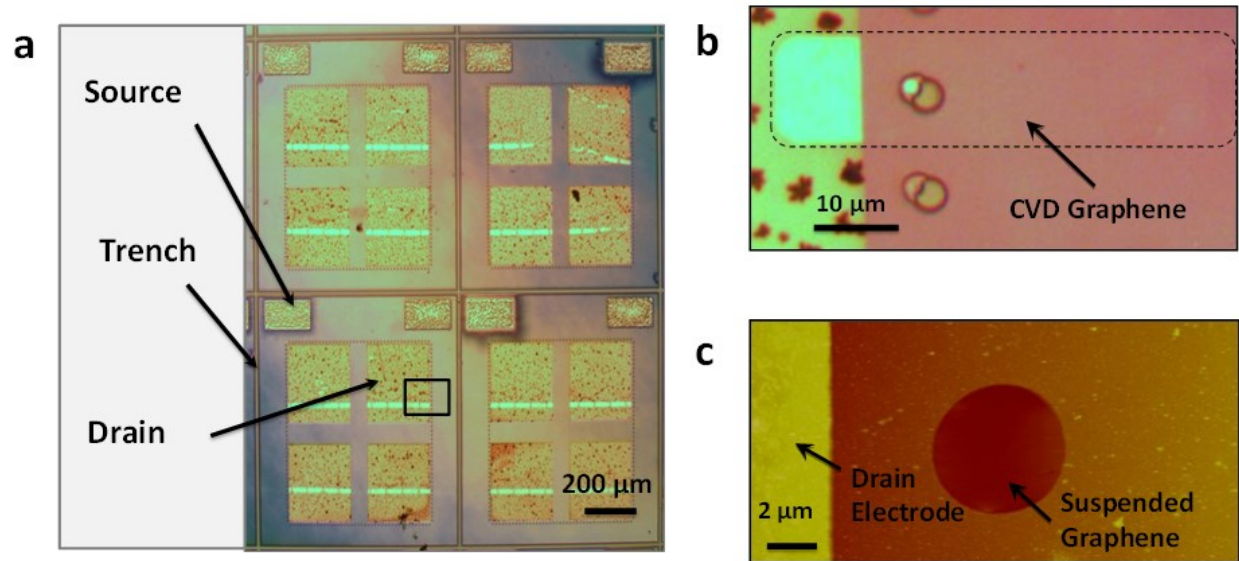
Figure 5.3 a) Optical image of a four unit array of graphene NEMS switches. b) Zoomed in optical image of a single graphene NEMS switch located in the black rectangle in (a). c) Atomic force microscope image of a graphene NEMS switch.

5.4   Electrical Measurement

The completed device can work either as a two-terminal or three-terminal NEMS switch. All the electrical measurements are performed at 78 K and a pressure of ~10^{-6} Torr unless otherwise indicated to eliminate the influence of capillary forces due to adsorbed water on device operation. The low temperature electrical measurements in vacuum are measured in a Desert cryogenic probe station cooled by liquid nitrogen. In 2-terminal operation, a voltage between the source and drain electrodes, V_{sd}, is used to electrostatically deflect the graphene membrane. When the graphene membrane gets sufficiently close to the source electrode it forms a conducting pathway between the source and drain electrode which results in a current, I_{sd} (Figure 5.4a). In 2-terminal operation the gate voltage is kept at $V_g = 0$ V. At a critical voltage of $V_{sd} \sim$ 3.5 V, the current between the source and drain electrodes increases abruptly and the device switches "on"; when V_{sd} is swept back to 0V the current abruptly decreases which leads to the "off" position. The typical number of switching cycles measured is ~ 10-30. Figure 5.4b shows the same device switching up to 30 times. There is some small scatter in the switching voltage but most of the switching takes place between $V_{sd} \sim 3.0$ V– 3.5 V.

In 3-terminal operation, a constant V_{sd} is applied and then the gate voltage is swept until switching commences. Data for a different graphene switch is shown in Figure 5.4c. The device switches at $V_g \sim 30$ V, with $V_{sd} = 4$ V. Figure 5.4d shows the corresponding resistance, R_{sd}, vs V_g for the same device. Initially the "off state" has a high resistance ~ 10 GΩ. As the gate voltage is increased, there is an electrostatic force on the graphene membrane that pulls the graphene closer to the drain electrode. This is supported by the resistance decreasing with V_g, suggesting some tunnelling or leakage current between the graphene and drain electrode. At $V_g \sim 30$ V, the
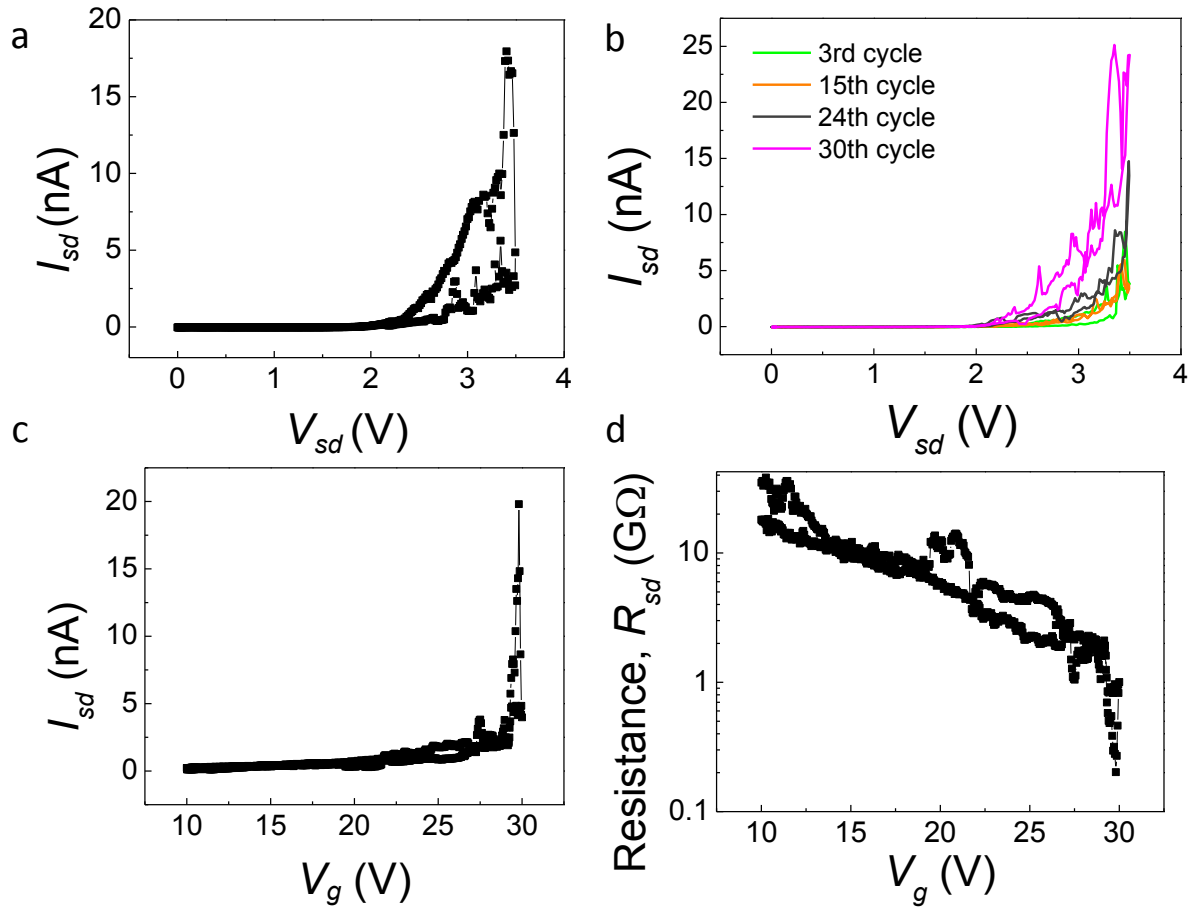
Figure 5.4 a) Current, I_{sd}, vs. source-drain voltage, V_{sd}, for a graphene NEMS switch under two-terminal switching with the gate voltage $V_g = 0$ V. A trace and retrace is shown. b) Current, I_{sd}, vs. source-drain voltage, V_{sd}, for the same graphene NEMS switch in (a) under multiple two-terminal switching with the gate voltage $V_g = 0$ V. A trace and retrace is shown for each cycle. c) Current, I_{sd}, vs. gate voltage, V_g, for a graphene NEMS switch operated as a 3-terminal switch where $V_{sd} = 4$ V. A trace and retrace is shown. d) Resistance, R_{sd}, vs. V_g for the same trace shown in (c).

graphene is sufficiently close to the drain electrode that more intimate contact is made and the R decreases by ~ 1 order of magnitude. Both the 2-terminal and 3-terminal switching I-V curves follow a similar behavior to other previously reported NEMS switches where the current increases gradually at first following a smooth curve, and then increases abruptly.[71,72,80,127] For both the 2-terminal and 3-terminal switches, we define the voltage at the point when the current starts to jump as the "threshold voltage".

5.5 Verification of Electromechanical Switching

To rule out purely electrical effects in the switching behavior, we did some additional experiments to distinguish the IV characteristics from graphene NEMS switches and graphene-Si Schottky barriers, and then to verify that the measured electrical IV characteristics come from the electromechanical actuated movements.

The electrostatic force that deflects the graphene membrane, $F_e = - V^2 A \varepsilon_0 \varepsilon_r / 2d^2$, is symmetric with respect to the sign, where V is the applied voltage, A is the area of the membrane, ε_0 is the dielectric permittivity of vacuum space, ε_r is the dielectric constant, and d is the distance between the graphene membrane and the underneath electrode. Therefore, switching should be symmetric for positive and negative voltages, which is indeed the case. One example is shown in Figure 5.5, with the optical image in Figure 5.5a. For two-terminal switching with positive and negative V_{sd}, the threshold V_{sd} are ~ 6 V and ~ -6 V, respectively (Figure 5.5b). Three terminal switching from the same device demonstrates similar symmetry. When sweeping the gate voltage in the positive range with $V_{sd} = 4$ V, the threshold V_g is ~ 28V (Figure 5.5c). For the opposite case, the threshold V_g is ~ -28 V with $V_{sd} = -4$ V (Figure 5.5d). However, this kind of symmetry is not observed in graphene-Si Schottky barriers.[131,132]
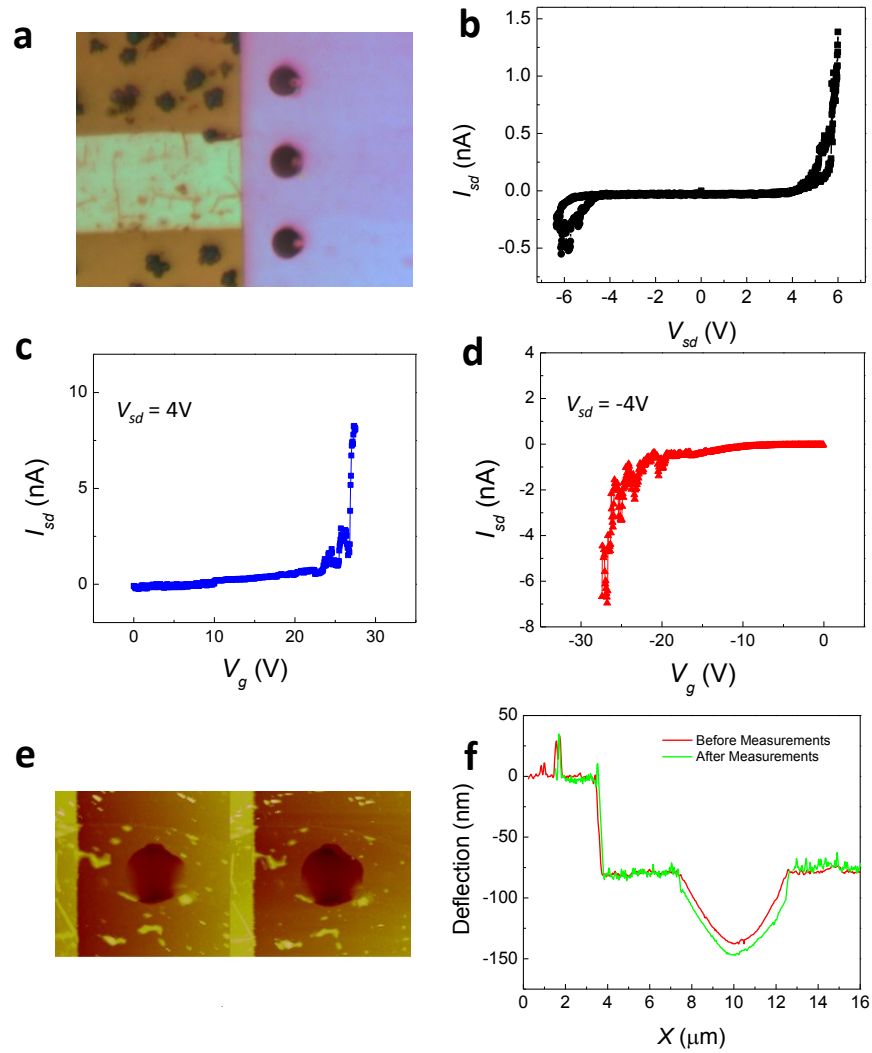
Figure 5.5 a) Optical image of the graphene NEMS switch. b) 2-terminal IV characteristic with positive and negative V_{sd}. c) 3-terminal IV characteristic with positive V_{sd} and V_g. d) 3-terminal IV characteristic with negative V_{sd} and V_g. e) AFM images of the graphene membrane in the device (in the black rectangle) before and after the electrical measurements shown in Figure 5.5 b, c,d. f) Cross cuts of the AFM images before and after electrical measurements across the center of the graphene membrane.

In addition, we checked if the graphene membrane in the device from which we took the data in Figure 5.5b, c, d is suspended with atomic force microscope (AFM) imaging before and after these electrical measurements to rule out the possibility that the graphene membrane got stuck to the electrodes before measurement. The AFM images of the suspended graphene membrane in the device before and after the electrical measurements are shown in Figure 5.5e, and the images are of the same color scale. We observed that the graphene membrane remained free standing before and after the electrical measurements. From the crosscuts of the AFM images in Figure 5.5f, we also found that the graphene membrane dipped in about 10 nm, most likely due to slack introduced in the graphene from the transfer process. This phenomenon can be considered as further evidence of the electromechanical switching in the device.

5.6   Temperature Dependence

We also studied the temperature dependence of the threshold switching voltages in the graphene NEMS switches and compared it with that of "stuck" devices. Figure 5.6a shows the 2-terminal switching IV curves at four different temperatures ranging from 100 K to 225 K. With the increase of temperature, the threshold V_{sd} voltage decreases. The three terminal switching shows a similar dependence (Figure 5.6b). With the temperature increase from 100 K to 175 K, the switching V_g decrease from more than 42 V to ~18 V with V_{sd} = 3V. The apparent temperature dependence can be attributed to an increase in the tension on suspended graphene with decrease of temperature, which has been observed for both CVD and exfoliated suspended graphene membranes.[8, 9] In comparison, the IV_{sd} traces for this device after being "stuck", the schematic of which is shown in Figure 5.6c, for temperatures from 150 K to 300 K showed very limited temperature dependence in contrast to the data in Figure 5.6d.
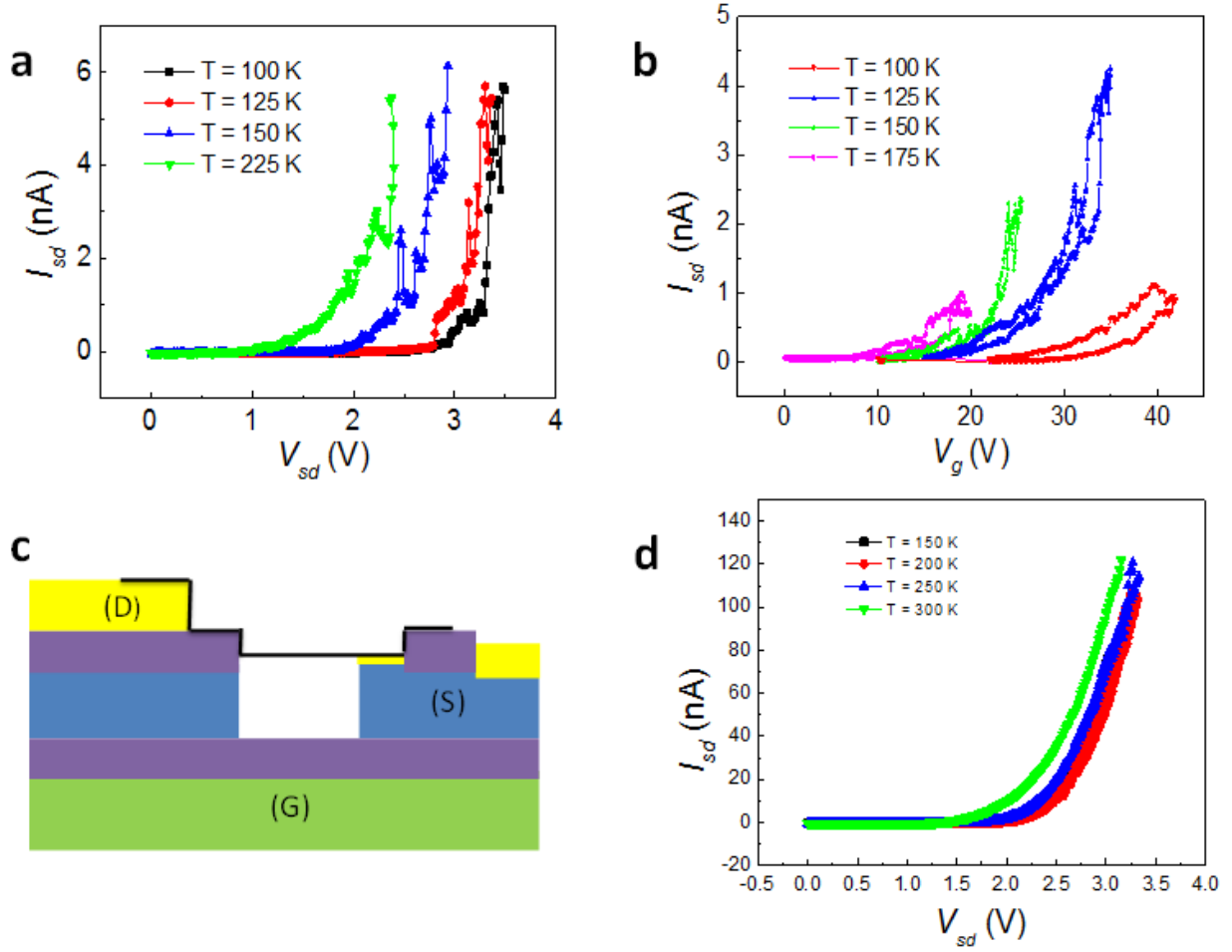
Figure 5.6 Temperature dependence measurement. a) Two-terminal switching at different temperatures from 100 K to 225K. b) Three-terminal switching at different temperatures from 100 K to 175 K. c) Schematic of a switch with graphene stuck to the source electrode. d) IV_{sd} characteristic of the "stuck device".

5.7 Statistics of Threshold Voltage

We measured the threshold V_{sd} in 51 2-terminal devices with the same geometry and dimensions (radius of cavities a = 2.5 μm, radius of source electrodes b = 1 μm) but varied the separation between graphene and source electrodes, d_1 (Figure 5.7a and 5.7b). The average threshold voltage V_{sd} and standard deviation are 5.45 ± 0.85 V for devices with d_1 = 120 nm (Figure 5.7a), and 6.23 ± 0.89 V for d_1 = 160 nm (Figure 5.7b), respectively. This decrease in the average threshold V_{sd} is consistent with the simple electrostatic model where decreasing d_1 leads to a decreasing threshold V_{sd}. The measured threshold V_{sd} is as low as 3.5 V, and all of them are less than 10 V. These low voltages are much smaller than typical MEMS switches (30 - 50 V) and comparable to CMOS logic and conventional dynamic random access memory (RAM) technology.[83,123] We also measured 9 3-terminal graphene switches, and the threshold V_g ranges from 20 V to 45 V, while V_{sd} is set as 3 V (Figure 5.7c).

5.8 Modeling and Analysis

To understand the mechanics of the switches, we numerically model our device using non-linear finite element simulations with the software package Abaqus. We use a decoupled electro-mechanical model that approximates the electrostatic force at a point (x,y) on the deformable electrode to be the same as that between two parallel plates and this approach gives a reasonable approximate solution (Figure 5.8a).[133–135] The electrostatic pressure from the gate electrode P_g and source electrode P_{sd} on the graphene membrane are defined as follows:
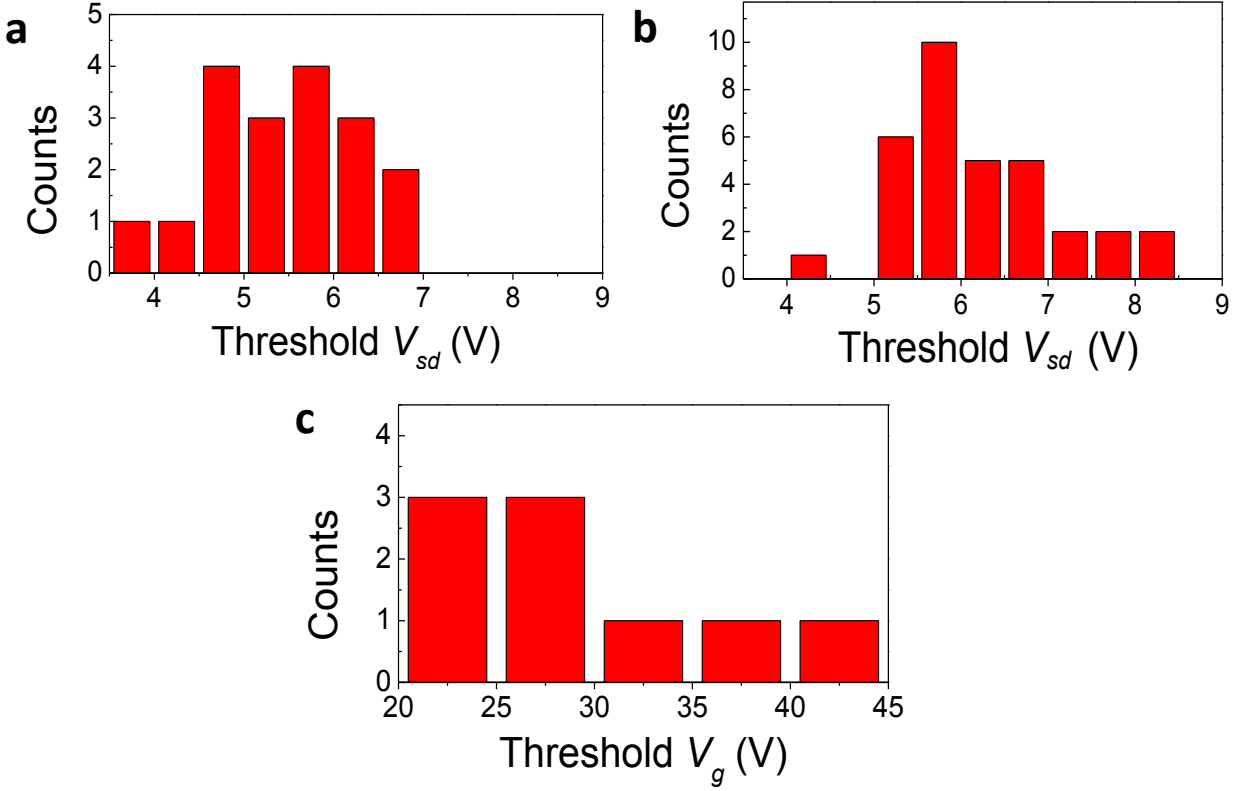
Figure 5.7 a) A histogram showing the number of devices vs. their respective switching voltage for 2-terminal graphene NEMS switches with d_1 = 120 nm. The average and standard deviation threshold V_{sd} = 5.45 ± 0.85 V. b) A histogram showing the number of devices vs. their respective switching voltage for 2-terminal graphene NEMS switches with d_1 = 160 nm. The average and standard deviation threshold V_{sd} = 6.23 ± 0.89 V. c)A histogram showing the number of devices vs. their respective switching voltage for 3-terminal graphene NEMS switches with d_1 = 120 nm and V_{sd} = 3 V.

$$P_g = \frac{\epsilon_0 V_g^2}{2(d_1 + d_2 + d_3/k - w(x,y))^2}$$

(5.1)

$$P_{sd} = \frac{\epsilon_0 V_{sd}^2}{2(d_1 - w(x,y))^2}$$

(5.2)

here, d_2 , d_3 are the initial separations between source and box oxide layer, and the thickness of the box oxide layer, ε_0 is the dielectric permittivity of vacuum space, κ (= *3.9*) is dielectric constant of silicon dioxide,[136] while *w(x,y)* gives the deflection of the graphene membrane as function of the *x* and *y* coordinates. The electrostatic pressure P_g and P_{sd} act on regions of the graphene directly above the gate and drain electrodes respectively.

The schematic of the switch is as shown in Figure 5.8b. The switch can operate either in 2-terminal or 3-terminal configurations, the difference being that in the 2-terminal operation V_g is set to zero. The simplified finite element (FE) model is also shown in Figure 5.8c. The suspended graphene membrane (drain) is the deformable electrode while the source and gate are rigid and fixed. Hence only the deformable part of the graphene membrane is actually part of the FE model while the rest of the switch is modeled through constraints and loads. The graphene membrane is fixed along the edges and advantage is taken of the two fold symmetry by applying a symmetry boundary condition. The electrostatic forces due to the electric fields between the drain and source electrodes as well as the drain and gate electrodes that deform the graphene membrane are described by equations (1) and (2) in the main text. These position dependent loads have been applied using DLOAD sub-routine of Abaqus.[3] The graphene membrane is modeled with S4R (4 noded shell elements with reduced integration) elements to include both bending and stretching effects.[137,138]
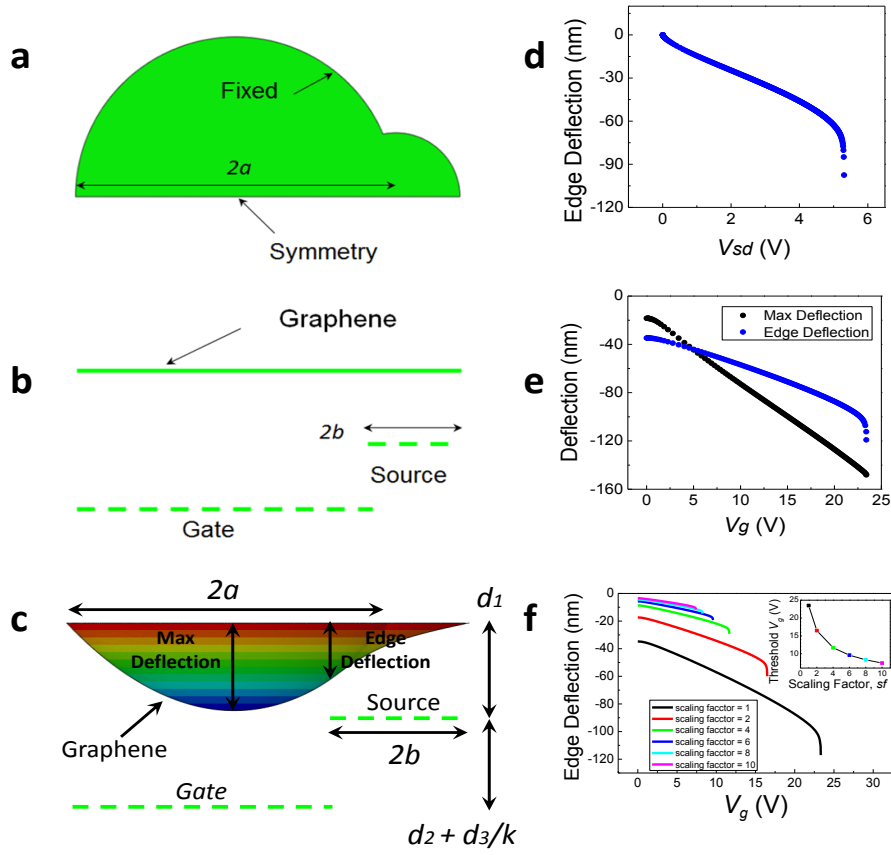
Figure 5.8 a) Top view of a simplified finite element model (Abaqus) of graphene membrane in the NEMS switch. b) Side view of the finite element model. $2a = 5$ μm, $2b = 2$ μm, $d_1 = 120$ nm, $d_2 = 230$ nm, and $d_3 = 200$ nm. c) Simulation of the graphene NEMS switch. d) Simulation results showing the edge deflection vs. V_{sd} of graphene switches ($a = 2.5$ μm, $b = 1$ μm, $d_1 = 120$ nm, $d_2 = 230$ nm, $d_3 = 200$ nm), assuming effective Young's modulus $E_{eff} = 0.4$ TPa, Poisson's ratio $v = 0.16$ and thickness $t = 0.34$ nm. e)Simulation results showing the pull-in of three terminal graphene switches with the same geometry dimension as (d) assuming effective Young's modulus $E_{eff} = 0.4$ TPa, Poisson's ratio $v = 0.16$ and thickness $t = 0.34$ nm. $V_{sd} = 3$ V. f) Simulation results showing plot of edge deflection vs. V_g with scaling factor = 1-10. Inset is the plot of threshold V_{sd} vs. scaling factor, sf.

As the electrostatic load is increased, the membrane deforms and comes closer to the electrodes and at the threshold voltage, pulls-in, thereby making contact and completing the circuit. This contact occurs along the axis of symmetry at the edge of the post (source electrode). We call the deflection of the membrane at this point the "edge deflection". In the two-terminal operation, the pull-in is caused solely by V_{sd} while in the three-terminal operation it is caused by increasing V_g. The results show that the pull-in in the three-terminal case is a local phenomenon as the maximum deflection that occurs near the center of the suspended region along the axis of symmetry shows no abrupt change with increasing V_g.

An example of the simulation results for 2-terminal and 3-terminal configurations are shown in Figure 5.8d and 5.8e respectively assuming the effective Young's modulus of CVD graphene E_{eff} = 0.4 TPa, which is about 40% of the Young's modulus of exfoliated monolayer graphene but is reasonably close to a recently reported value for CVD graphene.[139] The geometrical dimensions are: a = 2.5 μm, b = 1 μm, d_1 = 120 nm, d_2 = 230 nm and d_3 = 200 nm. In the finite element simulations of 2-terminal switching, V_{sd} is varied continuously until the membrane is pulled-in,[69,140] which is shown by an abrupt drop in the deflection of graphene membrane above the edge of source electrode as defined in Figure 5.8c. For the simulation of 3-terminal operation of devices with the same dimensions, V_{sd} is fixed at 3 V and V_g is varied until the graphene membrane is pulled into contact with the source electrode. The threshold V_{sd} and V_g obtained from the simulations are 5.3 V and 23.4 V, respectively. Using the finite element simulations, we took E_{eff} to be a fitting parameter and derived a distribution of E_{eff} from the data shown in Figure 5.7. To fit the data in Figure 5.7a and 5.7c, an average value of E_{eff} = 0.4 TPa is required, while an average of E_{eff} = 0.15 TPa for the data in Figure 5.7b. We think the scatter and deviation in the data of threshold voltages are caused by wrinkles or slack, both initial slack

76

in the transferred graphene and slack introduced through sliding caused by the electrostatic actuation; furthermore, the range of E_{eff} is in line with reported values from CVD graphene.[139] Further detailed studies of the deformation mechanisms would be needed to conclusively resolve these uncertainties, but the overall behaviour appears to be adequately described by the model with the modulus adjusted to account for various potential softening mechanisms.[139]

5.9   Size Scaling

The threshold voltages for our 3-terminal switches range from 20 V to 45 V. However, we find that the value decreases by further scaling down the dimension of the devices in a study of scaling effects with finite element simulations similar to previous ones. We scaled down all the dimensions (initial dimensions: $a = 2.5$ μm, $b = 1$ μm, $d_1 = 120$ nm, $d_2 = 230$ nm, $d_3 = 200$ nm) by the same scaling factor (*sf*) and did the simulations in the 3-terminal configuration. The results of these simulations, where the deformations scaled exactly with the inverse of the scaling factor, are shown through gate voltage (V_g) versus edge deflection plots in Figure 5d. The simulated threshold V_g decreased with *sf* increasing from 1 to 10. When the device is scaled down by 10 times (final dimensions with *sf* = 10: $a = 250$ nm, $b = 100$ nm, $d_1 = 12$ nm, $d_2 = 23$ nm, $d_3 = 20$ nm), the threshold V_g is found to be decreased to 7.4 V from 23.5 V with $V_{sd} = 3$ V, shown in the inset of Figure 5.8f. This indicates that we can potentially have larger device densities with lower actuation voltages and improved efficiencies just by scaling down the devices.

77
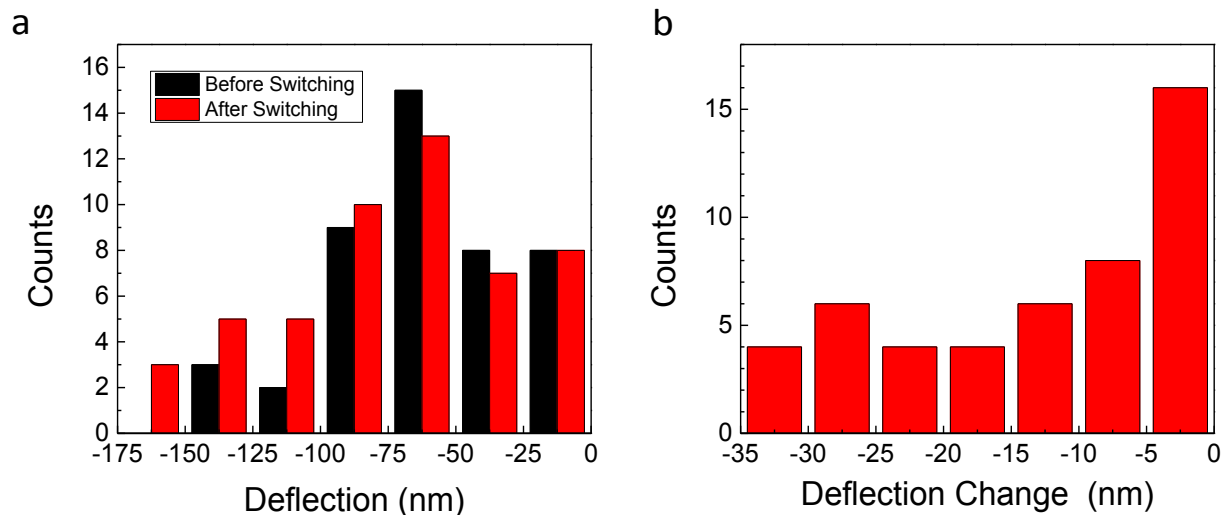
Figure 5.9 a) Statistical distribution of center deflections measured by AFM of graphene membranes from one chip before and after ~10 times electrical switching. b) Statistical distribution of the change of center deflection after the electrical measurements.

5.10 Sliding during Switching

We took AFM images before and after the electrical measurements of more than 100 suspended graphene membrane devices. The statistical distribution of the center deflections of the graphene membranes from 49 devices on one chip before and after 1-10 times of electromechanical switching is shown in Figure 5.9a. The majority of the center deflections before and after electrical measurements are 50-100 nm downward, while the depth of the underneath source electrodes is ~200 nm. After electromechanical switching, most of the graphene membranes have a larger initial deflection, and the deflection changes are plotted in Figure 5.9b. These changes range from 0 nm to 35 nm with the majority being within 10 nm.

5.11 Graphene 3-Terminal Switches with a Different Geometry

We developed a different geometry for the graphene NEMS switches. The side view schematic and top view of the switch is shown in Figure 5.10a. Instead of a Au coated circular source electrode at the edge of the predefined well on which graphene membrane is suspended, a uniform step around the edge of the well is etched with BOE 1:6 and the exposed heavily doped device Si layer is exposed as the source electrode.   The width of the step is $0.3 - 1$ μm, and the depth of the step (d_l) above the source electrodes ranges from 100 nm to 220 nm as well. An example of switching IV characteristics of a graphene NEMS switch is shown in Figure 5.10b and 5.10c. The threshold V_{sd} and V_g are 7 V and 34.5 V, respectively. Figure 5.10d shows a switching IV curve for a three-terminal switch at room temperature. The threshold V_g is ~12V with $V_{sd} = 2.8$ V, close to the requirement for CMOS IC integration.[83]
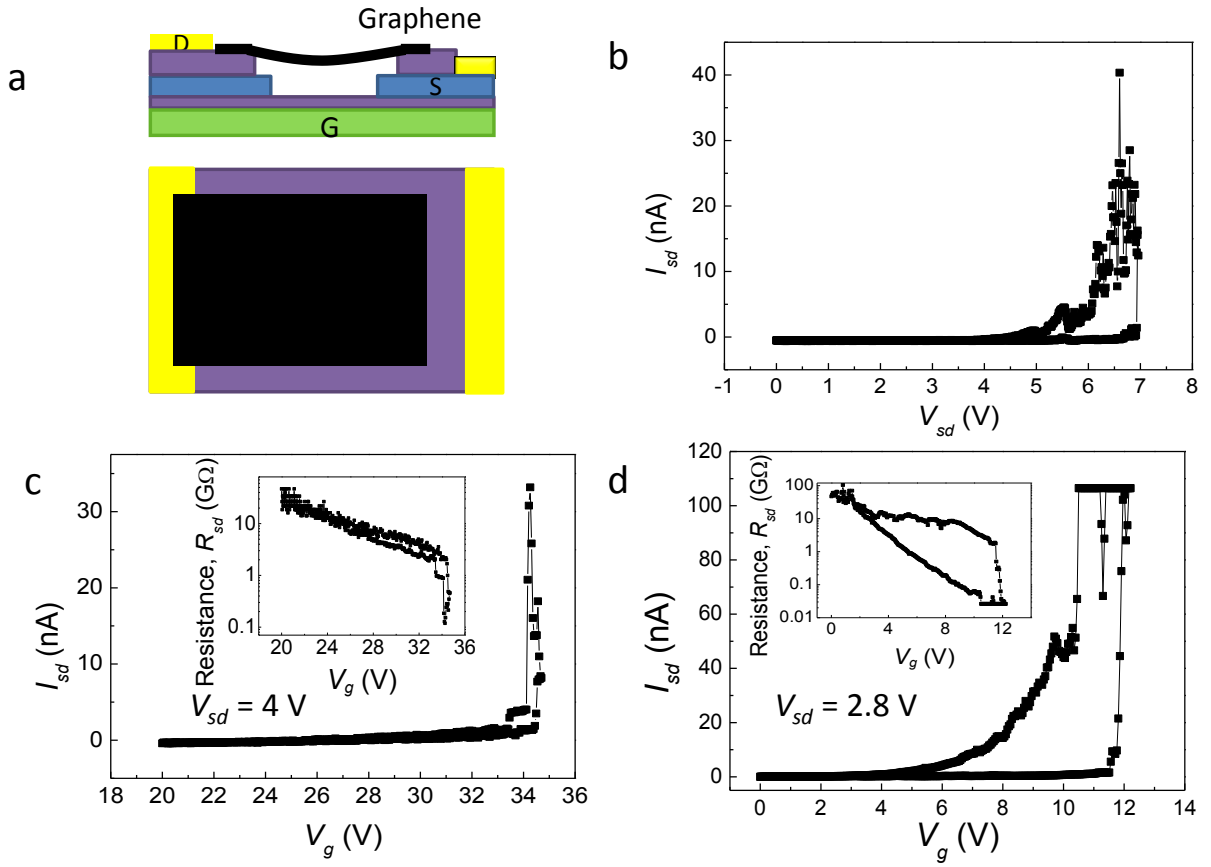
Figure 5.10 Experimental data of a graphene NEMS switch with a different geometry. a) (upper) Side-view schematic of the switch. (lower) Top-view of the switch. b) Two-terminal IV characteristic of a graphene NEMS switch with the geometry in Figure 5.10a. c) Three-terminal IV characteristic of the switch at 78 K and a pressure of ~10^{-6} Torr. d) Three-terminal IV characteristic of a switch with geometry in (a) at room temperature and atmospheric pressure.

5.12 Conclusion

In conclusion, we fabricated and characterized a large array of graphene NEMS switches with a unique design, with which sub – 5 V actuation and an improved mechanical integrity of the graphene membrane is achieved. This design, with the graphene membrane having a "line" contact during switching, holds the promise to address the adhesion challenges in graphene nanomechanical switches. We also study the effect of scaling to the decrease of actuation voltage with simulation, thereby providing an instructive guide for further scaling of graphene NEMS switches.

Chapter 6

Measurement of Interfacial Forces in

Graphene Membranes

6.1   Introduction

Interfacial forces act between all materials.[64] At macroscopic distances, these interfacial forces are weak and practically insignificant, but at distances approaching tens of nanometers, they become much stronger, thereby enhancing the attraction within micro/nanomechanical structures or molecules, and potentially significantly affecting the device performance.[88,95,96,141] Graphene, a 2 dimensional nanomaterial composed of carbon atoms, is a promising material with potential applications in a variety of nanomechanical, biological and electrical devices due to its exceptional properties.[7,18,22,25,32,141–143] Furthermore, graphene being extremely thin with a very high surface area to volume ratio is highly susceptible to interfacial forces and is an ideal candidate to study and characterize these forces.[103,144] Therefore, there is an increasing interest in studying the nature of interfacial forces on graphene.[58] Even though the adhesion strength between graphene and substrates when in contact has been experimentally measured in different ways, experimental measurements of non-contact attractive interfacial forces remains relatively unexplored.[56,57,102,145] Interfacial forces on bulk materials or other nanomaterials have been measured using a variety of configurations.[64,88,141,146] Here, we demonstrate a novel experimental method to study these elusive forces on graphene with a real time observation of the induced pull in instability.

6.2 Fabrication

Devices used in this study consist of a graphene flake suspended over an annular ring etched into a silicon oxide wafer, forming a graphene-sealed microcavity (Figure 6.1a). Device configurations include graphene suspended on bare SiO_x or gold-coated SiO_x. Suspended graphene membranes were fabricated by a combination of standard photolithography, reactive ion etching and mechanical exfoliation of graphene. An array of annular cavities with designed dimensions was first defined by photolithography on an oxidized silicon wafer with a silicon oxide thickness of 90/285 nm. Reactive ion etching was then used to etch the annular rings into microcavities with a depth of 100-120 nm. After removal of photoresist with acetone and isopropanol, the chips were further cleaned in a Nanostrip bath at 60°C for 20 minutes. Thermal evaporation is used to deposit a layer of Cr/Au 5/10 nm for the Au coated annular rings. During the evaporation process, the chips are tilted at a 10~15° angle, so that the Cr/Au atoms can be deposited into the annular rings and cover the side walls. The large aspect ratio between the width and depth of the annular ring allows for a conformal metal deposition such that the post and the substrate are electrically contacted and grounded. Mechanical exfoliation of natural graphite using Scotch tape was then used to deposit suspended graphene sheets over the microcavities.

6.3 Observation of Pull-in Instability

The graphene membranes are pressurized using a previously-developed technique.[32,56] The suspended graphene membranes are placed in a high pressure chamber at a charging pressure, $p_{ext} \sim 300$ kPa of H_2 gas, and left for a sufficiently long time (~10 hours) until the

pressures inside, p_{int}, and outside of the microcavity, p_{ext}, equilibrate. After removing the sample from the high pressure chamber and bringing it to atmospheric pressure, a pressure difference, $\Delta p = p_{int} - p_{ext}$, exists across the graphene membrane. At low Δp, the graphene sheet remains adhered to the inner post and deforms in a donut shape (Figure 6.1b). At sufficiently high Δp, the force is large enough to overcome the adhesion energy of the graphene to the inner post, and the graphene membrane delaminates from it, becoming a spherical cap (Figure 6.1c).

After creating deformed spherical caps, our strategy is to then let gas slowly diffuse out of the microcavity through the underlying SiO_x substrate which decreases Δp and the corresponding central deflection, h, of the graphene membrane until it is pulled back onto the center post due to attractive interactions between the post and graphene membrane. This process is monitored in real-time using an atomic force microscope, AFM (Figure 6.1d). Figure 6.1d shows a series of AFM line scans through the center of a pressurized graphene membrane before and after the pull-in process. Initially a line trace through the center of the membrane (dark blue) corresponds to the situation in Figure 6.1c where the graphene is delaminated from the inner post. At a later time (black) the graphene is pulled onto the post and the graphene is deformed in a donut shape as seen in Figure 6.1b. The red line corresponds to a line trace just before pull-in. We call the center deflection at this point in time, the pull-in distance, h_0. Figure 6.1e shows the measured pull-in distance, h_0, vs. number of graphene layers for graphene sheets in an identical geometry on the same chip (see Appendix A1). The number of graphene sheets was verified by Raman spectroscopy (see Appendix A1). The pull-in distance measured on bare SiO_x substrate, h_0, increases slightly with the number of layers from an average value of $h_0 = 9.2$ nm for 1 layer graphene to $h_0 = 10.8$ nm for 5 layer graphene. At these values of h_0, the variation in the height of the graphene over the post is small and the post and graphene are effectively 2 parallel plates.
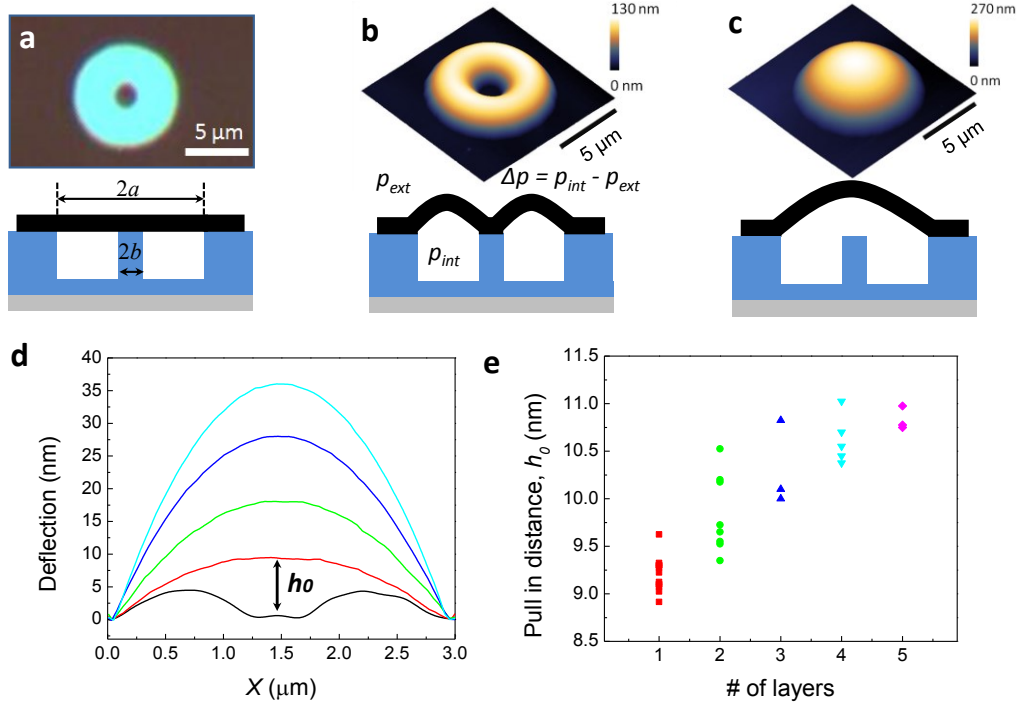
Figure 6.1 a) (upper) Optical image of suspended a few layer graphene membrane in an annular ring geometry. (lower) Side view schematic of the suspended graphene on the annular ring. b) (upper) A 3d rendering of an AFM image of a pressurized graphene membrane in the annular ring geometry before delamination from the inner post. (lower) Side view schematic of the pressurized suspended graphene on the annular ring. c) (upper) A 3d rendering of an AFM image of a pressurized graphene membrane in the annular ring geometry after delamination from the inner post. (lower) Side view schematic of the pressurized suspended graphene delaminated from the inner post. d) A series of AFM line cuts through the center of a pressurized graphene membrane during pull in. The outer diameter, $2a = 3$ µm, and inner diameter, $2b = 0.5$ µm. e) Pull in distance, h_0, vs. number of layers for graphene membranes in an annular ring geometry with $2a = 3$ µm and $2b = 0.5$ µm. (upper left inset) Side view schematic of the graphene membrane right before and after pull in.

6.4   *Analytical Model*

The pull-in behavior observed here is similar to the pull-in or jump-in of a cantilever spring into contact due to interfacial forces.[88,92] We model the pull-in behavior in a continuum setup by considering an isotropic pressurized graphene membrane with initial surface tension, S_0, and an attractive pressure, P_{att}, due to the interfacial force between the post and the graphene membrane.[29,56,147–149] The key assumptions of our treatment include: (1) The membrane tension S is uniform. (2) The pressure due to the surface forces acting between the post and the membrane, P_{att}, is uniform. This is reasonable if the membrane curvature is small. This is the case when the post is small compared to the overall size of the cavity.

The analysis (in Appendix A2) culminates in a relationship between the system parameters given by:

$$\frac{Et}{32\,a^2(1-v)}\left((\Delta p - P_{att})^2 b^4 + \Delta p^2(a^4 - b^4) + P_{att}^2 b^4 log\left(\frac{a^4}{b^4}\right) - 4\,\Delta p\,P_{att}b^2(a^2 - b^2)\right)$$

$$+\left(S_0\left(\frac{1}{4h}\left(\Delta p\,a^2 - P_{att}b^2\left(1 + log\left(\frac{a^2}{b^2}\right)\right)\right)\right)^2\right)$$

$$=\left(\frac{1}{4h}\left(\Delta p\,a^2 - P_{att}b^2\left(1 + log\left(\frac{a^2}{b^2}\right)\right)\right)\right)^3 \tag{6.1}$$

where E is the elastic modulus of graphene, t is the thickness, v is the Poisson ratio, and a and b are the outer and inner radii of the annular cavity, respectively. Equation (1) establishes a relationship between h and Δp if S_0, Et, a, b, and P_{att} are known. The radii, a and b, are measured by AFM, while Et and v are taken from well-established values in the literature for single and few layer graphene.[29,32,56] We cannot directly measure S_0 so we assume values in the range of S_0 = 0.03 - 0.15 N/m with an average value of S_0 = 0.07 N/m, consistent with numerous

86

experimental measurements for exfoliated suspended graphene membranes in a similar geometry.[32,150,151] Figure 6.2a shows the relationship between h vs. Δp obtained from equation (1) using the system parameters for a monolayer graphene membrane: $a = 1.5$ μm, $b = 0.25$ μm, $S_0 = 0.07$ N/m, $Et = 340$ N-m, $v = 0.16$, and $P_{att} = \beta/h^4 = 0.0199$ nN-nm^2/h^4. The deflection, h decreases with decreasing Δp (leaking gas) until a critical point is reached. At this critical maximum deflection, h_0, the graphene is sufficiently close to the post and pulled into the post by the attractive force. This pull-in instability is illustrated by the point on the curve where the slope goes to infinity at the pull in distance h_0, or:

$$\left. \frac{d\Delta p}{dh} \right|_{h=h_0} = 0 \tag{6.2}$$

The measured h_0, a, and b, coupled with the values of S_0, Et, and v taken from the literature, allow us to determine P_{att} by solving eqs. (1) and (2) simultaneously for Δp and P_{att}.

6.5   Finite Element Analysis

To validate the analytical model, we also carried out high-fidelity finite element simulations of the experimental configuration using the code Abaqus where we remove the assumptions used to develop the analytical model. The model used in the simulations is shown in Figure 6.2. Axisymmetric shell elements (that permit both bending and membrane behavior) were used and the Young's modulus and Poisson's ratio were set to 1 TPa[29] and 0.16[152] respectively. The outer edge of the membrane is pinned and the substrate/post is modelled as a fixed analytical rigid body. Since it is known that pressurized graphene behaves like a membrane and bending plays a negligible role in its mechanics[56,145], the value of the bending modulus and
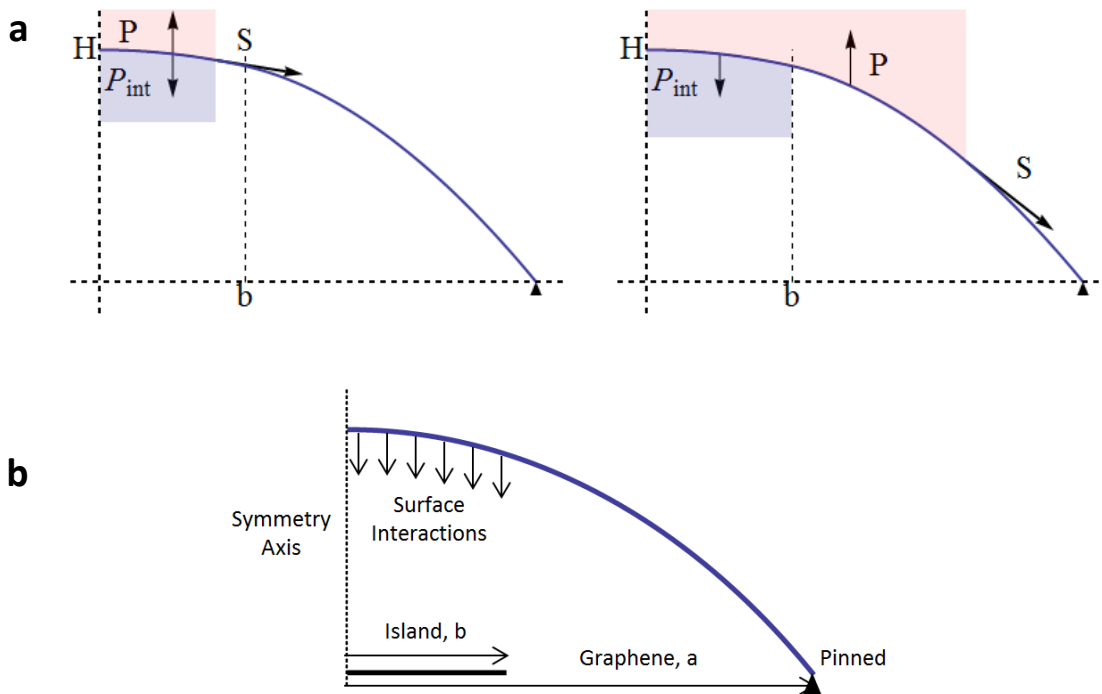
Figure 6.2 Schematic of the model. a) Schematics showing the equilibrium condition for the two regions of the membrane. b) Schematic of the model used for finite element analysis simulations.

slope near the boundary is found to be irrelevant in these simulations. A prescribed initial tension is applied and the attractive interactions between the substrate and the membrane are modelled as surface-to-surface contact/adhesive interactions with the substrate being the master surface. The contact interaction properties are supplied through the user subroutine "UINTER" of Abaqus. The slave nodes experience a tensile (attractive) contact stress (σ_z) only in the vertical direction given by,

$$\sigma_z(r) = -\frac{\beta}{w(r)^4} \tag{6.3}$$

Here, β is a parameter and w is the deflection of the node measured from the substrate. Both σ_z and w are functions of the radial position, in contrast to the analytical model where they are assumed to be independent of position.

The simulation is split into two steps – both static steps with nonlinear geometric effects included. In the step 1, the contact/adhesive interactions are suppressed and the membrane is allowed to deform under the influence of a uniform pressure load acting on the entire area of the suspended membrane. The magnitude of this load is set such that the deflection is just high enough to neglect the interaction pressure if the interactions were not suppressed. This simulates the state of affairs at the beginning of the experiment before the gas begins to leak from the cavity. In the second step, which is a Static-Riks step, a second uniform pressure load is added with the same magnitude as the previous pressure load but in the opposite direction and the surface interactions between the substrate and the membrane are switched on. Hence at a given increment during the step, apart from the force due to the contact interactions, the membrane has the uniform pressure load from the previous step and a uniform pressure in the opposite direction whose value is given by the load proportionality factor. The superposition of these two uniform
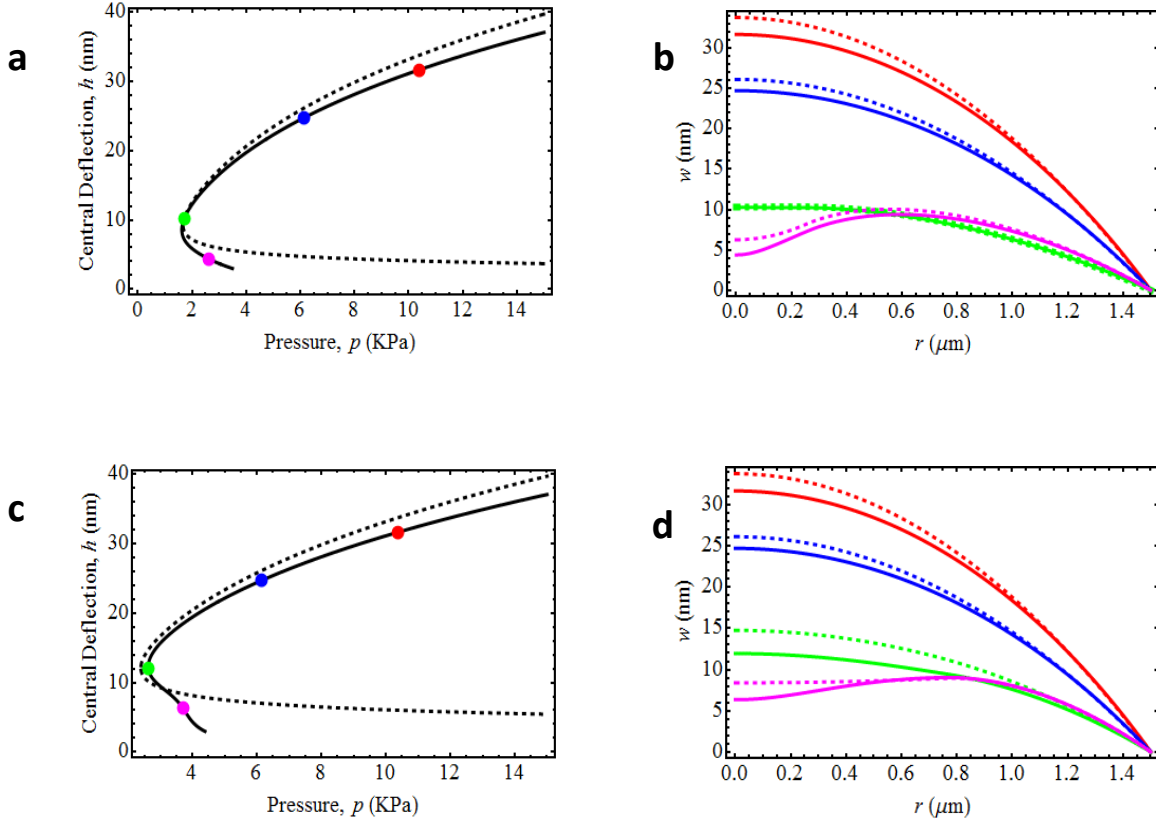
Figure 6.3 a) Plots comparing p vs h behavior as obtained from the FE simulations (solid curve) and the analytical calculations (dashed curve) with $a = 1.5$ µm, $b = 0.25$ µm, $Et = 340$ N/m, $\nu = 0.16$, $S_0 = 0.07$ N/m and $\beta = 0.02$ nN-nm^2. b) The deflection profiles at different pressures (solid – FE, dashed – Analytical) (Red – 10.38 kPa, Blue – 6.12 kPa, Green – 1.72 kPa and Magenta – 2.61 kPa). For convenience, the corresponding points on p vs h plot are also shown. (c) and (d) The same as (a) and (b) except $b = 0.75$ µm. The different pressures used in this case are: Red – 10.39 kPa, Blue – 6.14 kPa, Green – 2.63 kPa and Magenta – 3.70 kPa.

pressure loads mimics the leaking of the gas in the experiment. As the simulation progresses, the load across the membrane decreases and it comes closer to the substrate. This increases the interaction between the post and membrane. The results of this step are plotted in Figure 6.2a of the main text. It can be seen that the load across the membrane initially decreases until a limit point is reached and then it starts increasing. The limit point gives the pull-in distance and the pressure at which it occurs. The configurations below the limit point can't be achieved in a load controlled experiment, but suggest that system has two possible equilibrium configurations at a given pressure load greater than the pull-in pressure. Careful comparison of the analytical and finite element simulation results (Figure 6.3) shows that the analytical result is an accurate description of the physical phenomena as long as the substrate/post size is small compared to the size of the suspended membrane.

A comparison to a high-fidelity finite element model that more accurately treats the spatial dependence of the attractive forces is shown in blue on Figure 6.4a; the close agreement between them supports the validity of our analytical model.

6.6 Layer Dependence

We assumed an attractive force law of the form $P_{att} = \beta/h^4$, consistent with the van der Waals (vdW) force derived from Lifshitz theory between graphene and SiO_2 for separations on the order of 10 nm or the phenomenological Lennard-Jones pair potential of interaction. [64,65,90,153,154]From the experimentally measured pull-in distances in Figure 6.1e we calculate β for each device and arrive at the corresponding $P_{att}(h = h_0)$. This is shown in Figure 6.4b where $\beta = 0.0199$ nN-nm^2 for monolayer graphene. This value is ~1.5% of the dispersion force between 2 perfectly metallic parallel plates, $P_{att} = \pi\hbar c/240h^4 = 1.3$ nN-nm^2/h^4,[90] and agrees reasonably
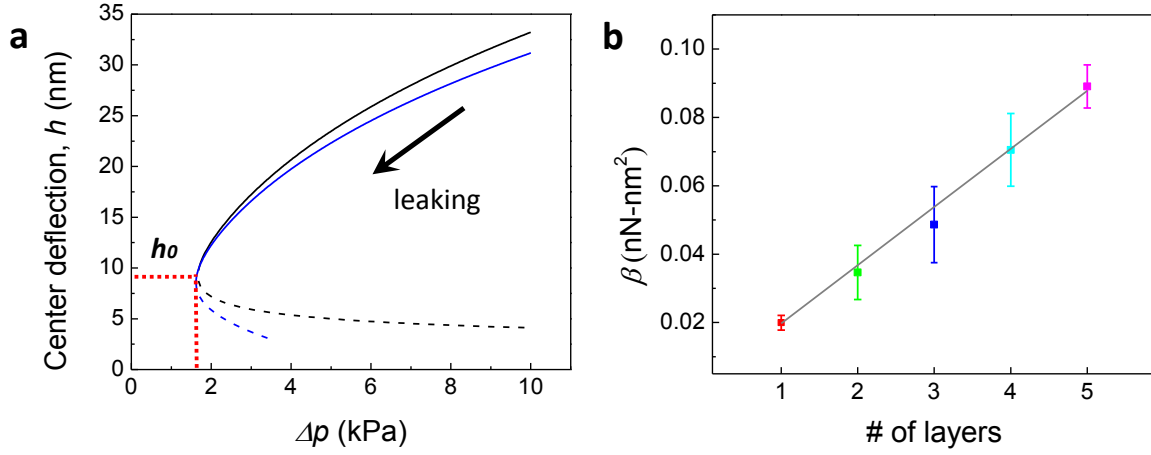
Figure 6.4 Scaling of β with Number of Layers. a) Center deflection, h, vs. pressure difference, Δp, calculated for a monolayer graphene membrane in the annular ring geometry with an outer diameter, $2a = 3$ μm, and inner diameter, $2b = 0.5$ μm. The red dashed line at $\Delta p = 1.68$ kPa corresponds to pull-in and the deflection at this point is $h_0 = 9.2$ nm. The black line corresponds to the analytical model and the blue line is a finite element analysis model. b) The calculated values of β vs. number of layers using the data in (a) assuming a model where the force responsible for pull-in has the form $P_{att} = \beta/h^4$. The initial tension S_0 is assumed to be 0.07 N/m. A best fit line through the data is also shown which has a slope of 0.017 nN-nm^2/# of layer.

well with recent theoretical calculations for graphene and SiO_2 at 10 nm separations, $\beta = 0.001$ nN-nm^2 - 0.01 nN-nm^2 for an intrinsic graphene doping density of 10^{14} m^{-2} and 10^{16} m^{-2} at T = 300 K, respectively.[153] Figure 2b also shows that β increases linearly with # of layers, up to 5 layers, with a slope of 0.017 nN-nm^2/layer, close to the measured value of monolayer graphene, $\beta = 0.0199$ nN-nm^2. This increase with layer number suggests that the strength of the force is increasing in an integer manner as additional graphene layers are added. This is consistent with the additive nature of the vdW force.[64,153] Our results are interesting in the context of recent experiments where an AFM tip was pulled off of a graphene substrate where the pull-off force was observed to depend on the number of graphene layers in suspended membranes,[155] but not on graphene supported by a substrate.[155,156] Despite this similarity in response, we note that pull-off experiments are well-known to be different mechanistically than the pull-in experiments of our study.

6.7 Power Law Study

In addition to vdW force, the interfacial forces can be from capillary or electrostatic forces. The capillary forces take effect when graphene membranes or the substrate are covered with liquid films and the liquid films touch, and the force can be described by $P_{att} \propto 1/h$.[64,154,157] However, we assume that the capillary force is not a likely candidate for the interfacial forces causing the pull-in phenomenon because absorbed liquid films of 10 nm thickness are unlikely to form between graphene membranes and the substrate.[158,159] The electrostatic interaction, which can arise from image charges, work function differences or patch potentials can be described by $P_{att} \propto 1/h^2$.[64,160,161] To further study the power law model considering different origins of the interaction, we varied the geometry of the annular ring. The pull-in distance for 1-4 layers
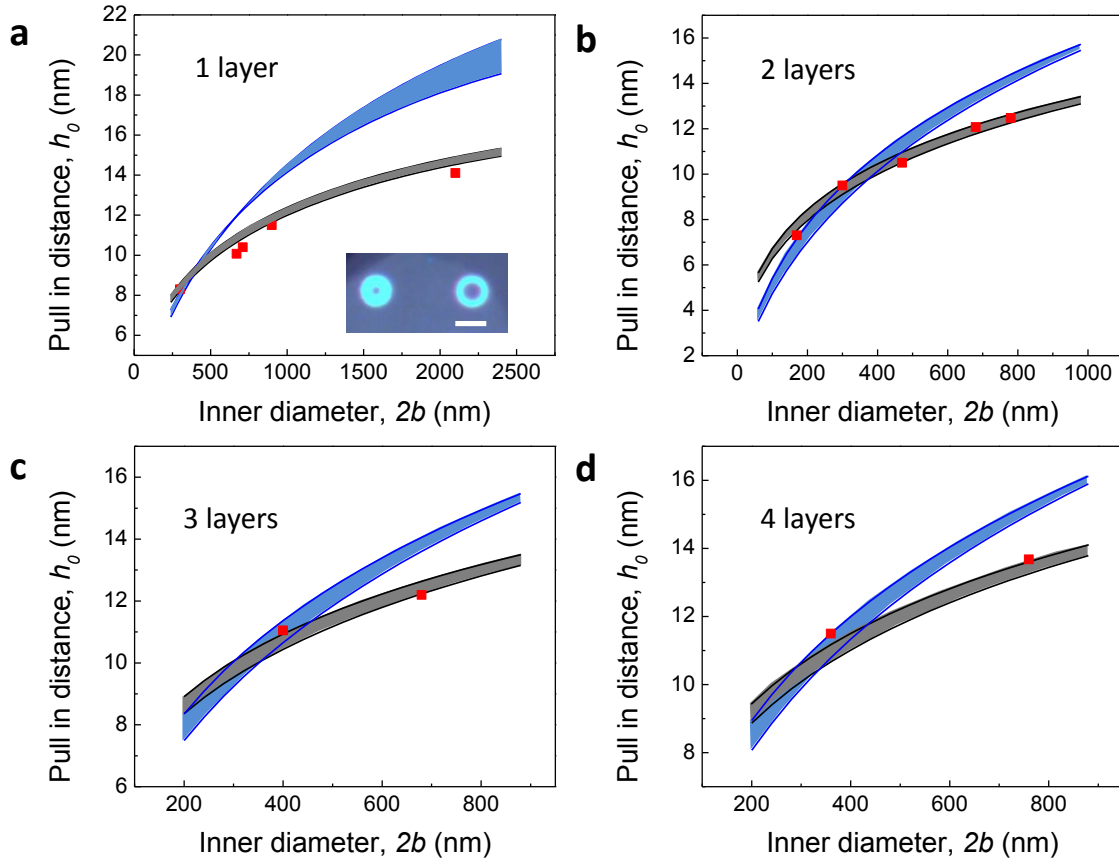
Figure 6.5 Scaling of the Pull in Distance with P_{att}. Pull in distance, h_0, vs. inner diameter, $2b$, for a) 1 layer b) 2 layer c) 3 layer d) 4 layer graphene flakes (verified by Raman spectroscopy) with identical outer diameter but different inner diameters. The black and blue shaded lines are the calculated results for 2 different power law dependences $P_{att} = \beta/h^4$ (black) and $P_{att} = \alpha/h^2$ (blue) with $S_0 = 0.03 - 0.09$ N/m. The values of β and α are listed in supplementary material. a) (inset) Optical image of 2 of the measured monolayer devices. The scale bar = 5 μm.

graphene membranes with an identical outer diameter but a different inner diameter is shown in Figure 6.5. The pull in distance shows a slight increase with increasing b. A theoretical calculation based on our analytical model using $P_{att} = \beta/h^4$ and the calculated values of β in Figure 6.2b, is shown as a black shaded line in Figure 6.3. The boundaries of the shaded lines show the range of values for $S_0 = 0.03 - 0.09$ N/m.[151]

To determine if electrostatic forces play a significant role in our measurements, we fit the data in Figure 6.1e and Figure 6.3 with a model in which an electrostatic force takes the form, $P_{att} = \alpha/h^2$, and we use the same strategy to determine α as was used to calculate β above. Doing so for the monolayer devices in Figure 1e, gives $\alpha = 0.49$ pN (for $S_0 = 0.07$ N/m). We can also use these values of α to fit the data in Figure 6.3. This is shown as a shaded blue line which fits poorly to the data. A good fit would require that α increase with inner post diameter for all the devices measured, while no such assumption is needed for β. To fit all of our measured pull-in distances (51 devices in 17 geometries from 5 different chips) using an electrostatic force model requires that α values vary from $0.15 - 1.79$ pN across all the devices. A model based on an inverse 3rd power dependence was also examined and does not fit all the data as well as the inverse fourth power dependence (see Appendix A3).

6.8 Materials Dependence

To test the material dependence of the interfacial interaction with graphene, we also carried out experiments where we measured the pull-in distance between graphene and a gold coated annular ring that were electrically contacted and grounded. 2-5 layers graphene membranes (17 devices in 6 similar geometries from 4 chips) were measured. The pull in distance varied between 9 nm and 18 nm for annular rings with a = 1-1.75 µm and

95
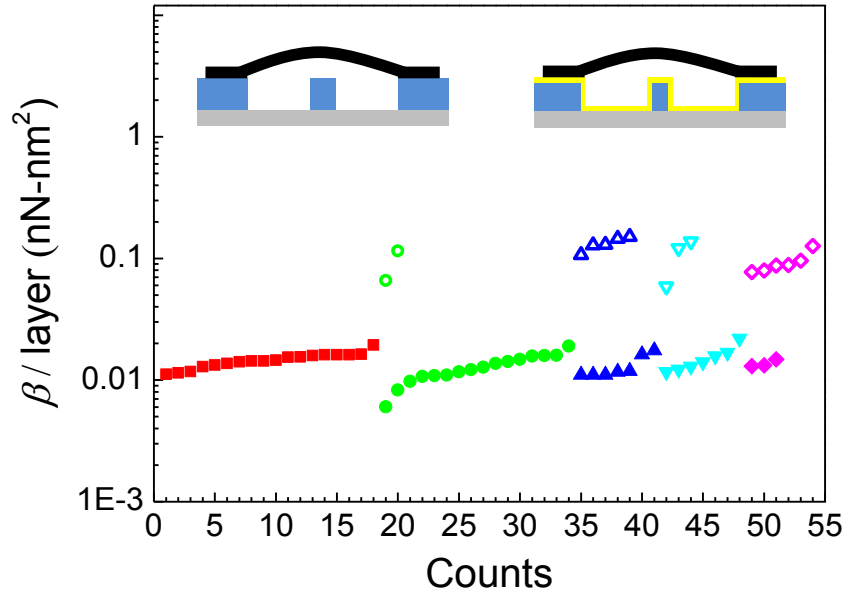
Figure 6.6 Modelled vdW force vs. Number of Layers for SiO_x and Gold. Measured β / *Number* of graphene layers between SiO_x and 1 layer graphene (solid red squares), 2 layer graphene (solid green circles), 3 layer graphene (solid blue up triangles), 4 layer graphene (solid cyan down triangles), 5 layer graphene (solid magenta diamond), and β / *number* of graphene layers between Au and 2 layer graphene (hollow green circles), 3 layer graphene (hollow blue up triangles), 4 layer graphene (hollow cyan down triangles), and 5 layer graphene (hollow magenta diamond). The average and standard deviation of β / *Number* of graphene layers between SiO_x and graphene are 0.0179 ± 0.0037 nN-nm^2 / layer. The average and standard deviation of β / *Number* of graphene layers between Au and graphene are 0.104 ± 0.031 nN-nm^2 / layer. Each data point corresponds to a separate device. (top left inset) Side view schematic of the pressurized suspended graphene on the annular ring with SiO_x surface. (top right inset) Side view schematic of the pressurized suspended graphene on an Au coated annular ring.

b = 0.15-0.6 μm, slightly larger than the measured pull-in distances for uncoated SiO_x posts of a similar geometry. Using the same theoretical analysis as with the graphene/SiO_x data, we determined the average value and standard deviation of β / # of graphene layers between the Au coated post and electrically grounded graphene to be 0.104 ± 0.031 nN-nm^2 / layer; these are about an order of magnitude higher than those for graphene interacting with SiO_x (Figure 6.6). The graphene/Au values agrees reasonably well with the theoretical predictions based on a Lifshitz formula of graphene interacting with gold at 15 nm separation, $\beta = 0.08$ nN-nm^2.

6.9   *Deformation of Graphene Membranes by vdW Force*

The extreme flexibility of the suspended graphene coupled with the large magnitude of the interfacial force at these short separations shows up as a statically deformed membrane right before pull-in for some devices. This is especially evident for a graphene membrane with a small inner post – more localized force- and a large outer diameter – more flexible graphene (Figure 6.5). The AFM image shows a graphene membrane locally deformed at its center shortly before pull-in (Figure 6.7a). The AFM line cut through the center (Figure 6.7b) shows this deformation to be about 2 nm. This deformation is further verified by the analytical model which shows a number of stable configurations for graphene membranes deformed by P_{att} at these dimensions and separations (Figure 6.7c).
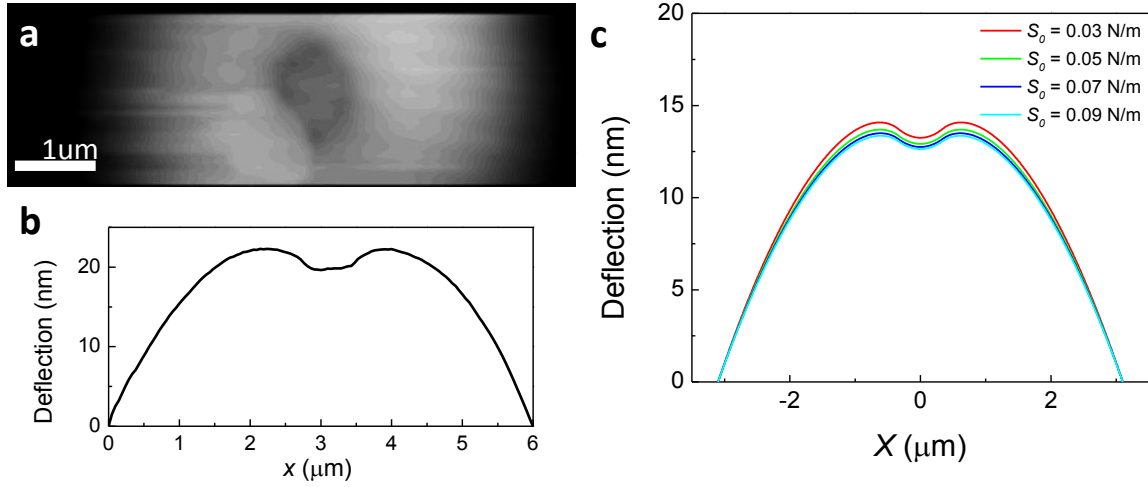
Figure 6.7 Deforming a Graphene Membrane with the vdW Force. a) An atomic force microscope image showing a close up view of the top part of the pressurized graphene membrane right before pull-in showing the deformation at the center of the membrane resulting from the vdW force. b) A line cut through the center of the image in (a). c) Calculated deflection vs. position through the center of a graphene membrane using the analytical model, for varying S_0.

6.10 Conclusion

In conclusion, we observed the pull in instability at 10nm-20nm distance on graphene by the attractive interfacial forces between graphene and SiO_x/Au, and found them to agree very well with a form $P_{att} = \beta/h^4$, consistent with recently calculated values of long range vdW forces between graphene and SiO_x and graphene and gold. Furthermore, the strength of the force scales linearly with layer numbers, which is compatible with the additive nature of vdW forces. It is noteworthy that our experimental configuration is essentially a realization of a parallel plate geometry by self-alignment to measure interfacial forces acting on atomically thin, two-dimensional materials[41]. These experiments which provide a measurement of the magnitude and power law dependence of the interfacial forces at 10-20 nm separations between graphene and 2 common substrates can guide the development of nanomechanical devices from single and few layer graphene sheets where these forces are critical to their effective operation.[7,71,123]

Chapter 7

Biaxial Strain Engineering in Suspended Monolayer MoS$_2$

7.1 Introduction

Electronic band structure modulation in materials is desirable for a wide range of electronics and optoelectronic applications.[162] Strain engineering has the potential to achieve fast, continuous, and reversible band structure tuning in a low cost manner.[163,164] Furthermore, it can be used to improve the performance of devices, such as to increase the charge carrier mobility in semiconductors or to raise the emission efficiency of light emission devices.[165,166] 2 dimensional (2D) materials, typically graphene and MoS$_2$, have proved to be exceptional candidates for the applications in electronics and optoelectronics.[10,22–25,167] Therefore, strain engineering in 2D materials is attracting interest especially considering their extremely high intrinsic limit of stretching up to ~25% for graphene and ~11% for MoS$_2$.[28,29,47] However, uniaxial tensile strains of a few percent cannot open an appreciable band gap in graphene, even though its band structure is modified with a deformation of the Dirac cone and the displacement of Dirac cone away from the K point.[109,110] Compared with graphene, MoS$_2$ is a more interesting material for band gap engineering with strain since it has a direct band gap for monolayer and an indirect band gap for multilayers.[43,46] Previous experimental studies indicate that a redshift rate with uniaxial strain of ~50 meV/% for the direct band gap in both monolayer and bilayers, and ~100 meV/% for the indirect band gap in bilayers.[115–118,168] The only study

with biaxial strain shows an unexpected high tuning rate of more than 300 meV/% for the direct bandgap of tri-layer MoS_2 grown by CVD, but the strain applied was just up to 0.2 % due to a limit in the electromechanical actuation provided by the piezoelectric device used to strain the MoS_2.[119] Here, we study the band gap engineering in suspended monolayer MoS_2 with elastic biaxial strain applied by a uniform pressure across the membrane.

7.2   Fabrication

The suspended MoS_2 membranes are also fabricated by a bottom up method similar to the fabrication introduced in Chapter 5 and 6.[62,69,151,169] The fabrication starts with patterning and etching of arrays of circular cavities of 5 μm diameter and more than ~250 nm depth on the silicon wafer with 285 nm SiO_2. The chips are also cleaned with Nanostrip after removal of photoresist with acetone and isopropanol. 1-3 layers MoS_2 flakes are mechanically exfoliated on the silicon wafer to cover the wells, forming free standing circular membranes. Figure 7.1a shows an optical image of a MoS_2 flake containing both monolayer and bilayer free standing membranes. The schematic of a bulged membrane is shown in Figure 7.1b. Noticeably, the yield of monolayer and few layers MoS_2 membranes is significantly lower than that of graphene with the same mechanical exfoliation processes, and the size of exfoliated MoS_2 flakes are always smaller. Possible reasons include higher adhesion energy between MoS_2 layers, lower attractive interfacial forces between MoS_2 flakes and the substrate, and higher density of defects in MoS_2 flakes.   The number of layers is counted with optical contrast, Raman microscopy, and photoluminescence. Similarly, trained eyes can also tell the number of layers in 1-3 layers MoS_2 flakes. Since MoS_2 is semiconductor, we can use photoluminescence to measure the bandgap of
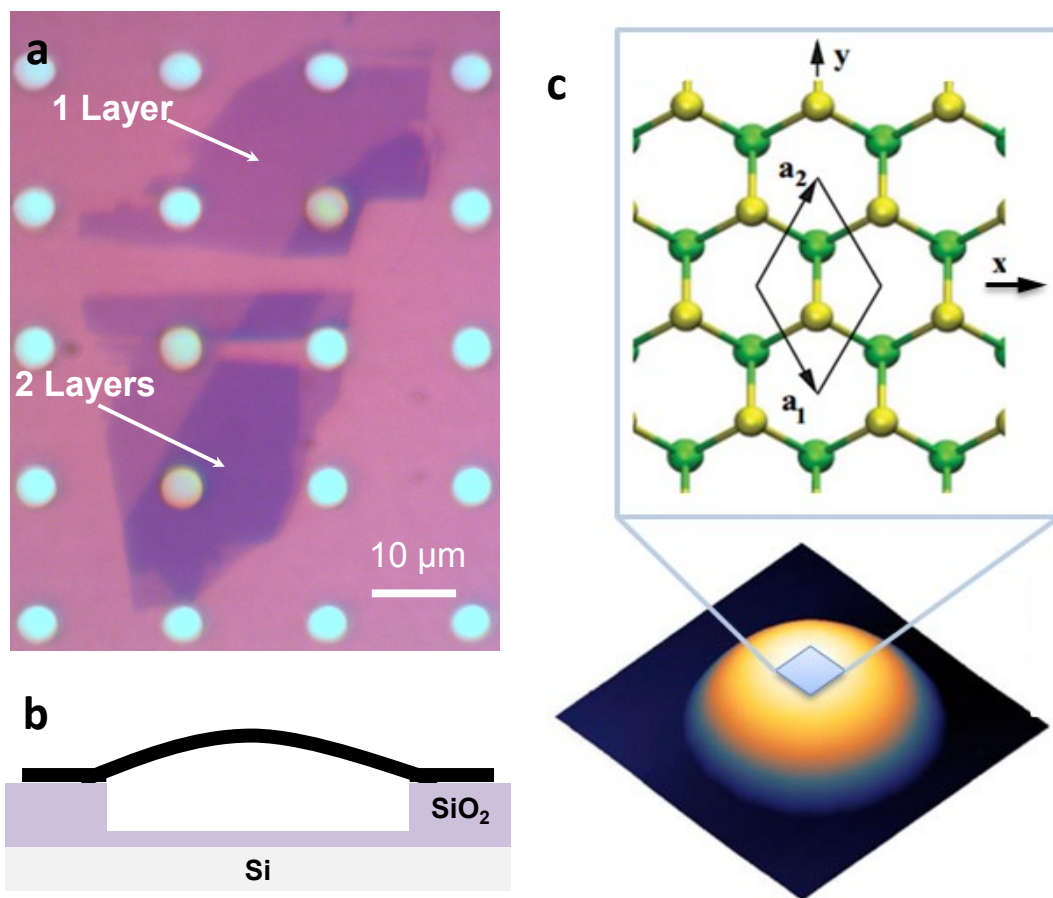
Figure 7.1 a) optical image of a MoS$_2$ flake containing both monolayer and bilayer free standing membranes. b) schematic of a bulged MoS$_2$ membrane. c) (lower) AFM image of a bulged MoS$_2$ membrane, (upper) atomic structure of monolayer MoS$_2$ under biaxial strain.[112]

the flake, especially for the freestanding parts, which turns out to be a good way to verify

number of layers in the flake.[43] Raman and PL spectrums taken on the supported part of MoS_2

can also be used to count the # of layers by comparing the spectrums with reported results.[46,115]

7.3 Biaxial Straining

Biaxial strain is applied on the MoS_2 membrane by a similar process as used in Chapter 5.

The circular membranes are charged with pressure differences thereby making the membranes

bulge up as spherical caps, and the center of the membrane is under biaxial strain accordingly.

The strain ε can be derived from the deflection of the bulge measured with AFM. As introduced

in Chapter 2 for the mechanics of pressurized circular membranes, we use equation 2.11 to

estimate the biaxial strain at the center of the bulged MoS_2 spherical cap,

$$\varepsilon = \frac{2z^2}{3a^2} \tag{7.1}$$

where z is the deflection of the spherical cap, and a is the radius of the circular membrane

without bulging. An example of a pressurized MoS_2 membrane is shown in Figure 7.1c.

7.4 Direct Bandgap Energy Tuning in Monolayer

The PL spectrums are measured with an optical microscope coupled to a grating

spectrometer under ambient conditions at room temperature. An average laser power of ~ 200

μW is used to avoid heating. The suspended MoS_2 membranes are excited with a CW solid state

laser at a wavelength of 532 nm. The PL spectrums are taken at the center of the membrane if not

indicated otherwise. In the energy range of 1.33 eV – 2.41 eV measured, suspended monolayer
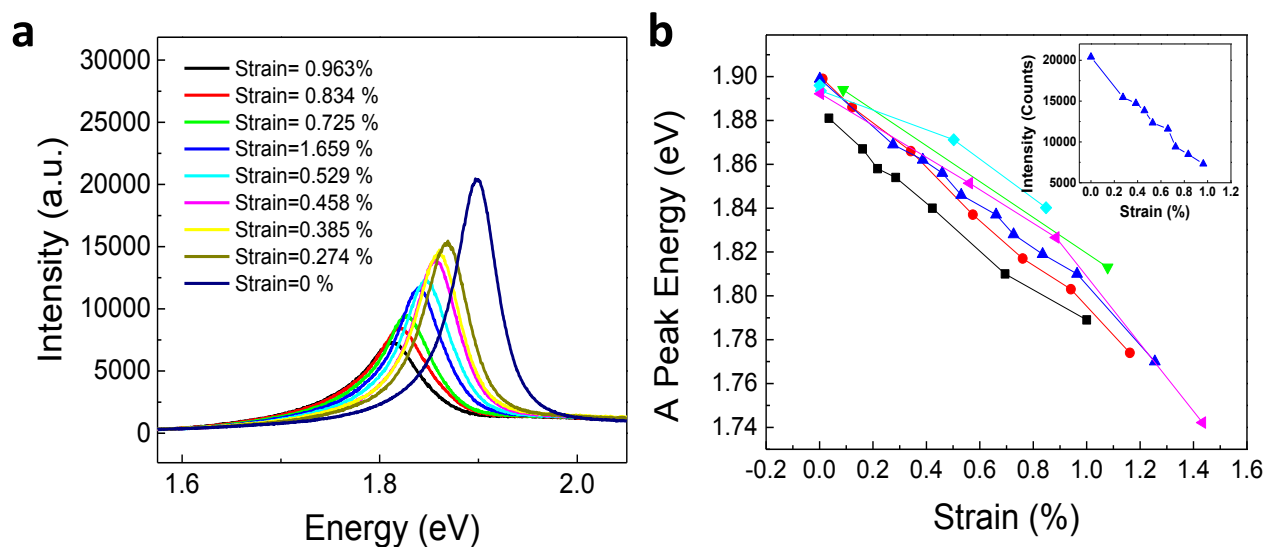
Figure 7.2 PL of monolayer MoS$_2$ a) PL of a suspended monolayer MoS$_2$ membrane with applied biaxial strain up to ~ 1%. b) Measured direct bandgap (A peak) energy from 6 monolayer MoS$_2$ membranes under different biaxial strain values. Inset is the normalized intensity of A peak of the PL spectra shown in (a) versus the biaxial strain applied.

samples show a single sharp PL peak (A peak) at 1.90 eV of ~50 meV width, corresponding to the direct bandgap energy in the sample. Therefore, suspended monolayer is more suited for the observation of bandgap energy modulation with elastic strain compared to supported monolayer samples, in which the intensity of PL peak at 1.9 eV decreases substantially due to the influence from the substrate. Figure 7.2a shows the shift of PL spectra with applied biaxial strains up to ~ 1% with each step of about 0.1 %. The spectra are normalized with the MoS_2 Raman peak even though its intensity is much smaller compared to the A peak. Both bandgap energy (Cyan color spots in Figure 7.2b) and peak intensity (Figure 7.2c) indicated by the spectra decrease with the increase of strain. The bandgap shifting rate with biaxial strain is 98.6 ± 3.1 meV/%, which is about twice of the value due to uniaxial strain on monolayer MoS_2 but very close to the previously reported theoretically expected values.[112] We did the similar measurements on 6 monolayer membranes with the maximum biaxial strain up to ~ 1%, and they all demonstrate the same trend with similar bandgap tuning rates as shown in Figure 7.2b with different colors representing different samples, respectively.

7.5   Conclusion

In conclusion, we demonstrate modulation of the electronic band structure in monolayer suspended MoS_2 membranes with local biaxial strain. We observed a linear direct band gap (A peak) decrease rate of ~100 meV in monolayer, which is the twice of the change rate with uniaxial strain.

Reference

[1]   H. G. Craighead, *Science* **2000**, *290*, 1532.

[2]   M. Roukes, *Phys. World* **2001**, *14*, 25.

[3]   K. L. Ekinci, M. L. Roukes, *Rev. Sci. Instrum.* **2005**, *76*, 61101.

[4]   C. Chen, J. Hone, *Proc. IEEE* **2013**, *101*, 1766.

[5]   J. L. Arlett, E. B. Myers, M. L. Roukes, *Nat Nano* **2011**, *6*, 203.

[6]   J. P. Salvetat, J. M. Bonard, N. H. Thomson, A. J. Kulik, L. Forró, W. Benoit, L. Zuppiroli, *Appl. Phys. A Mater. Sci. Process.* **1999**, *69*, 255.

[7]   J. S. Bunch, A. M. van der Zande, S. S. Verbridge, I. W. Frank, D. M. Tanenbaum, J. M. Parpia, H. G. Craighead, P. L. McEuen, *Science* **2007**, *315*, 490.

[8]   W. Lu, C. M. Lieber, *Nat Mater* **2007**, *6*, 841.

[9]   B. D. Davidson, S. M. George, V. M. Bright, in *Micro Electro Mech. Syst. (MEMS), 2010 IEEE 23rd Int. Conf.*, **2010**, pp. 424–427.

[10]   Q. H. Wang, K. Kalantar-Zadeh, A. Kis, J. N. Coleman, M. S. Strano, *Nat Nano* **2012**, *7*, 699.

[11]   T.-H. Lee, S. Bhunia, M. Mehregany, *Science* **2010**, *329*, 1316.

[12]   O. Loh, X. Wei, J. Sullivan, L. E. Ocola, R. Divan, H. D. Espinosa, *Adv. Mater.* **2012**, *24*, 2463.

[13]   T. Rueckes, K. Kim, E. Joselevich, G. Y. Tseng, C.-L. Cheung, C. M. Lieber, *Science* **2000**, *289*, 94.

[14]   K. S. Kim, Y. Zhao, H. Jang, S. Y. Lee, J. M. Kim, K. S. Kim, J.-H. Ahn, P. Kim, J.-Y. Choi, B. H. Hong, *Nature* **2009**, *457*, 706.

[15]   S. Bae, H. Kim, Y. Lee, X. Xu, J.-S. Park, Y. Zheng, J. Balakrishnan, T. Lei, H. Ri Kim, Y. Il Song, Y.-J. Kim, K. S. Kim, B. Ozyilmaz, J.-H. Ahn, B. H. Hong, S. Iijima, *Nat Nano* **2010**, *5*, 574.

[16]   X. Li, W. Cai, J. An, S. Kim, J. Nah, D. Yang, R. Piner, A. Velamakanni, I. Jung, E. Tutuc, S. K. Banerjee, L. Colombo, R. S. Ruoff, *Science* **2009**, *324*, 1312.

[17]   Y. Hao, M. S. Bharathi, L. Wang, Y. Liu, H. Chen, S. Nie, X. Wang, H. Chou, C. Tan, B. Fallahazad, H. Ramanarayan, C. W. Magnuson, E. Tutuc, B. I. Yakobson, K. F. McCarty, Y.-W. Zhang, P. Kim, J. Hone, L. Colombo, R. S. Ruoff, *Sci.* **2013**, *342* , 720.

[18]   K. S. Novoselov, A. K. Geim, S. V Morozov, D. Jiang, Y. Zhang, S. V Dubonos, I. V Grigorieva, A. A. Firsov, *Science* **2004**, *306*, 666.

[19]   J. I. Gersten, F. W. Smith, *The Physics and Chemistry of Materials*, John Wiley & Sons, Inc, New York, **2001**.

[20]   M. Chhowalla, H. S. Shin, G. Eda, L.-J. Li, K. P. Loh, H. Zhang, *Nat Chem* **2013**, *5*, 263.

[21]   M. Xu, T. Liang, M. Shi, H. Chen, *Chem. Rev.* **2013**, *113*, 3766.

[22]   A. K. Geim, K. S. Novoselov, *Nat Mater* **2007**, *6*, 183.

[23]   K. S. Novoselov, D. Jiang, F. Schedin, T. J. Booth, V. V Khotkevich, S. V Morozov, A. K. Geim, *Proc. Natl. Acad. Sci. United States Am.* **2005**, *102* , 10451.

[24]   A. K. Geim, I. V Grigorieva, *Nature* **2013**, *499*, 419.

[25]   A. K. Geim, *Science* **2009**, *324*, 1530.

[26]   J. R. Williams, L. DiCarlo, C. M. Marcus, *Science* **2007**, *317*, 638.

[27]   J. Baringhaus, M. Ruan, F. Edler, A. Tejeda, M. Sicot, AminaTaleb-Ibrahimi, A.-P. Li, Z. Jiang, E. H. Conrad, C. Berger, C. Tegenkamp, W. A. de Heer, *Nature* **2014**, *advance on*.

[28]   G.-H. Lee, R. C. Cooper, S. J. An, S. Lee, A. van der Zande, N. Petrone, A. G. Hammerberg, C. Lee, B. Crawford, W. Oliver, J. W. Kysar, J. Hone, *Sci.* **2013**, *340* , 1073.

[29]   C. Lee, X. Wei, J. W. Kysar, J. Hone, *Science* **2008**, *321*, 385.

[30]   F. Bonaccorso, Z. Sun, T. Hasan, A. C. Ferrari, *Nat Phot.* **2010**, *4*, 611.

[31]   A. A. Balandin, S. Ghosh, W. Bao, I. Calizo, D. Teweldebrhan, F. Miao, C. N. Lau, *Nano Lett.* **2008**, *8*, 902.

[32]   J. S. Bunch, S. S. Verbridge, J. S. Alden, A. M. van der Zande, J. M. Parpia, H. G. Craighead, P. L. McEuen, *Nano Lett.* **2008**, *8*, 2458.

[33]   P. Y. Huang, C. S. Ruiz-Vargas, A. M. van der Zande, W. S. Whitney, M. P. Levendorf, J. W. Kevek, S. Garg, J. S. Alden, C. J. Hustedt, Y. Zhu, J. Park, P. L. McEuen, D. A. Muller, *Nature* **2011**, *469*, 389.

[34]   S. Bhaviripudi, X. Jia, M. S. Dresselhaus, J. Kong, *Nano Lett.* **2010**, *10,* 4128.

[35]   I. Vlassiouk, M. Regmi, P. Fulvio, S. Dai, P. Datskos, G. Eres, S. Smirnov, *ACS Nano* **2011**, *5*, 6069.

[36]   Z. Yan, J. Lin, Z. Peng, Z. Sun, Y. Zhu, L. Li, C. Xiang, E. L. Samuel, C. Kittrell, J. M. Tour, *ACS Nano* **2012**, *6*, 9110.

[37] H. Wang, G. Wang, P. Bao, S. Yang, W. Zhu, X. Xie, W.-J. Zhang, *J. Am. Chem. Soc.* **2012**, *134*, 3627.

[38] X. Li, Y. Zhu, W. Cai, M. Borysiak, B. Han, D. Chen, R. D. Piner, L. Colombo, R. S. Ruoff, *Nano Lett.* **2009**, *9*, 4359.

[39] J. W. Suk, A. Kitt, C. W. Magnuson, Y. Hao, S. Ahmed, J. An, A. K. Swan, B. B. Goldberg, R. S. Ruoff, *ACS Nano* **2011**, *5*, 6916.

[40] Y. Lee, S. Bae, H. Jang, S. Jang, S.-E. Zhu, S. H. Sim, Y. Il Song, B. H. Hong, J.-H. Ahn, *Nano Lett.* **2010**, *10*, 490.

[41] W. H. Lee, J. W. Suk, J. Lee, Y. Hao, J. Park, J. W. Yang, H.-W. Ha, S. Murali, H. Chou, D. Akinwande, K. S. Kim, R. S. Ruoff, *ACS Nano* **2012**, *6*, 1284.

[42] Y. REN, C. ZHU, W. CAI, H. LI, Y. HAO, Y. WU, S. CHEN, Q. WU, R. D. PINER, R. S. RUOFF, *Nano* **2012**, *07*, 1150001.

[43] K. F. Mak, C. Lee, J. Hone, J. Shan, T. F. Heinz, *Phys. Rev. Lett.* **2010**, *105*, 136805.

[44] RadisavljevicB., RadenovicA., BrivioJ., GiacomettiV., KisA., *Nat Nano* **2011**, *6*, 147.

[45] O. Lopez-Sanchez, D. Lembke, M. Kayci, A. Radenovic, A. Kis, *Nat Nano* **2013**, *8*, 497.

[46] A. Splendiani, L. Sun, Y. Zhang, T. Li, J. Kim, C.-Y. Chim, G. Galli, F. Wang, *Nano Lett.* **2010**, *10*, 1271.

[47] S. Bertolazzi, J. Brivio, A. Kis, *ACS Nano* **2011**, *5*, 9703.

[48] A. M. van der Zande, P. Y. Huang, D. A. Chenet, T. C. Berkelbach, Y. You, G.-H. Lee, T. F. Heinz, D. R. Reichman, D. A. Muller, J. C. Hone, *Nat Mater* **2013**, *12*, 554.

[49] J. R. William. D. Callister, *Materials Science and Engineering: An Introduction*, Wiley, **2006**.

[50] S. P. Timoshenko, S. W. Krieger, *Theory of Plates and Shells*, McGraw-Hill, Inc., **1959**.

[51] A. C. Ugural, *Stresses in Beams, Plates, and Shells*, CRC Press, Boca Raton, FL, **2009**.

[52] M. K. Small, W. D. Nix, *J. Mater. Res.* **1992**, *7*, 1553.

[53] J. W. Beams, *Structure and Principles of Thin Films*, John Wiley & Sons, Inc, New York, **1959**.

[54] H. Hencky, *Z. Fur Math. Und Phys.* **1915**, *63*, 311.

[55] J. G. Williams, *Int. J. Fract.* **1997**, *87*, 265.

[56] S. P. Koenig, N. G. Boddeti, M. L. Dunn, J. S. Bunch, *Nat Nano* **2011**, *6*, 543.

[57]   T. Yoon, W. C. Shin, T. Y. Kim, J. H. Mun, T.-S. Kim, B. J. Cho, *Nano Lett.* **2012**, *12*, 1448.

[58]   J. S. Bunch, M. L. Dunn, *Solid State Commun.* **2012**, *152*, 1359.

[59]   B. N. Chapman, *J. Vac. Sci. Technol.* **1974**, *11*, 106.

[60]   J. Valli, *J. Vac. Sci. Technol. A Vacuum, Surfaces, Film.* **1986**, *4*, 3007.

[61]   M. G. Allen, S. D. Senturia, *J. Adhes.* **1989**, *29*, 219.

[62]   N. G. Boddeti, X. Liu, R. Long, J. Xiao, J. S. Bunch, M. L. Dunn, *Nano Lett.* **2013**, *13*, 6216.

[63]   J. Visser, *Adv. Colloid Interface Sci.* **1972**, *3*, 331.

[64]   J. N. Israelachvili, *Intermolecular And Surface Forces*, Academic Press, **2010**.

[65]   Z. H. Aitken, R. Huang, *J. Appl. Phys.* **2010**, *107*.

[66]   G. T. A. Kovacs, *Micromachined Transducers: Sourcebook*, WCB/MacGraw-Hill, **1998**.

[67]   S. M. Sze, *Semiconductor Sensors*, J. Wiley, **1994**.

[68]   K. E. Petersen, *IBM J. Res. Dev.* **1979**, *23*, 376.

[69]   X. Liu, N. G. Boddeti, M. R. Szpunar, L. Wang, M. A. Rodriguez, R. Long, J. Xiao, M. L. Dunn, J. S. Bunch, *Nano Lett.* **2013**, *13*, 2309.

[70]   T. N. Theis, P. M. Solomon, *Science* **2010**, *327*, 1600.

[71]   K. M. Milaninia, M. A. Baldo, A. Reina, J. Kong, *Appl. Phys. Lett.* **2009**, *95*, 183103.

[72]   Z. Shi, H. Lu, L. Zhang, R. Yang, Y. Wang, D. Liu, H. Guo, D. Shi, H. Gao, E. Wang, G. Zhang, *Nano Res.* **2011**, *5*, 82.

[73]   S. M. Kim, E. B. Song, S. Lee, S. Seo, D. H. Seo, Y. Hwang, R. Candler, K. L. Wang, *Appl. Phys. Lett.* **2011**, *99*, 23103.

[74]   B. Standley, W. Bao, H. Zhang, J. Bruck, C. N. Lau, M. Bockrath, *Nano Lett.* **2008**, *8*, 3345.

[75]   H. Zhang, W. Bao, Z. Zhao, J.-W. Huang, B. Standley, G. Liu, F. Wang, P. Kratz, L. Jing, M. Bockrath, C. N. Lau, *Nano Lett.* **2009**, *12*, 1772.

[76]   P. Kim, C. M. Lieber, *Science* **1999**, *286*, 2148.

[77]   J. E. Jang, S. N. Cha, Y. Choi, G. A. J. Amaratunga, D. J. Kang, D. G. Hasko, J. E. Jung, J. M. Kim, *Appl. Phys. Lett.* **2005**, *87*, 163114.

[78] J. E. Jang, S. N. Cha, Y. Choi, T. P. Butler, D. J. Kang, D. G. Hasko, J. E. Jung, Y. W. Jin, J. M. Kim, G. A. J. Amaratunga, *Appl. Phys. Lett.* **2008**, *93*, 113105.

[79] S. W. Lee, D. S. Lee, R. E. Morjan, S. H. Jhang, M. Sveningsson, O. A. Nerushev, Y. W. Park, E. E. B. Campbell, *Nano Lett.* **2004**, *4*, 2027.

[80] A. B. Kaul, E. W. Wong, L. Epp, B. D. Hunt, *Nano Lett.* **2006**, *6*, 942.

[81] S. N. Cha, J. E. Jang, Y. Choi, G. A. J. Amaratunga, D. J. Kang, D. G. Hasko, J. E. Jung, J. M. Kim, *Appl. Phys. Lett.* **2005**, *86*, 83103.

[82] J. W. Ward, M. Meinhold, B. M. Segal, J. Berg, R. Sen, R. Sivarajan, D. K. Brock, T. Rueckes, in *Non-Volatile Mem. Technol. Symp. 2004*, **2004**, pp. 34–38.

[83] D. A. Czaplewski, G. A. Patrizi, G. M. Kraus, J. R. Wendt, C. D. Nordquist, S. L. Wolfley, M. S. Baker, M. P. de Boer, *J. Micromechanics Microengineering* **2009**, *19*, 85003.

[84] R. Parsa, M. Shavezipur, W. S. Lee, S. Chong, D. Lee, H. S. P. Wong, R. Maboudian, R. T. Howe, in *Micro Electro Mech. Syst. (MEMS), 2011 IEEE 24th Int. Conf.*, **2011**, pp. 1361–1364.

[85] W. S. Lee, S. Chong, R. Parsa, J. Provine, D. Lee, S. Mitra, H. S. P. Wong, R. T. Howe, in *Solid-State Sensors, Actuators Microsystems Conf. (TRANSDUCERS), 2011 16th Int.*, **2011**, pp. 2606–2609.

[86] M. G. Joe Brewer, *Nonvolatile Memory Technologies with Emphasis on Flash: A Comprehensive Guide to Understanding and Using Flash Memory Devices*, Wiley-IEEE Press, **2008**.

[87] M. G. Jim Hutchby, *Workshop ERD/ERM Work. Gr. Meetin* **2010**.

[88] J. N. Israelachvili, D. Tabor, *Proc. R. Soc. London. A. Math. Phys. Sci.* **1972**, *331*, 19.

[89] I. E. Dzyaloshinskii, E. M. Lifshitz, L. P. Pitaevskii, *Adv. Phys.* **1961**, *10*, 165.

[90] H. B. G. Casimir, *Proc. K. Ned. Akad. Wet* **1948**.

[91] E. M. Lifshitz, *Sov. Phys. Jetp-Ussr* **1956**, *2*, 73.

[92] D. Tabor, R. H. S. Winterton, *Proc. R. Soc. London. A. Math. Phys. Sci.* **1969**, *312*, 435.

[93] S. M.J, *Physica* **1958**, *24*, 751.

[94] B. V Derjaguin, I. I. Abrikossova, *J. Phys. Chem. Solids* **1958**, *5*, 1.

[95] R. Maboudian, R. T. Howe, *J. Vac. Sci. Technol. B Microelectron. Nanom. Struct.* **1997**, *15*, 1.

[96] F. W. DelRio, M. P. de Boer, J. A. Knapp, E. David Reedy, P. J. Clews, M. L. Dunn, *Nat Mater* **2005**, *4*, 629.

[97]   H. B. Chan, V. A. Aksyuk, R. N. Kleiman, D. J. Bishop, F. Capasso, *Science* **2001**, *291*, 1941.

[98]   A. W. Rodriguez, F. Capasso, S. G. Johnson, *Nat Phot.* **2010**, *5*, 211.

[99]   F. Capasso, J. N. Munday, D. Iannuzzi, H. B. Chan, *Sel. Top. Quantum Electron. IEEE J.* **2007**, *13*, 400.

[100]   H. B. Chan, V. A. Aksyuk, R. N. Kleiman, D. J. Bishop, F. Capasso, *Science* **2001**, *291*, 1941.

[101]   H. B. Chan, V. A. Aksyuk, R. N. Kleiman, D. J. Bishop, F. Capasso, *Phys. Rev. Lett.* **2001**, *87*, 211801.

[102]   S. Scharfenberg, N. Mansukhani, C. Chialvo, R. L. Weaver, N. Mason, *Appl. Phys. Lett. **2011**, 100*, 21910.

[103]   M. Bordag, B. Geyer, G. L. Klimchitskaya, V. M. Mostepanenko, *Phys. Rev. B* **2006**, *74*, 205431.

[104]   D. Drosdoff, L. M. Woods, *Phys. Rev. B* **2010**, *82*, 155459.

[105]   M. A. and M. Porfiri, *Smart Mater. Struct.* **2012**, *21*, 105030.

[106]   M.-F. Yu, T. Kowalewski, R. S. Ruoff, *Phys. Rev. Lett.* **2001**, *86*, 87.

[107]   A. V Desai, M. A. Haque, *Appl. Phys. Lett.* **2007**, *90*, 33102.

[108]   C.-H. Ge, C.-C. Lin, C.-H. Ko, C.-C. Huang, Y.-C. Huang, B.-W. Chan, B.-C. Perng, C.-C. Sheu, P.-Y. Tsai, L.-G. Yao, C.-L. Wu, T.-L. Lee, C.-J. Chen, C.-T. Wang, S.-C. Lin, Y.-C. Yeo, C. Hu, *Electron Devices Meet. 2003. IEDM '03 Tech. Dig. IEEE Int.* **2003**, 3.7.1.

[109]   M. Huang, H. Yan, T. F. Heinz, J. Hone, *Nano Lett.* **2010**, *10*, 4074.

[110]   M. Huang, T. A. Pascal, H. Kim, W. A. Goddard, J. R. Greer, *Nano Lett.* **2011**, *11*, 1241.

[111]   K. F. Mak, K. He, C. Lee, G. H. Lee, J. Hone, T. F. Heinz, J. Shan, *Nat Mater* **2013**, *12*, 207.

[112]   T. Li, *Phys. Rev. B* **2012**, *85*, 235407.

[113]   H. Pan, Y.-W. Zhang, *J. Phys. Chem. C* **2012**, *116*, 11752.

[114]   L. Kou, C. Tang, Y. Zhang, T. Heine, C. Chen, T. Frauenheim, *J. Phys. Chem. Lett.* **2012**, *3*, 2934.

[115]   H. J. Conley, B. Wang, J. I. Ziegler, R. F. Haglund, S. T. Pantelides, K. I. Bolotin, *Nano Lett.* **2013**, *13*, 3626.

[116]   K. He, C. Poole, K. F. Mak, J. Shan, *Nano Lett.* **2013**, *13*, 2931.

[117]   C. R. Zhu, G. Wang, B. L. Liu, X. Marie, X. F. Qiao, X. Zhang, X. X. Wu, H. Fan, P. H. Tan, T. Amand, B. Urbaszek, *Phys. Rev. B* **2013**, *88*, 121301.

[118] A. Castellanos-Gomez, R. Roldán, E. Cappelluti, M. Buscema, F. Guinea, H. S. J. van der Zant, G. A. Steele, *Nano Lett.* **2013**, *13*, 5361.

[119] Y. Y. Hui, X. Liu, W. Jie, N. Y. Chan, J. Hao, Y.-T. Hsu, L.-J. Li, W. Guo, S. P. Lau, *ACS Nano* **2013**, *7*, 7126.

[120] *International Roadmap Committee Future Memory Devices Workshop Summary*, **2010**.

[121] P. Gammel, G. Fischer, J. Bouchaud, *Bell Labs Tech. J.* **2005**, *10*, 29.

[122] W. Han, A. L. Hsu, T. Palacios, *Microw. Mag. IEEE* **2012**, *13*, 114.

[123] O. Y. Loh, H. D. Espinosa, *Nat Nano* **2012**, *7*, 283.

[124] M. Liao, S. Hishita, E. Watanabe, S. Koizumi, Y. Koide, *Adv. Mater.* **2010**, *22*, 5393.

[125] J. O. Lee, Y.-H. Song, M.-W. Kim, M.-H. Kang, J.-S. Oh, H.-H. Yang, J.-B. Yoon, *Nat Nano* **2013**, *8*, 36.

[126] P. Li, Z. You, G. Haugstad, T. Cui, *Appl. Phys. Lett.* **2011**, *98*, 253103.

[127] S. W. Lee, S. J. Park, E. E. B. Campbell, Y. W. Park, *Nat Commun* **2011**, *2*, 220.

[128] S. Chong, B. Lee, K. B. Parizi, J. Provine, S. Mitra, R. T. Howe, H.-S. P. Wong, *Electron Devices Meet. (IEDM), 2011 IEEE Int.* **2011**, 30.5.1.

[129] K. Akarvardar, D. Elata, R. Parsa, G. C. Wan, K. Yoo, J. Provine, P. Peumans, R. T. Howe, H. S. P. Wong, in *Electron Devices Meet. 2007. IEDM 2007. IEEE Int.*, **2007**, pp. 299–302.

[130] J. E. Jang, S. N. Cha, Y. J. Choi, D. J. Kang, T. P. Butler, D. G. Hasko, J. E. Jung, J. M. Kim, A. J. AmaratungaGehan, *Nat Nano* **2008**, *3*, 26.

[131] H. Yang, J. Heo, S. Park, H. J. Song, D. H. Seo, K.-E. Byun, P. Kim, I. Yoo, H.-J. Chung, K. Kim, *Sci.* **2012**, *336*, 1140.

[132] C.-C. Chen, M. Aykol, C.-C. Chang, A. F. J. Levi, S. B. Cronin, *Nano Lett.* **2011**, *11*, 1863.

[133] K. D. and R. C. Batra, *J. Micromechanics Microengineering* **2009**, *19*, 35008.

[134] B. E. Artz, L. W. Cathey, *Solid-State Sens. Actuator Work. 1992. 5th Tech. Dig. IEEE* **1992**, 190.

[135] P. Osterberg, H. Yie, X. Cai, J. White, S. Senturia, *Micro Electro Mech. Syst. 1994, MEMS '94, Proceedings, IEEE Work.* **1994**, 28.

[136] P. R. Gray, *Analysis and Design of Analog Integrated Circuits*, Wiley, **2009**.

[137] V. B. Shenoy, C. D. Reddy, Y.-W. Zhang, *ACS Nano* **2010**, *4*, 4840.

[138] A. Pantano, D. M. Parks, M. C. Boyce, *J. Mech. Phys. Solids* **2004**, *52*, 789.

[139] C. S. Ruiz-Vargas, H. L. Zhuang, P. Y. Huang, A. M. van der Zande, S. Garg, P. L. McEuen, D. A. Muller, R. G. Hennig, J. Park, *Nano Lett.* **2011**, *11*, 2259.

[140] H. C. Nathanson, W. E. Newell, R. A. Wickstrom, J. R. Davis Jr., *Electron Devices, IEEE Trans.* **1967**, *14*, 117.

[141] SchneeweissP., GierlingM., VisanescuG., K. P., J. E., GuntherA., FortaghJ., *Nat Nano* **2012**, *7*, 515.

[142] S. Garaj, W. Hubbard, A. Reina, J. Kong, D. Branton, J. A. Golovchenko, *Nature* **2010**, *467*, 190.

[143] C. Chen, S. Rosenblatt, K. I. Bolotin, W. Kalb, P. Kim, I. Kymissis, H. L. Stormer, T. F. Heinz, J. Hone, *Nat Nano* **2009**, *4*, 861.

[144] J. Sarabadani, A. Naji, R. Asgari, R. Podgornik, *Phys. Rev. B* **2011**, *84*, 155407.

[145] Z. Zong, C.-L. Chen, M. R. Dokmeci, K. Wan, *J. Appl. Phys.* **2010**, *107*.

[146] S. K. Lamoreaux, *Phys. Rev. Lett.* **1997**, *78*, 5.

[147] J. Atalaya, A. Isacsson, J. M. Kinaret, *Nano Lett.* **2008**, *8*, 4196.

[148] W. Bao, F. Miao, Z. Chen, H. Zhang, W. Jang, C. Dames, C. N. Lau, *Nat Nano* **2009**, *4*, 562.

[149] W. H. D. and C. M. Wang, *Nanotechnology* **2009**, *20*, 75702.

[150] R. A. Barton, J. Parpia, H. G. Craighead, *J. Vac. Sci. Technol. B Microelectron. Nanom. Struct.* **2011**, *29*, 50801.

[151] L. Wang, J. J. Travis, A. S. Cavanagh, X. Liu, S. P. Koenig, P. Y. Huang, S. M. George, J. S. Bunch, *Nano Lett.* **2012**, *12*, 3706.

[152] O. L. Blakslee, D. G. Proctor, E. J. Seldin, G. B. Spence, T. Weng, *J. Appl. Phys.* **1970**, *41*.

[153] J. Sarabadani, A. Naji, R. Asgari, R. Podgornik, *Phys. Rev. B* **2011**, *84*, 155407.

[154] H.-J. Butt, M. Kappl, in *Surf. Interfacial Forces*, Wiley-VCH Verlag GmbH & Co. KGaA, **2010**, pp. 5–53.

[155] Z. Deng, N. N. Klimov, S. D. Solares, T. Li, H. Xu, R. J. Cannara, *Langmuir* **2012**, *29*, 235.

[156] Q. Li, C. Lee, R. W. Carpick, J. Hone, *Phys. status solidi* **2010**, *247*, 2909.

[157] N. Burnham, A. Kulik, in *Handb. Micro/Nano Tribol. Second Ed.*, CRC Press, **1998**.

[158] D. Beaglehole, H. K. Christenson, *J. Phys. Chem.* **1992**, *96*, 3395.

[159] L. Zitzler, S. Herminghaus, F. Mugele, *Phys. Rev. B* **2002**, *66*, 155436.

[160] C. C. Speake, C. Trenkel, *Phys. Rev. Lett.* **2003**, *90*, 160403.

[161] W. J. Kim, A. O. Sushkov, D. A. R. Dalvit, S. K. Lamoreaux, *Phys. Rev. A* **2010**, *81*, 22505.

[162] K.-H. Hong, J. Kim, S.-H. Lee, J. K. Shin, *Nano Lett.* **2008**, *8*, 1335.

[163] J. Feng, X. Qian, C.-W. Huang, J. Li, *Nat Phot.* **2012**, *6*, 866.

[164] J. Li, Z. Shan, E. Ma, *MRS Bull.* **2014**, *39*, 108.

[165] M. V Fischetti, S. E. Laux, *J. Appl. Phys.* **1996**, *80*.

[166] Q. Yang, W. Wang, S. Xu, Z. L. Wang, *Nano Lett.* **2011**, *11*, 4012.

[167] S. Z. Butler, S. M. Hollen, L. Cao, Y. Cui, J. A. Gupta, H. R. Gutiérrez, T. F. Heinz, S. S. Hong, J. Huang, A. F. Ismach, E. Johnston-Halperin, M. Kuno, V. V Plashnitsa, R. D. Robinson, R. S. Ruoff, S. Salahuddin, J. Shan, L. Shi, M. G. Spencer, M. Terrones, W. Windl, J. E. Goldberger, *ACS Nano* **2013**, *7*, 2898.

[168] S. Tongay, J. Zhou, C. Ataca, K. Lo, T. S. Matthews, J. Li, J. C. Grossman, J. Wu, *Nano Lett.* **2012**, *12*, 5576.

[169] X. Liu, J. W. Suk, N. G. Boddeti, L. Cantley, L. Wang, J. M. Gray, H. J. Hall, V. M. Bright, C. T. Rogers, M. L. Dunn, R. S. Ruoff, J. S. Bunch, *Adv. Mater.* **2014**, *26*, 1571.

[170] Y. K. Koh, M.-H. Bae, D. G. Cahill, E. Pop, *ACS Nano* **2010**, *5*, 269.

Appendix

A1. Counting the number of graphene layers

The pull-in distances in Fig. 1e were measured from two graphene flakes about 100 μm apart from each other on the same chip (Fig. A1). In the two graphene flakes, there were 13 one-layer, 9 two-layer, 5 three-layer, 5 four-layer, and 3 five-layer suspended membranes. For both the graphene/SiO_x and the graphene/Au annular rings, the number of graphene layers was verified using Raman spectroscopy and optical contrast.

In order to count the number of graphene layers used in chapter 5, we used optical contrast verified by Raman spectroscopy. Figure A1 (a) shows a graphene flake used in this study. The devices in Figure A1 (a) correspond to the devices in Figure 1e. The corresponding spots where Raman spectrum was taken for each device are shown as colored circles; red is 1 layer, green is 2 layers, blue is 3 layers, cyan is 4 layers and magenta is 5 layers. Figures A1 (b) shows the Raman spectrum taken from the spots of corresponding color in A1 (a), respectively. To verify the number of layers we found the ratio of the integrated intensity of the first order optical phonon peak and the graphene G peak (Fig. A1 (c)).[170]

To measure the Raman spectrum on the gold coated samples, we patterned areas that contained no Au/Cr over which Raman spectrum of the graphene was taken without interference from the gold film. We patterned 5 μm circular discs between the annular wells using photolithography which masked the subsequent thermal evaporation of Au/Cr onto the SiO_x. After evaporation and lift-off, the protected areas contained no Au/Cr while all other areas of the wafer were covered with the Au/Cr film. We then used mechanical exfoliation to deposit the

graphene and took the Raman spectrum of graphene through the 5 μm circular wells similarly to Fig A1. Figure A2 (a) shows a few layer graphene flake on Au/Cr coated wafer. The larger circles are locations where there is no Au/Cr and only SiO_x with or without graphene. The blue circle corresponds to the location where Raman spectrum was taken. The number of graphene layers is verified using the same method as previously introduced.
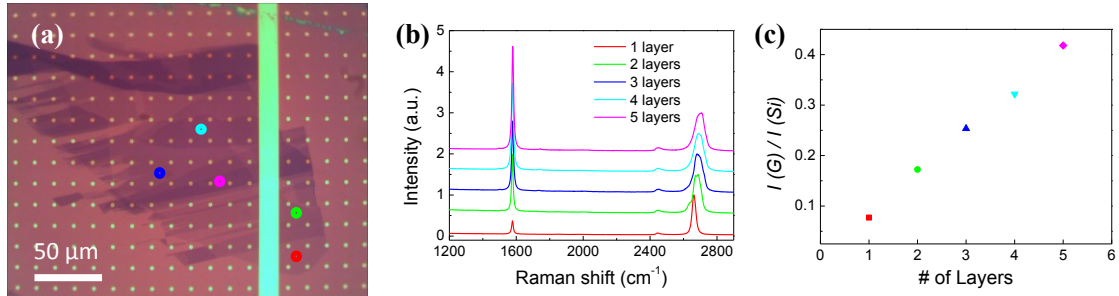
Figure A1: Determining the number of layers

(a) Optical image showing one of the graphene flakes corresponding to some of the samples measured in Fig. 1e. The colored circles denote the location at which Raman spectroscopy was taken (black-1 layer, red-2 layers, green-3 layers, blue-4 layers, and cyan-5 layers).

(b) Raman spectrum for the graphene flake in (a). The color of each curve corresponds to Raman spectrum taken at the corresponding colored circle in the optical image.

(c) Ratio of the integrated intensity of the first order silicon peak I(Si) and the graphene G peak, I(G) (i.e. I(G)/I(Si) for the Raman spectrum in (b).

117
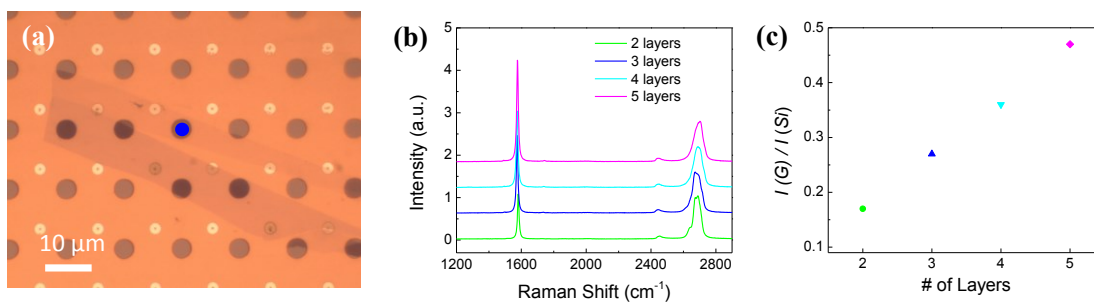
Figure A2: Additional Raman spectrum

   (a) Optical image showing a few layer graphene flake on Au coating. The blue circles denote the location at which Raman spectroscopy was taken.

(b) Raman spectrum for 2-5 layers graphene flakes on Au coating through 5 µm wells.

(c) Ratio of the integrated intensity of the first order silicon peak I(Si) and the graphene G peak, I(G) (i.e. I(G)/I(Si) for the Raman spectrum in (b).

A2. Analytical Model for Pull-in Instability in Graphene Membrane

We developed a simple analytical model based on membrane mechanics to describe the interrelationship of the system parameters in the experiment and we use it inversely with the measurements to infer the operant surface forces[2].

The symbols used in our approach are:

b = Post Radius

a = Outer Radius of the cavity

E = Young's Modulus

t = thickness

v = Poisson's Ratio

S = Total Tension/Membrane Force in the radial direction

S_r = Incremental tension in the radial direction

S_t = Incremental tension in the tangential direction

S_0 = Initial equi-biaxial tension

ΔP = Pressure exerted by the difference of gas pressures inside and outside the cavity

P_{att} = Pressure due to the post-graphene interactions

r = Radial Co-ordinate, $0 < r < a$

w = Deflection of the membrane, as a function of r

h = Deflection at $r = 0$

The key assumptions of our treatment are:

1) The membrane tension S is uniform.

2) The pressure due to the surface forces acting between the post and the membrane, P_{att}, is uniform. This is reasonable if the membrane curvature is small. This is the case when the post is small compared to the overall size of the cavity.

In order to understand the validity and impact of these assumptions, we also carry out high-fidelity finite element (FE) simulations where they are removed; these are described in the next section.

Force equilibrium in the vertical direction gives (see Figure 6.2 (a)):

$$(\Delta P\text{-}P_{att})r^2 = -2\,S\,r\frac{dw}{dr} \qquad r < b$$

$$\Delta P\,r^2\text{-}P_{att}b^2 = -2\,S\,r\frac{dw}{dr} \qquad r \geq b$$

$$S = S_r + S_0$$

The negative sign on the right hand side is due to dw/dr being negative. Integrating with respect to r with appropriate limits, yields:

$$w = h\text{-}\frac{\Delta P\text{-}P_{att}}{4S}r^2 \qquad r < b$$

$$w = w(r = b) + \frac{1}{4S}\left(P_{att}b^2\log\left(\frac{r^2}{b^2}\right)\text{-}\Delta P(r^2\text{-}b^2)\right) \qquad r \geq b$$

Due to continuity of w at $r = b$ we obtain:

$$w = h\text{-}\frac{\Delta P\text{-}P_{att}}{4S}r^2 \qquad r < b$$

$$w = h + \frac{1}{4S}\left(P_{att}b^2\log\left(\frac{r^2}{b^2}\right) + P_{att}b^2\text{-}\Delta P\,r^2\right) \qquad r \geq b$$

Applying the boundary condition $w(r = a) = 0$, yields:

$$h = \frac{1}{4S}\left(\Delta P \, a^2 - P_{att}b^2\left(1 + \log\left(\frac{a^2}{b^2}\right)\right)\right) \qquad (1)$$

Finally,

$$w = \frac{1}{4S}\left(\Delta P(a^2 - r^2) - P_{int}(b^2 - r^2) - P_{att}b^2\log\left(\frac{a^2}{b^2}\right)\right) \qquad r < b \qquad (2)$$

$$w = \frac{1}{4S}\left(\Delta P(a^2 - r^2) + P_{att}b^2\log\left(\frac{r^2}{a^2}\right)\right) \qquad r \geq b \qquad (3)$$

We assume that the membrane is in an equi-biaxial state, then $S_r = S_t$ and $\epsilon_r = \epsilon_t = \frac{S}{Et/(1-v)}$ and:

$$\epsilon_r + \epsilon_t = \frac{du}{dr} + \frac{u}{r} + \frac{1}{2}\left(\frac{dw}{dr}\right)^2 = \frac{2 S_r}{Et/(1-v)}$$

Integrating with respect to an area element $2\pi r dr$ over $(0, a)$, yields:

$$\int_0^a d(ur) + \int_0^a \frac{r}{2}\left(\frac{dw}{dr}\right)^2 dr = \frac{2 S_r}{Et/(1-v)}\int_0^a rdr$$

The first integral on the LHS is zero due to the boundary conditions and thus:

$$S_r S^2 = \frac{Et}{32 \, a^2(1-v)}\left((\Delta P - P_{att})^2 b^4 + \Delta P^2\left(a^4 - b^4\right)\right.$$

$$\left. + P_{att}^2 b^4 \log\left(\frac{a^4}{b^4}\right) - 4 \, \Delta P \, P_{att} b^2\left(a^2 - b^2\right)\right) \qquad (4)$$

In order to obtain the condition for pull-in we eliminate S_r and S from eqs. (1) and (4) results in an equation for h in terms of $a, b, Et, v, \beta, S_0, P_{att}$ and ΔP; in our experimental configuration all of these are known except ΔP and S_0. When we specify a particular value of S_0 this yields an expression for the load-deflection behavior, i.e., ΔP vs. h.

$$\frac{\text{Et}}{32\ a^2(1-v)}\left((\Delta P\text{-}P_{att})^2 b^4 + \Delta P^2\left(a^4\text{-}b^4\right) + P_{att}^2 b^4 \log\left(\frac{a^4}{b^4}\right)\text{-}4\ \Delta P\ P_{att}b^2\left(a^2\text{-}b^2\right)\right)$$

$$+\left(S_0\left(\frac{1}{4h}\left(\Delta P\ a^2\text{-}P_{att}b^2\left(1+\log\left(\frac{a^2}{b^2}\right)\right)\right)\right)^2\right)$$

$$=\left(\frac{1}{4h}\left(\Delta P\ a^2\text{-}P_{att}b^2\left(1+\log\left(\frac{a^2}{b^2}\right)\right)\right)\right)^3 \qquad (5)$$

Consistent with the van der Waals (vdW) form, we assume P_{att} is given by a power law of the form,

$$P_{att} = \frac{\beta}{h^4}$$

The pull-in condition occurs at the limit point:

$$\frac{d\Delta P}{dh} = 0 \qquad (6)$$

which yields a unique ΔP and S_0 when β and h are specified.

A3. Calculation of Constants for Interfacial Forces

Using the analytical model described above, we calculate the values of β assuming a range of initial tension, S_0. Previous results on mechanically exfoliated monolayer and few layer graphene found S_0 in the range of 0.03 - 0.15 N/m where the average values was $S_0 = 0.07$ N/m[5-7]. Figure A3a shows calculated β for different S_0 (0.03, 0.05, 0.09 N/m). This range also marks the shaded boundaries for the theoretically calculated pull-in distance in Figure 6.5.

The same analytical model used to calculate β can be applied to $α$ and $γ$, where γ is a constant similar to α and β assuming $P_{att} = γ/h^3$. The inverse cubic dependence for the interfacial interactions can arise due to vdW interactions between thick graphene membranes and the substrate. Calculated $α$ and $γ$ with $S_0 = 0.03, 0.05, 0.09$ N/m is shown in Fig. A3b and Fig. A3c. The calculated $α$ for all the devices measured is plotted in Fig. S6a assuming $S_0 = 0.07$ N/m. The same analysis is done with γ shown in Fig. S6b. We also plot pull-in distance (h) versus post diameter ($2b$) for this power law and compare it with $P_{att} = β/h^4$ and the experimental data in Fig. A4. Even though the plot fits experimental data closely for 2-4 layers graphene membrane, it does not fit the data from monolayer graphene membranes as well.
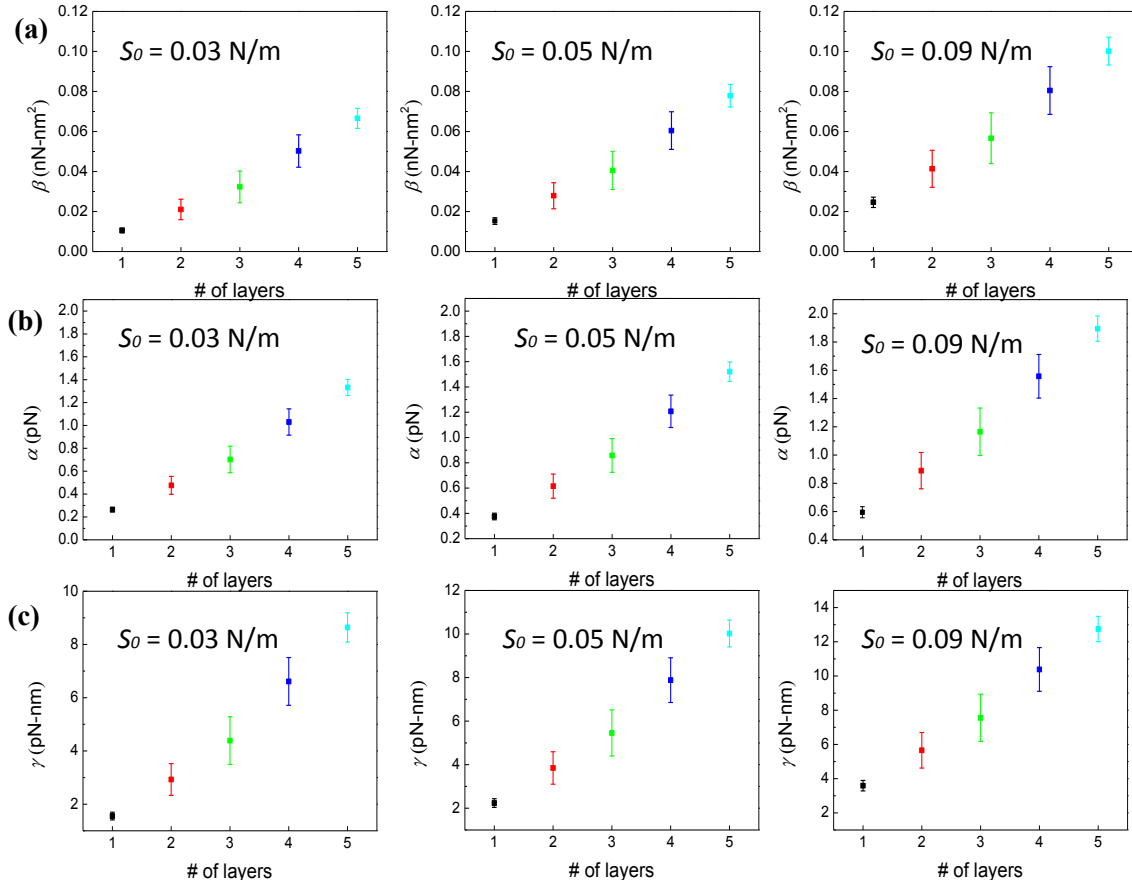
Figure A3: *α, β, γ* vs. number of layers

(a) The calculated values of *β* vs. number of layers assuming a model where the force responsible for pull-in has the form $P_{att} = \beta/h^4$ with different initial tension $S_0 = 0.03$ N/m, $S_0 = 0.05$ N/m, $S_0 = 0.09$ N/m

(b) The calculated values of *α* vs. number of layers assuming a model where the force responsible for pull-in has the form $P_{att} = \alpha/h^2$ with different initial tension $S_0 = 0.03$ N/m, $S_0 = 0.05$ N/m, $S_0 = 0.09$ N/m

(c) The calculated values of *γ* vs. number of layers assuming a model where the force responsible for pull-in has the form $P_{att} = \gamma/h^3$ with different initial tension $S_0 = 0.03$ N/m, $S_0 = 0.05$ N/m, $S_0 = 0.09$ N/m
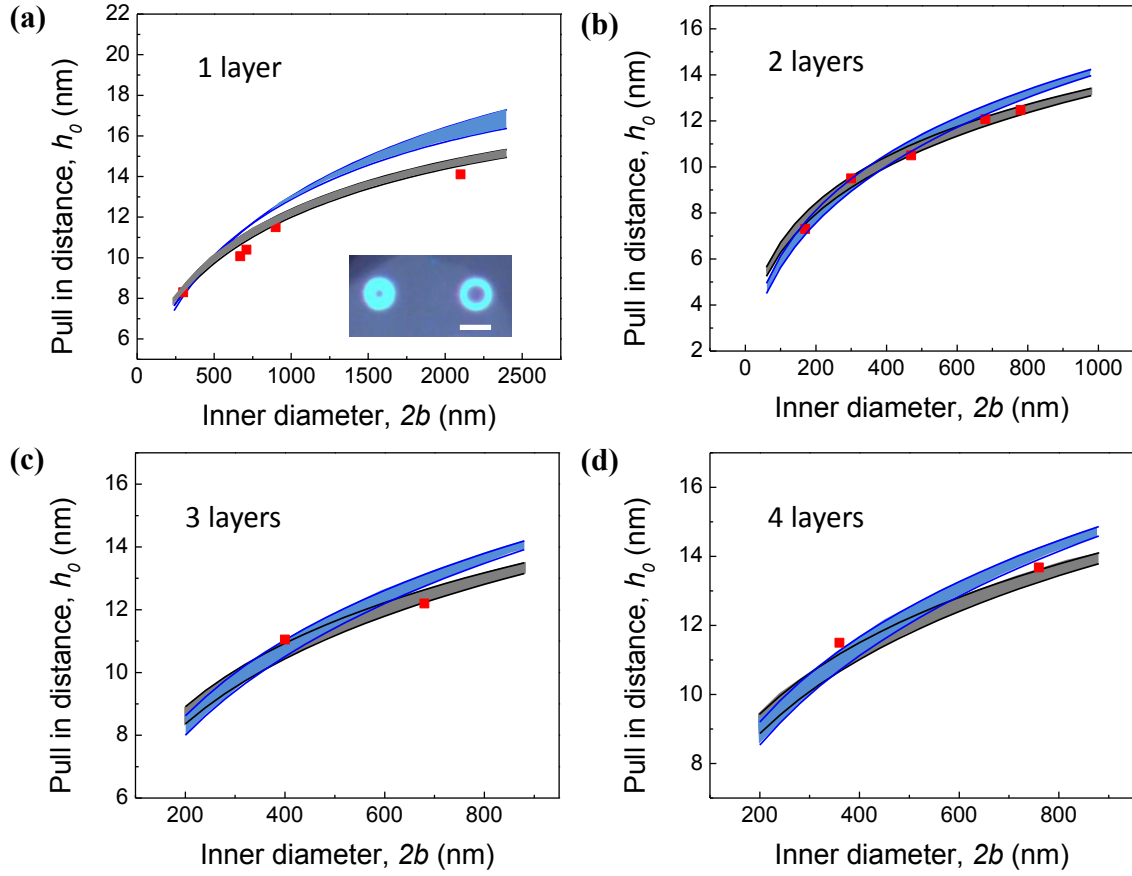
Figure A4: Scaling of the pull in distance with P_{att}

Pull in distance, h_0, vs. inner diameter, $2b$, for a) 1 layer b) 2 layer c) 3 layer d) 4 layer graphene flakes (verified by Raman spectroscopy) with identical outer diameter but different inner diameters. The black and blue shaded lines are the calculated results for 2 different power law dependences $P_{att} = \beta/h^4$ (black) and $P_{att} = \alpha/h^3$ (blue) with $S_0 = 0.03 - 0.09$ N/m. The values of β and γ are listed in Fig. A3. a) (inset) Optical image of 2 of the measured monolayer devices. The scale bar = 5 µm.